

AD-A099 532

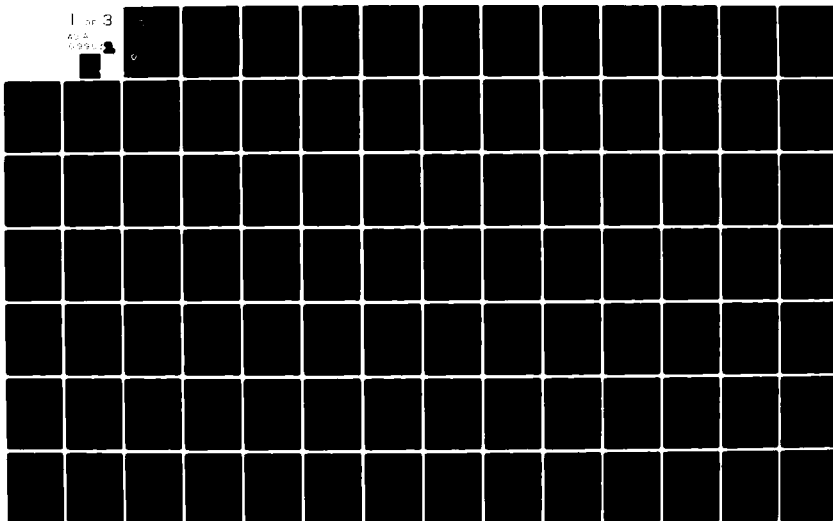
ARMY TROOP SUPPORT AND AVIATION MATERIEL READINESS CO--ETC F/G 20/4
ROTOR DYNAMIC INFLOW DERIVATIVES AND TIME CONSTANTS FROM VARIOU--ETC(U)
DEC 80 D M PITT
TSARCOM-TR-81-2

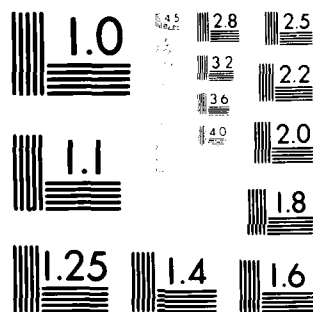
UNCLASSIFIED

NL

1 of 3

AD-A
0099 532





MICROCOPY RESOLUTION TEST CHART
NBS 1010-A-4a

AD A099532

DTIC FILE COPY

USATSARCOM

TR 81-2

**ROTOR DYNAMIC INFLOW DERIVATIVES
AND TIME CONSTANTS FROM
VARIOUS INFLOW MODELS**

DALE M. PITT

December 1980

LEVEL II

12

DTIC
ELECTE
JUN 0 1 1981
S D
E

APPROVED FOR PUBLIC RELEASE; DISTRIBUTION UNLIMITED



**U.S. ARMY TROOP SUPPORT AND AVIATION MATERIEL READINESS COMMAND
DIRECTORATE FOR PLANS AND SYSTEMS ANALYSIS
4300 GOODFELLOW BOULEVARD
ST. LOUIS, MISSOURI 63120**

81 6 01 050

DISCLAIMER STATEMENT

The view, opinions, and/or findings contained in this report are those of the author and should not be construed as an official Department of the Army position, policy, or decision, unless so designated by other documentation.

UNCLASSIFIED

SECURITY CLASSIFICATION OF THIS PAGE (When Data Entered)

14 REPORT DOCUMENTATION PAGE		READ INSTRUCTIONS BEFORE COMPLETING FORM	
1. REPORT NUMBER USATSARCOM-TR-81-2	2. GOVT ACCESSION NO. AD-A099532	3. RECIPIENT'S CATALOG NUMBER	
4. TITLE (and Subtitle) ROTOR DYNAMIC INFLOW DERIVATIVES AND TIME CONSTANTS FROM VARIOUS INFLOW MODELS		5. TYPE OF REPORT & PERIOD COVERED THESIS	
7. AUTHOR(s) DALE M. /PITT		6. PERFORMING ORG. REPORT NUMBER	
9. DRSTs		8. CONTRACT OR GRANT NUMBER(s)	
9. DRSTs		10. PROGRAM ELEMENT, PROJECT, TASK AREA & WORK UNIT NUMBERS	
10. PERFORMING ORGANIZATION NAME AND ADDRESS USATSARCOM, ATTN: DRSTS-B 4300 GOODFELLOW BLVD. ST. LOUIS, MO 63120		11. REPORT DATE DECEMBER 1980	
11. CONTROLLING OFFICE NAME AND ADDRESS USATSARCOM, ATTN: DRSTS-B 4300 GOODFELLOW BLVD. ST. LOUIS, MO 63120		12. NUMBER OF PAGES 231	
13. MONITORING AGENCY NAME & ADDRESS (if different from Controlling Office)		13. SECURITY CLASS. (of this report) UNCLASSIFIED	
14. DISTRIBUTION STATEMENT (of this Report) APPROVED FOR PUBLIC RELEASE; DISTRIBUTION UNLIMITED		15a. DECLASSIFICATION/DOWNGRADING SCHEDULE	
17. DISTRIBUTION STATEMENT (of the abstract entered in Block 20, if different from Report)			
18. SUPPLEMENTARY NOTES THIS IS A DISSERTATION PRESENTED TO THE SEVER INSTITUTE OF WASH- INGTON UNIVERSITY IN PARTIAL FULFILLMENT OF THE REQUIREMENTS FOR THE DEGREE OF DOCTOR OF SCIENCE. THIS WORK WAS PERFORMED UNDER THE DIRECTION OF PROFESSOR DAVID A. PETERS.			
19. KEY WORDS (Continue on reverse side if necessary and identify by block number) DYNAMIC-INFLOW, INDUCED VELOCITY, HELICOPTER, ROTORS, TIME CONSTANTS, GAINS, UNSTEADY AERODYNAMICS, ACTUATOR DISC			
20. ABSTRACT (Continue on reverse side if necessary and identify by block number) A LINEAR, UNSTEADY THEORY IS DEVELOPED THAT RELATED TRANSIENT ROTOR LOADS (THRUST, ROLL MOMENT, AND PITCH MOMENT) TO THE OVERALL TRANSIENT RESPONSE OF THE ROTOR INDUCED-INFLOW FIELD. THE RELATIONSHIPS ARE DERIVED FROM AN UNSTEADY, ACTUATOR-DISC THEORY; AND SOME ARE OBTAINED IN CLOSED FORM. THE THEORY IS USED TO DETERMINE THE EFFECTS OF LIFT DISTRIBUTION AND SHAFT ANGLE-OF- ATTACK ON THE SAID RELATIONSHIPS. ALSO, TWO DIFFERENT ASSUMP- TIONS ARE USED IN THE UNSTEADY CALCULATIONS, FINALLY, A			

DD FORM 1 JAN 73 1473

EDITION OF 1 NOV 68 IS OBSOLETE

UNCLASSIFIED

SECURITY CLASSIFICATION OF THIS PAGE (When Data Entered)

UNCLASSIFIED

SECURITY CLASSIFICATION OF THIS PAGE(When Data Entered)

PRESCRIBED WAKE ANALYSIS IS USED TO VALIDATE THE ACTUATOR-DISC THEORY FOR NORMAL FLIGHT CONDITIONS. THE RESULTS REVEAL BOTH THE STRENGTHS AND WEAKNESSES OF PREVIOUS FORMULATIONS AND REVEAL AREAS IN WHICH FURTHER STUDY IS NEEDED. THE MOST SIGNIFICANT RESULT IS AN ANALYTIC, THREE-DEGREE-OF-FREEDOM INFLOW MODEL THAT IS SHOWN TO BE ACCURATE FOR USE IN THE DYNAMIC ANALYSIS OF ROTORS.

UNCLASSIFIED

SECURITY CLASSIFICATION OF THIS PAGE(When Data Entered)

WASHINGTON UNIVERSITY
SEVER INSTITUTE OF TECHNOLOGY

ROTOR DYNAMIC INFLOW DERIVATIVES AND TIME
CONSTANTS FROM VARIOUS INFLOW MODELS

by

DALE M. PITT

Prepared under the direction of Professor D. A. Peters

A dissertation presented to the Sever Institute of
Washington University in partial fulfillment
of the requirements for the degree of

DOCTOR OF SCIENCE

December, 1980

Saint Louis, Missouri

Accession For	
NTIS GRA&I	<input checked="checked" type="checkbox"/>
DTIC TAB	<input type="checkbox"/>
Unannounced	<input type="checkbox"/>
Justification	
By	
Distribution/	
Availability Codes	
Avail and/or	
Dist	Special
A	

WASHINGTON UNIVERSITY
SEVER INSTITUTE OF TECHNOLOGY

ABSTRACT

ROTOR DYNAMIC INFLOW DERIVATIVES AND TIME
CONSTANTS FROM VARIOUS INFLOW MODELS

by Dale Marvin Pitt

ADVISOR: Professor D. A. Peters

December, 1980

Saint Louis, Missouri

A linear, unsteady theory is developed that relates transient rotor loads (thrust, roll moment, and pitch moment) to the overall transient response of the rotor induced-flow field. The relationships are derived from an unsteady, actuator-disc theory; and some are obtained in closed form. The theory is used to determine the effects of lift distribution and shaft angle-of-attack on the said relationships. Also, two different assumptions are used in the unsteady calculations. Finally, a prescribed wake analysis is used to validate the actuator-disc theory for normal flight conditions. The results reveal both the strengths and weaknesses of previous formulations and reveal areas in which further study is needed. The most significant result is an analytic, three-degree-of-freedom inflow model that is shown to be accurate for use in the dynamic analysis of rotors.

TABLE OF CONTENTS

No.		Page
1.	Introduction	1
2.	Previous Work	4
2.1	General Inflow Theories	4
2.1.1	Simple Actuator-Disc Theories	4
2.1.2	Simple Vortex Theories	9
2.1.3	Vortex Theories-Finite Number of Blades	13
2.1.4	Improved Actuator-Disc Theories	18
2.2	Dynamic Inflow Theories	25
2.2.1	Early Work	25
2.2.2	Recent Work	31
3.	Mathematical Formulation of Inflow Models	46
3.1	Actuator-Disc Theory	46
3.1.1	Steady Aerodynamics	46
3.1.2	Unsteady Aerodynamics	64
3.2	Prescribed-Wake Vortex Theory	74
4.	Development of Computer Models	77
4.1	Actuator-Disc Program	77
4.1.1	Steady Calculations	77
4.1.2	Unsteady Calculations	86
4.2	Prescribed-Wake Computer Program	88
5.	Results and Discussions	91
5.1	Actuator-Disc Results	91
5.1.1	Steady Results	91
5.1.2	Unsteady Results	113
5.2	Prescribed-Wake Results	147

TABLE OF CONTENTS
(continued)

No.		Page
6.	Conclusions and Recommendations	154
6.1	Conclusions Concerning the Steady, Actuator-Disc Model	154
6.2	Conclusions Concerning the Unsteady, Actuator-Disc Model	156
6.3	Conclusions Concerning the Prescribed-Wake Model	157
6.4	Comments Concerning the Analytical Model	157
6.5	Recommendations for Future Research	158
7.	Appendices	161
7.1	Actuator Disc Coordinate System	162
7.2	Legendre Polynomials and Their Associated Properties	167
7.3	Actuator Disc Aerodynamic Loading	176
7.4	Unsteady Actuator Disc-Supplemental Data	181
7.5	Nomenclature	204
8.	Bibliography	209
9.	Vita	216

LIST OF TABLES

No.	Page
1. Dynamic Inflow History	26
2. Empirical L-Matrix	38
3. L-Matrix for Edgewise Flow	95
4. Elements of M-Matrix	115
5. Analytic Forms of L-Matrix and M-Matrix	146

LIST OF FIGURES

No.		Page
1.	Glauert's Linear Variation of Momentum Induced Velocities Along the Rotor Disc	6
2.	Blade-Element Theory Induced Velocity Distribution for the Hover Condition	8
3.	Undistorted Rigid Wake Distribution of the Lifting Line Vortex Theory	15
4.	The Semi-Empirical Induced Velocity Superposition Theory of Stricker and Gradl	20
5.	Comparison of Measured and Mangler-Squire's Calculated Values of Induced Velocity Along the Rotor Longitudinal Axis	23
6.	Comparison of Measured and Mangler-Squire's Calculated Values of Induced Velocity Along the Rotor Lateral Axis	24
7.	Effects of Streamline Integration Increments on the Induced Velocity Distribution. Corrected Thrust Distribution and $\alpha = 90^\circ$	80
8.	Effects of Different Integration Techniques on the Accuracy of the L(1,1) Term. Corrected Thrust Distribution and $\alpha = 90^\circ$	82
9.	Effects of the Streamline Integration Increment Size on the Accuracy of the Diagonal Elements of the L Matrix. Corrected Thrust Distribution and $\alpha = 90^\circ$	84
10.	First Column of the [L] Matrix	92
11.	Second Column of the [L] Matrix	92
12.	Third Column of the [L] Matrix	93
13.	Fourth Column of the [L] Matrix	93
14.	Fifth Column of the [L] Matrix	94
15.	First Column of the Inverted [L] Matrix	104
16.	Second Column of the Inverted [L] Matrix	106
17.	Third Column of the Inverted [L] Matrix	107
18.	Fourth Column of the Inverted [L] Matrix	108

LIST OF FIGURES
(continued)

No.	Page
19.	Fifth Column of the Inverted [L] Matrix 110
20.	First and Second Columns of the Deviation Matrix 112
21.	Third Column of the Deviation Matrix 112
22.	Imaginary Part of the (1,1) Element of the Inverted Complex L(K) Matrix, $\alpha = 90^\circ$ 114
23.	Imaginary Part of the (2,2) or (3,3) Element of the Inverted Complex L(K) Matrix, $\alpha = 90^\circ$ 114
24.	Imaginary Part of the (4,4) or (5,5) Element of Inverted L(K) Matrix, $\alpha = 90^\circ$ 115
25.	Apparent Mass Element M(1,1) for $\alpha = 90^\circ$ 118
26.	Apparent Mass Elements M(2,2) and M(3,3) for $\alpha = 90^\circ$ 118
27.	Apparent Mass Elements M(4,4) and M(5,5) for $\alpha = 90^\circ$ 120
28.	Magnitude of the (1,1) Element of Inverted Complex L(K) Matrix at $\alpha = 90^\circ$ with Corrected Pressure 120
29.	Magnitude of the (1,1) Element of Inverted Complex L(K) Matrix at $\alpha = 90^\circ$ with Uncorrected Pressure 122
30.	Magnitude of the (2,2) and (3,3) Elements of Inverted Complex L(K) Matrix at $\alpha = 90^\circ$ with Corrected Pressure 122
31.	Magnitude of the (2,2) and (3,3) Elements of Inverted Complex L(K) Matrix at $\alpha = 90^\circ$ with Uncorrected Pressure 123
32.	Magnitude of the (4,4) and (5,5) Elements of Inverted Complex L(K) Matrix at $\alpha = 90^\circ$ 123
33.	Phase Angle of the (1,1) Element of Inverted Complex L(K) Matrix at $\alpha = 90^\circ$ with Corrected Thrust Distribution 127

LIST OF FIGURES
(continued)

No.	Page
34.	Phase Angle of the (1,1) Element of Inverted Complex L(K) Matrix at $\alpha = 90^\circ$ with Uncorrected Thrust Distribution 127
35.	Phase Angle of the (2,2) and (3,3) Elements of Inverted Complex L(K) Matrix at $\alpha = 90^\circ$ for Corrected Moment Distribution 128
36.	Phase Angle of the (2,2) and (3,3) Elements of Inverted Complex L(K) Matrix at $\alpha = 90^\circ$ for Uncorrected Moment Distribution 128
37.	Phase Angle of the (4,4) and (5,5) Elements of Inverted Complex L(K) Matrix at $\alpha = 90^\circ$ for Second Harmonic Load Distribution 129
38.	Magnitude of the (1,1) Element of Inverted Complex L(K) Matrix for α Sweep (Corrected Pressure) 129
39.	Magnitude of the (3,1) Element of Inverted Complex L(K) Matrix for α Sweep (Corrected Pressure) 132
40.	Magnitude of the (5,1) Element of Inverted Complex L(K) Matrix for α Sweep (Corrected Pressure) 132
41.	Complex Induced Velocity Distribution For $K = 10$, $\alpha = 1^\circ$, and Uncorrected Thrust Loading 135
42.	Steady Induced Velocity Distribution for $\alpha = 1^\circ$ and Uncorrected Thrust Loading 135
43.	Phase Angle of the (1,1) Element of Inverted Complex L(K) Matrix for α Sweep (Corrected Pressure) 136
44.	Phase Angle of the (3,1) Element of Inverted Complex L(K) Matrix for α Sweep (Corrected Pressure) 136
45.	Phase Angle of the (5,1) Element of Inverted Complex L(K) Matrix for α Sweep (Corrected Pressure) 137

LIST OF FIGURES
(continued)

No.		Page
46.	Imaginary Part of the (1,1) Element of the Inverted Complex L(K) Matrix for α Sweep (Corrected Pressure)	137
47.	Imaginary Part of the (3,1) Element of the Inverted Complex L(K) Matrix for α Sweep (Corrected Pressure)	140
48.	Imaginary Part of (5,1) Element of the Inverted Complex L(K) Matrix for α Sweep (Corrected Pressure)	140
49.	Deviation of the Real Part of the (1,1) Element of the Inverted Complex L(K) Matrix as Calculated by S.P. and S.V. for α Sweep (Corrected Pressure)	142
50.	Deviation of the Real Part of the (3,1) Element of the Inverted Complex L(K) Matrix as Calculated by S.P. and S.V. for α Sweep (Corrected Pressure)	142
51.	Deviation of the Real Part of the (5,1) Element of the Inverted Complex L(K) Matrix as Calculated by S.P. and S.V. for α Sweep (Corrected Pressure)	143
52.	Deviation of the Imaginary Part of Element (1,1) for the S.V. 5X5 and 3X3 Complex Inverted L(K) Matrix for α Sweep (Corrected Pressure Distribution)	143
53.	Deviation of the Imaginary Part of Element (3,1) for the S.V. 5X5 and 3X3 Complex Inverted L(K) Matrix for α Sweep (Corrected Pressure Distribution)	145
54.	Relative Magnitude of the Off-Diagonal Terms of the 3X3 Inverted Complex L(K) Matrix at $\alpha = 30^\circ$	145
55.	Phase Angle of Complex (1,3)/(3,3) for Analytical L and M Matrices	148
56.	Phase Angle of Complex (3,1)/(3,3) for Analytical L and M Matrices	148

LIST OF FIGURES
(continued)

No.		Page
57.	First Column of the Prescribed-Wake L-Matrix	149
58.	Second Column of the Prescribed-Wake L-Matrix	150
59.	Third Column of the Prescribed-Wake L-Matrix	152

Appendices:

7.1.1	Wind and Disc Cartesian Coordinate Systems	162
7.1.2	Curvilinear Coordinate System (Ellipsoidal Coordinate System)	165
7.1.3	Integration of Induced Velocity Along a Streamline in the X Direction	166
7.2.1	P_1^0 , P_3^0 and Corrected Thrust for C_T	173
7.2.2	P_2^1 , P_4^1 and Corrected Moment for C_L and C_M	173
7.2.3	P_3^2 for C_{2L} and C_{2M}	174
7.2.4	Q_1^0 and Q_3^0 Variation with η	174
7.2.5	Q_2^1 and Q_4^1 Variation with η	175
7.2.6	Q_3^2 Variation with η	175
7.3.1	Uncorrected Thrust Distribution	178
7.3.2	Corrected Thrust Distribution	178
7.3.3	Negative Pitching Moment Distribution	179
7.3.4	Negative Rolling Moment Distribution	179
7.3.5	Negative Second Harmonic Loading Distribution of $\cos 2\psi$	180
7.3.6	Negative Second Harmonic Loading Distribution of $\sin 2\psi$	180

LIST OF FIGURES
(continued)

No.		Page
7.4.1	Magnitude of the (2,2) Element of Inverted Complex L(K) Matrix for α Sweep (Corrected Pressure)	182
7.4.2	Magnitude of the (4,2) Element of Inverted Complex L(K) Matrix for α Sweep (Corrected Pressure)	182
7.4.3	Magnitude of the (1,3) Element of Inverted Complex L(K) Matrix for α Sweep (Corrected Pressure)	183
7.4.4	Magnitude of the (3,3) Element of Inverted Complex L(K) Matrix for α Sweep (Corrected Pressure)	183
7.4.5	Magnitude of the (5,3) Element of Inverted Complex L(K) Matrix for α Sweep (Corrected Pressure)	184
7.4.6	Magnitude of the (2,4) Element of Inverted Complex L(K) Matrix for α Sweep (Corrected Pressure)	184
7.4.7	Magnitude of the (4,4) Element of Inverted Complex L(K) Matrix for α Sweep (Corrected Pressure)	185
7.4.8	Magnitude of the (1,5) Element of Inverted Complex L(K) Matrix for α Sweep (Corrected Pressure)	185
7.4.9	Magnitude of the (3,5) Element of Inverted Complex L(K) Matrix for α Sweep (Corrected Pressure)	186
7.4.10	Magnitude of the (5,5) Element of Inverted Complex L(K) Matrix for α Sweep (Corrected Pressure)	186
7.4.11	Phase Angle of the (2,2) Element of Inverted Complex L(K) Matrix for α Sweep (Corrected Pressure)	187
7.4.12	Phase Angle of the (4,2) Element of Inverted Complex L(K) Matrix for α Sweep (Corrected Pressure)	187

LIST OF FIGURES
(continued)

No.	Page
7.4.13 Phase Angle of the (1,3) Element of Inverted Complex L(K) Matrix for α Sweep (Corrected Pressure)	188
7.4.14 Phase Angle of the (3,3) Element of Inverted Complex L(K) Matrix for α Sweep (Corrected Pressure)	188
7.4.15 Phase Angle of the (5,3) Element of Inverted Complex L(K) Matrix for α Sweep (Corrected Pressure)	189
7.4.16 Phase Angle of the (2,4) Element of Inverted Complex L(K) Matrix for α Sweep (Corrected Pressure)	189
7.4.17 Phase Angle of the (4,4) Element of Inverted Complex L(K) Matrix for α Sweep (Corrected Pressure)	190
7.4.18 Phase Angle of the (1,5) Element of Inverted Complex L(K) Matrix for α Sweep (Corrected Pressure)	190
7.4.19 Phase Angle of the (3,5) Element of Inverted Complex L(K) Matrix for α Sweep (Corrected Pressure)	191
7.4.20 Phase Angle of the (5,5) Element of Inverted Complex L(K) Matrix for α Sweep (Corrected Pressure)	191
7.4.21 Imaginary Term of the (2,2) Element Inverted Complex L(K) Matrix for α Sweep (Corrected Pressure)	192
7.4.22 Imaginary Term of the (4,2) Element Inverted Complex L(K) Matrix for α Sweep (Corrected Pressure)	193
7.4.23 Imaginary Term of the (1,3) Element Inverted Complex L(K) Matrix for α Sweep (Corrected Pressure)	193
7.4.24 Imaginary Term of the (3,3) Element Inverted Complex L(K) Matrix for α Sweep (Corrected Pressure)	193

LIST OF FIGURES
(continued)

No.	Page
7.4.25 Imaginary Term of the (5,3) Element Inverted Complex L(K) Matrix for α Sweep (Corrected Pressure)	194
7.4.26 Imaginary Term of the (2,4) Element Inverted Complex L(K) Matrix for α Sweep (Corrected Pressure)	194
7.4.27 Imaginary Term of the (4,4) Element Inverted Complex L(K) Matrix for α Sweep (Corrected Pressure)	195
7.4.28 Imaginary Term of the (1,5) Element Inverted Complex L(K) Matrix for α Sweep (Corrected Pressure)	195
7.4.29 Imaginary Term of the (3,5) Element Inverted Complex L(K) Matrix for α Sweep (Corrected Pressure)	196
7.4.30 Imaginary Term of the (5,5) Element Inverted Complex L(K) Matrix for α Sweep (Corrected Pressure)	196
7.4.31 Deviation of Real Terms of the (2,2) Element Inverted Complex L(K) Matrix for α Sweep (Corrected Pressure)	197
7.4.32 Deviation of Real Terms of the (4,2) Element Inverted Complex L(K) Matrix for α Sweep (Corrected Pressure)	197
7.4.33 Deviation of Real Terms of the (1,3) Element Inverted Complex L(K) Matrix for α Sweep (Corrected Pressure)	198
7.4.34 Deviation of Real Terms of the (3,3) Element Inverted Complex L(K) Matrix for α Sweep (Corrected Pressure)	198
7.4.35 Deviation of Real Terms of the (5,3) Element Inverted Complex L(K) Matrix for α Sweep (Corrected Pressure)	199
7.4.36 Deviation of Real Terms of the (2,4) Element Inverted Complex L(K) Matrix for α Sweep (Corrected Pressure)	199

LIST OF FIGURES
(continued)

No.		Page
7.4.37	Deviation of Real Terms of the (4,4) Element Inverted Complex L(K) Matrix for α Sweep (Corrected Pressure)	200
7.4.38	Deviation of Real Terms of the (1,5) Element Inverted Complex L(K) Matrix for α Sweep (Corrected Pressure)	200
7.4.39	Deviation of Real Terms of the (3,5) Element Inverted Complex L(K) Matrix for α Sweep (Corrected Pressure)	201
7.4.40	Deviation of Real Terms of the (5,5) Element Inverted Complex L(K) Matrix for α Sweep (Corrected Pressure)	201
7.4.41	Deviation of Imaginary Terms of the (2,2) Element Inverted Complex L(K) Matrix for α Sweep (Corrected Pressure)	202
7.4.42	Deviation of Imaginary Terms of the (1,3) Element Inverted Complex L(K) Matrix for α Sweep (Corrected Pressure)	202
7.4.43	Deviation of Imaginary Terms of the (3,3) Element Inverted Complex L(K) Matrix for α Sweep (Corrected Pressure)	203

ROTOR DYNAMIC INFLOW DERIVATIVES AND TIME CONSTANTS FROM VARIOUS INFLOW MODELS

1. INTRODUCTION

Since the inception of the autogyro and helicopter, investigators have tried physically and mathematically to describe the airflow through the rotor system. The knowledge of the total airflow distribution through and about the helicopter rotor is required to adequately analyze the following characteristics of the helicopter: a) performance, b) vibration, c) rotor stability, d) controllability, e) acoustic signature, and f) rotor air loads and structural limitations. Over the years, a multitude of approaches have been developed to model mathematically the rotor flow-field. Much of the early flow-field theories were based either on the then-existing propeller theories or on fixed-wing aerodynamic analogies. However, in the last decades, rotatory-wing aerodynamics no longer depend on fixed-wing analogies but on theories and math models especially derived for helicopter rotors.

The present rotor inflow theories range from the extremely simple momentum theory to the very complicated

vortex lifting-line and lifting-surface theories that require large computer space and long computer time in their solution process. Uniform inflow is usually associated with the momentum theory while the more complicated vortex theories generally reflect nonuniform inflow. The degree of nonuniformity of the induced velocities is highly dependent upon the rotor's flight condition. The simple models have yielded good results in hover where the inflow can be assumed to be uniform with azimuth. Forward flight, on the other hand, causes unsymmetrical velocities on the rotor both radially and azimuthally. The blade motions of flapping, coning, and torsion result in an instantaneous induced flow field that has inplane, rotational, and normal velocity components that vary with time as well as with rotor azimuth. Consequently, nonuniform inflow theories are used when modeling forward flight.

The majority of the present inflow theories adequately predict steady-state performance and blade responses. However, these theories do not attempt to model inflow effects due to transients in thrust. The transients in rotor thrust result from pilot-controlled maneuvers, wind gusts, or coupled rotor-body oscillations.

The intent of this research is to examine the various helicopter inflow theories, and determine which ones are suitable for predicting the transient inflow velocities. Therefore, one of the actuator-disc inflow theories is

extended and modified to obtain dynamic-inflow derivatives and time constants. The range and validity of the actuator-disc assumption is then determined by exercising a prescribed-wake, lifting-line inflow theory.

2. PREVIOUS WORK

Before we proceed with the development of a suitable dynamic inflow theory, we will review some of the better known static inflow theories. Although each theory has merit, it would be impossible, and beyond the intent of this research, to modify each of the theories to predict unsteady inflows.

Consequently, the intent of this synopsis is to briefly describe and comment on the various inflow models and theories that were reviewed and researched. The advantages, disadvantages, assumptions, and purpose of the inflow theories will be examined, in order to determine those that might be used to determine the dynamic inflow characteristics of a rotor. The theories will generally be addressed in order of sophistication.

2.1 GENERAL INFLOW THEORIES

2.1.1 Simple Actuator-Disc Theories

Simple momentum theory was employed by Glauert (1)^{*} to describe the inflow through the rotor system of the autogyro. Simple momentum theory is based on the assumption of an actuator-disc which is loaded uniformly azimuthally (although it may vary radially). Thus, the theory assumes an infinite number of blades without tip losses. In hover, this results in an inflow distribution for which the induced

* The numbers in parentheses in the text indicate references in the Bibliography.

velocity is assumed to be normal to the rotor plane. The magnitude of the induced velocity, v_o , for the special case of uniform loading, is given by

$$v_o = \sqrt{\frac{T}{2\rho\pi R^2}} = \sqrt{\frac{D.L.}{2\rho}} \quad (1)$$

It should be noted that the value of induced velocity from momentum theory is independent of rotor speed, number of blades, chord length, or airfoil selection. For the forward-flight condition, the theory utilizes the analogy of an elliptically loaded wing having a span of $2R$. Glauert assumes that the total velocity, V_R , through the rotor disc is the vector sum of the induced velocity and the forward flight velocity, V . Hence, the induced velocity for the case of forward flight is:

$$v_o = \frac{T}{2\rho\pi R^2 V_R} = \frac{D.L.}{2\rho V_R} \quad (2)$$

The induced velocities, v_o , is assumed normal to the plane of the rotor and constant (or uniform) over the rotor disc. The induced velocity through the rotor in forward flight or in hover is independent of rotor speed, number of blades and also rotor angle of attack. Sissingh (2) noted for forward flight, and for $V \gg v_o$, that equation number (2) can be simplified to

$$v_o = \frac{T}{2\rho\pi R^2 V} = \frac{D.L.}{2\rho V} \quad (3)$$

This shows that the induced velocity is inversely proportional to forward flight velocity.

Glauert in reference 1 further refined the momentum theory by assuming that in forward flight there is a linear variation of the induced velocity along the rotor disc from the leading edge to the trailing edge. The relationship he proposed was a first-harmonic variation

$$v = v_o (1 + K \cos\psi) \quad (4)$$

In equation number (4), v_o is the induced velocity calculated from the momentum method. The value of the slope K was left undetermined. However, Glauert thought that it should be between 0 and 1. A positive K implies that the induced velocity is a minimum at the leading edge of the rotor and a maximum value at the trailing edge as shown in figure 1.

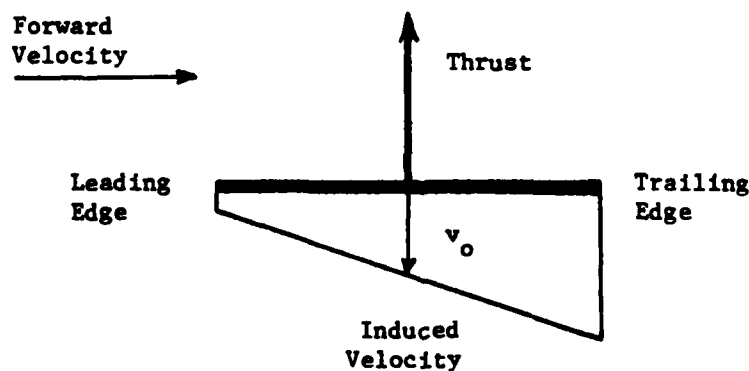


Figure 1. Glauert's Linear Variation of Momentum Induced Velocities Along the Rotor Disc

A significant advantage of momentum theory is that it is a simple representation of the rotor inflow and is an easy model with which to work. When used in conjunction with other computer programs (e.g. loads, performance, etc.) only moderate computer time or space allocation is required. The disadvantage of momentum theory is that it does not model details of the inflow. The magnitude of the inflow velocity and the detailed performance are not completely accurate in the region of transitional flight.

The constant-inflow assumption of simple momentum theory in hover can be removed by the blade-element theory. The blade-element theory for hover is developed in reference (3). The thrust produced by each concentric ring or annulus of rotor disc is obtained as a function of the rotor inflow at that point. The inflow at each element can be determined by a balance of the thrust of the annulus with the overall momentum change in the airflow through that annulus. The induced velocity in hover from the blade element theory is:

$$v(r) = \frac{-bca\Omega}{16\pi} + \sqrt{\left(\frac{bca\Omega}{16\pi}\right)^2 + \frac{bca\Omega^2 r\theta}{8\pi}} \quad (5)$$

Note that the induced velocity depends on number of blades, chord length, slope of the lift curve of the airfoil, and pitch at the particular radial station. Equation (5) was also derived using simple vortex theory by Knight and Hefner in reference 4. For the hover condition, equation (5)

compares favorably with measured results as shown in figure 2 from reference 5.

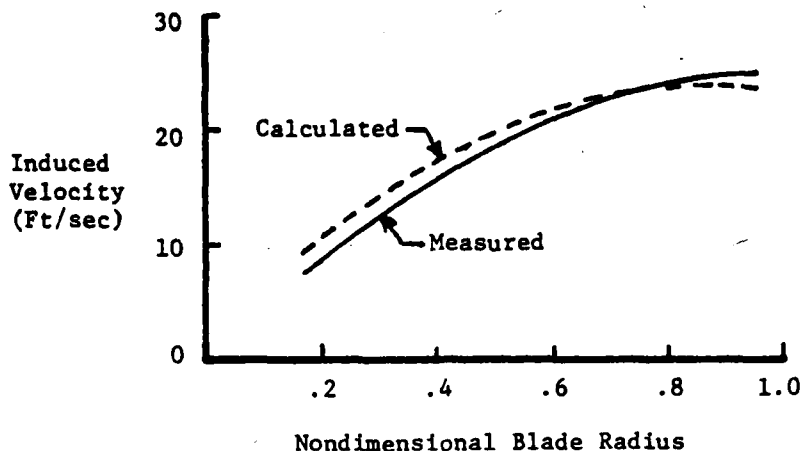


Figure 2. Blade-Element Theory Induced Velocity Distribution for the Hover Condition.

Stepniewski, reference 6, develops a blade-element method of determining the downwash distribution along the fore-and-aft rotor diameter for the case of horizontal flight. It is possible to determine from the blade twist both the geometric and equivalent pitch angle of each blade element along the fore-and-aft disc axis. Stepniewski employs a finite difference procedure to obtain the induced velocity. The requirement to know the magnitude and direction of the relative airflow in the immediate vicinity of the element of the blade is considered a disadvantage of the blade-element method.

Harris and McVeigh (7) utilized the blade-element method of fixed wing aerodynamics rather than the classical

blade-element, momentum theory to determine rotor inflow. They postulated that, in order to acquire zero lift at the tip and root of the blade, the angle-of-attack of the resultant airflow at the tip and root must be zero. Consequently, the induced velocity must increase from the uniform downwash level and ultimately reach an increment of velocity that is nearly twice the uniform downwash level to satisfy the boundary conditions of a practical rotor. Although the method is an improvement over the classical blade-element theory, it has not yet been developed for forward flight and is impractical for transient analysis.

Other than equation (4), all the theories discussed to this point assume uniform inflow (or induced velocities) in the azimuthal direction. In reference 8, Harris questions the validity of this assumption. He shows considerable discrepancy between the predicted lateral flapping and the measured values, concluding that significant fore-and-aft downwash must be occurring.

2.1.2 Simple Vortex Theories

The simple vortex theories were contrived before the advent of the computer, thus numerous assumptions were made to simplify the mathematics. These theories describe the wake as a semi-infinite cylindrical vortex sheet that is effused from the rotor blade tips. An infinite number of blades (i.e., actuator disc concept, uniform blade loading, and neglect of wake contraction) is implied by this theory.

The Biot-Savart law is used to calculate the induced velocities caused by the vorticity sheet.

Knight and Hefner (4) were the first to use this theory in determining the induced velocity and thrust of a hovering rotor. Coleman, Feingold, and Stempin (reference 9) extended the hovering theory of Knight and Hefner to forward flight. The rotor wake was assumed to be an elliptic cylinder of vorticity skewed with respect to the rotor axis at an angle (i.e., wake skew angle) that depends upon the flight velocity and upon the induced velocity. Utilizing this method, they were able to calculate the fore-and-aft variation of the inflow of the rotor as proposed by Glauert in equation (4). The Glauert constant, K , was explicitly expressed in terms of the wake skew angle, χ .

$$K = \tan (\chi/2) \quad (6)$$

The induced velocity could thus be written as

$$v(r) = v_0(1 + \bar{r} \tan (\chi/2) \cos \psi) \quad (7)$$

The induced velocity is, therefore, expressed as a function of the blade radius and azimuth position.

The simple vortex theory was further improved by Castles and DeLeeuw and Castles and Durham in references 10 and 11. In their analysis, they employed the same wake shape utilized by Coleman. With numerical integration, the induced velocity normal to the rotor disc was calculated on the lateral rotor axis.

Heyson in a series of papers, references 12-16, improved on the previous simple vortex theories. He removed the uniform loading assumption by modeling the wake as a number of parallel and concentric vortex cylinders. The overall inflow field, representing the radially nonuniform loaded rotor, is obtained by superposition of the respective velocity fields of each vortex cylinder. Consequently, this method yields a symmetrical inflow field about the longitudinal plane of symmetry of the rotor. The calculation of the flow field using the simple vortex theory is greatly complicated by the inclusion of terms representing azimuthal variations in circulation. In reference 14, Heyson developed the equations for all three components of induced velocity at an arbitrary point near the rotor and for an arbitrary harmonic of the azimuthal distribution of circulation. The values for the induced velocity cannot be expressed in closed form, and they are obtained by numerical integration. This process was utilized in obtaining the charts and table of induced velocities in reference 15. In order to obtain a realistic azimuthal load variation, the simple vortex method must utilize numerical integration. Thus, if the computer is required, thought should be given to the more exact lifting-line and lifting-surface theories. The simple vortex theory, even in the most complicated form developed by Heyson, is still based on actuator theory (i.e., infinite number of blades).

The last of the simple vortex inflow theories to be examined is the flat-wake concept. As promulgated in reference 17, the flat-wake theory represents a limiting case where all the vortices transferred to the slipstream of a rotor, moving horizontally at a relatively high speed, are reduced to a single ribbon of vorticity. Baskin et al. made the assumption that for the flat-wake concept, the variation of circulation with azimuth may be neglected, provided that for each blade station the circulation is averaged over a complete rotor revolution. Consequently, the radial change $\Gamma_b(r)$ of the azimuth-averaged blade circulation becomes the only variation to be considered. The assumption of a rigid wake implies that no interaction exists between the induced velocity and the wake structure, thus the problem reverts to a linear problem. In computing the resultant induced velocity, the velocity components generated by the lateral vortices and the longitudinal vortices subsystems forming the wake are computed separately and then superimposed. The induced velocity in the flat-wake theory is not expressed by a closed form equation, but must be determined numerically. In addition, the circulation distribution must be assumed or known prior to induced velocity calculations. The validity of the flat-wake concept is compromised at low μ values, because the deflection of the wake in the vicinity of the disc is large. Ormiston developed a flat-wake concept in reference 18

similar to the previously described flat-wake vortex theory. A general actuator-disc theory was developed for predicting the time averaged induced velocity distribution and the steady state force and moment response of a helicopter rotor in forward flight. A solution was obtained by using the harmonic balance method. The actuator disc theory included blade flapping dynamics. Examination of the harmonic content of the rotor blade flapping moment disclosed that the first harmonic terms, which determine the thrust and moment response of the rotor, are not affected by downwash harmonics higher than the second. Only the first two harmonic of downwash were retained for prediction of rotor thrust and moment response.

2.1.3 Vortex Theories-Finite Number of Blades

An inherent limitation of the simple vortex theories, is that the calculated induced velocities are time-averaged, rather than instantaneous. As noted by Heyson in reference 16, the time-averaged induced velocities give excellent results for rotor/wing interference problems, but are totally inadequate for calculating the blade loads. To satisfactorily determine the instantaneous induced flow field for a rotor with a finite number of blades, the vortex wake from each blade must be considered.

A vortex wake analysis that considers a finite number of helicopter rotor blades was first performed as early as 1929 by Goldstein (19). He determined the flow resulting

from a set of semi-infinite, equidistant, coaxial, helical surfaces, with each surface representing the vortex sheet for each blade of the rotor. The theory of Goldstein was made directly applicable to the hovering helicopter rotor in reference 20 by Lock. The Goldstein-Lock analysis neglects the effects of wake contraction, viscosity, and nonuniform downwash. For years, this method became the classical method of calculating rotor hovering performance and inflow. The advantage of the method was that it entailed minimal computational requirements. However, its usage was outdated with the advent of the high-speed computer as delineated in reference 21. A concise history and description of helicopter rotor wakes is given by Landgrebe and Cheney in reference 22, which has as its primary interest rotor performance.

One of the forerunners of the computerized vortex theories, and one which resulted in nonuniform inflow, was that of Piziali. In references 23 and 24 he calculated the nonuniform inflow for a rotor in hovering and forward flight. An undistorted rigid wake was assumed, and each blade was replaced by a segmented lifting line. The shed and trailing vorticity distributions were represented by a continuous mesh of straight-segmented, vortex filaments originating at the instantaneous position of the blade as shown in figure 3. The strengths Γ_b of the bound vortex

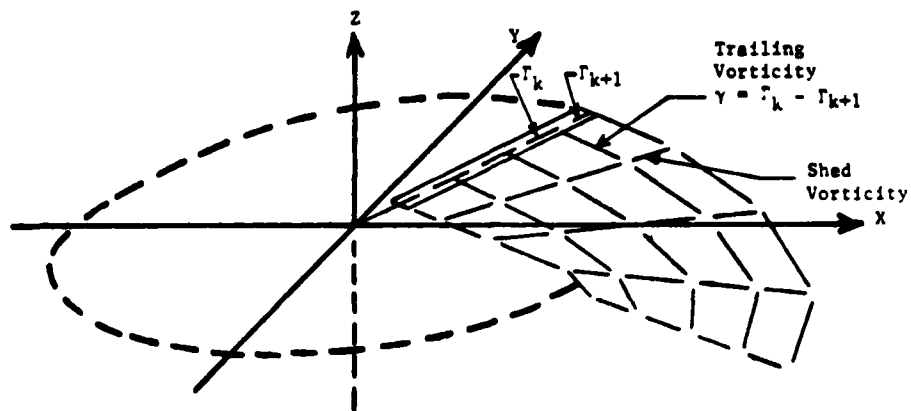


Figure 3. Undistorted Rigid Wake Distribution of the Lifting Line Vortex Theory

elements are considered to be the unknowns, and the computer iterates until a solution for the given flight conditions is obtained. The primary disadvantage of this method is that computer time can become large and that the nonuniform inflow velocities are not time dependent, i.e., although the calculated induced velocities are instantaneous, they do not vary with time. An improved wake model was required because the blade inflow was found to be responsive to wake distortions. This led to the development of the distorted, free-wake analysis and to the empirically-prescribed wake analysis. References 25 through 27 are an exemplification of some of the free-wake computer analyses developed. Generally, the wake from each rotor blade is represented by segmented vortex filaments which are allowed to move or distort freely until wake convergence. No preconceived

assumptions are made regarding the wake shape. Convergence implies that the wake geometry is consistent with the velocity field it induced. In contrast to the rigid-wake method of Goldstein-Lock, which could be managed through classical mathematical techniques, the computational procedure required in the free-wake method could only be accomplished by use of computers.

A conception of the magnitude and complexity of the free-wake inflow analysis is given by reference 28, where it is stated that for a single flight condition of a six bladed rotor, assuming an azimuth increment for the calculations of 30 degrees and each blade represented by 10 filaments, 1000 wake elements were required. This results in the computation of 72 million distortion velocities per flight condition.

As a means of increasing the accuracy of the free-wake analysis and of decreasing the computational time, empirically prescribed wake models were generated. Test of both full scale and model helicopter rotors has shown that the rotor, especially in hover, is heavily influenced by wake distortion effects. Landgrebe, in a series of papers and reports (28-31), describes the prescribed-wake theory. The wake shape is specified for the particular flight condition utilizing the generalized wake equations and wake constants which are derived from experimental data.

The above wake theories are all based on the lifting-line theory, i.e., each blade was modeled by a single bound vortex

filament. This model is justifiable for slender rotor blades, however it may be compromising when employed in representing low aspect-ratio blades. Subsequently, lifting surface theories were developed to improve the physical representation of a rotor blade. A lifting surface theory was used by Johnson and Scully in their calculation of airloads and by Kouarcek and Tangler to determine the performance of a hovering rotor. In reference 32, Johnson and Scully utilized a distorted wake lifting surface theory to determine the variable inflow in their helicopter airloads calculations. Johnson's lifting surface theory (33) was used to calculate vortex induced loads. Scully's method, contained in references 34 and 35, was used to calculate the self-induced distortions of the vortex wake in forward flight.

Kocureck and Tangler in reference 36 developed a prescribed wake, lifting-surface analysis for hovering rotors with low aspect ratio blades. The prescribed-wake method was an extension of Landgrebe's method. Additional data from model studies of low-aspect-ratio blades by Tangler was used to extend the data base. The lifting surface, as detailed in reference 37, is imagined to be formed by a continuous layer of horseshoe-shaped vortices of finite strength. The unknowns in the solution technique are the circulation strengths of each panel. The method of solution is similar to the prescribed lifting line wake theory, except that the boundary conditions must be satisfied. One of the boundary conditions

is that the Kutta condition is satisfied. The second boundary condition is that the circulation distribution must induce normal downwash velocities sufficient to cancel locally the component of the free-stream velocity normal to the blade surface. As with the lifting-line vortex theories, a high-speed computer is required to calculate the induced velocities at each flight condition. Closed-form solutions for the induced velocity distribution are not readily obtainable in the more complicated vortex theories.

2.1.4 Improved Actuator-Disc Theories

The complexity of the vortex theories results in excessive computer time. Recently, much work has been accomplished in the area of improved actuator theories. The concept behind the actuator theory is to provide an approximate induced velocity distribution with a modest computational requirement.

Wood and Hermes in reference 38 developed a method based upon momentum theory for obtaining the induced velocity distribution of a helicopter rotor in forward flight. Their theory determines induced velocity as a function of both blade radius and azimuth. The theory is based upon two simple factors, the first of which is that the induced velocity field of a rotor in hover can be determined by combined blade-element and momentum theory. The second fact is that the induced velocity buildup for a rotor blade subjected to

a sudden change of angle-of-attack is essentially exponential and can readily be approximated by an exponential function, (Carpenter and Fridovich (39)).

Wood and Hermes rationalized that a blade in forward flight is constantly entering undisturbed air thus the induced velocity caused by this blade would increase with time analogous to the sudden change in an angle-of-attack experiment. The total induced velocities are then obtained by superposition. A disadvantage of the theory is that a difficult coordinate transformation is required.

Azuma and Kawachi (40) developed an extended momentum theory that they call "Local Momentum Theory" for helicopter rotor aerodynamics. As derived, the theory is applicable for both steady and unsteady aerodynamic problems because it calculates the mean induced velocity and also the instantaneous induced velocity. The theory is based on the instantaneous momentum balance with the blade elemental lift at a local station of the rotor rotational plane. The rotor blade is considered to be decomposed into a series of wings, each of which has an elliptical circulation distribution and is so arranged that a tip of each wing is aligned to the blade tip. Azuma and Kawachi state that the computational time of their theory is about one tenth to one hundredth of that of the vortex theory. Stricker and Gradl (41) have developed a semi-empirical downwash model which combines momentum theory with properties of the vortex

wake model to calculate the radial and azimuth variation of the rotor inflow. The semi-empirical downwash model is based on the principle of superposition. The basic inflow model, for both hover and forward flight, is that calculated by the method of Wood and Hermes (38). The basic inflow model is then adjusted by adding wake contraction and tip loss effects. The wake contraction is simulated by a wake of up to 4 rings of vortices where the wake geometry is taken from Landgrebe's prescribed wake model of reference 29. Tip losses are simulated by an increase of induced velocity as proposed by Prandtl. Then, the induced velocity portions from modified blade element momentum theory, from wake contraction simulation, and from tip loss calculation are summed to obtain the local induced velocity as shown in figure 4.

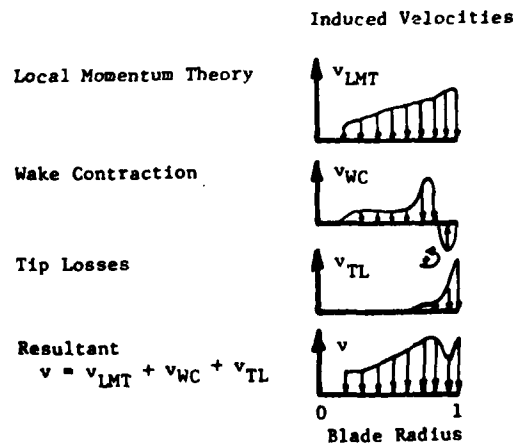


Figure 4. The Semi-Empirical Induced Velocity Superposition Theory of Stricker and Gradl.

Stricker and Gradl state that their semi-empirical method requires 0.2 to 1.0 minutes to get a trim solution, while the free wake analysis requires 2 to 20 minutes.

Mangler and Squire (42) in the late 1940's adapted the velocity and acceleration potential concepts to the determination of the induced velocity field of a rotor. They were able to determine the mean induced velocities in forward flight by assuming a pressure distribution across the rotor disc. The helicopter rotor was assumed to be lightly loaded and was composed of an infinite number of blades. The rotor was assumed to be replaced by a circular disc with a pressure step between the faces. Consequently, the thrust of the rotor is equivalent to the discontinuity in pressure forces between the two faces of the disc.

Mangler and Squire also showed that the Laplace equation, $\nabla^2 P = 0$, and the continuity equation, $\text{div } V = 0$, must be satisfied everywhere in the flow field. Solution of the Laplace equation is found in terms of Legendre functions of the elliptic coordinates associated with the disc. These are discontinuous between the two faces of the disc but continuous everywhere else. To simplify the math, only the case of an axially-symmetric load distribution was considered (i.e., load was only a function of radius and not azimuth position). The rotor loading distribution is expanded in a series of Legendre functions, so that the first term produces the entire thrust T and the rest of the series

produces only variations in the load distribution. Three different pressure distributions are obtained. Pressure distribution I is an elliptic load distribution. The second term of the series yields the second pressure distribution which is solely used as an intermediate step to the third pressure distribution. Pressure distribution III, which is a linear combination of pressure distribution I and II, was selected such that the thrust vanishes both at the center and edge of the rotor disc. This is a very good approximation for the actual thrust distribution on a rotor.

Figures 5 and 6 depict the induced velocity distribution along the longitudinal and lateral plane of symmetry respectively. The induced velocity was calculated using pressure distribution III and the measured data was obtained from reference 12. The correlation of the measured data with the calculated induced velocity distribution of pressure III is good. Stepniewski, in reference 6, shows that the average value of induced velocity from Mangler and Squire's theory is the same as obtained by Glauert in reference 1 (equation 2 of this paper).

Joglekar and Loewy (43), in an attempt to improve blade-response and blade-airload calculations, extend the theory of Mangler and Squire. They develop expressions for relating the assumed pressure field of the rotor disc to the total aerodynamic thrust and the total steady pitching and rolling moments attributable to the rotor. They also successfully

relate the assumed pressure distribution to the time-dependent aerodynamic rotor blade flapping moments. The modified actuator-disc theory was used to provide a more realistic wake-geometry into the classical, vortex-wake program of Piziali (references 23 and 24). An improved lift distribution is developed in order to get a better approximation to the time-averaged induced velocity field.

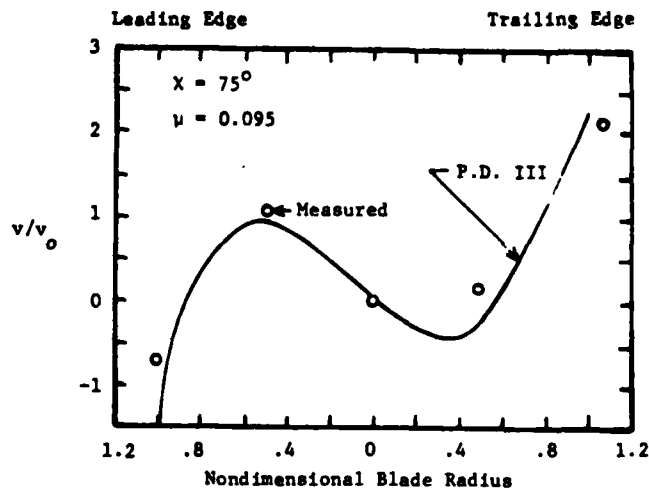


Figure 5. Comparison of Measured and Mangler-Squire's Calculated Values of Induced Velocity Along the Rotor Longitudinal Axis

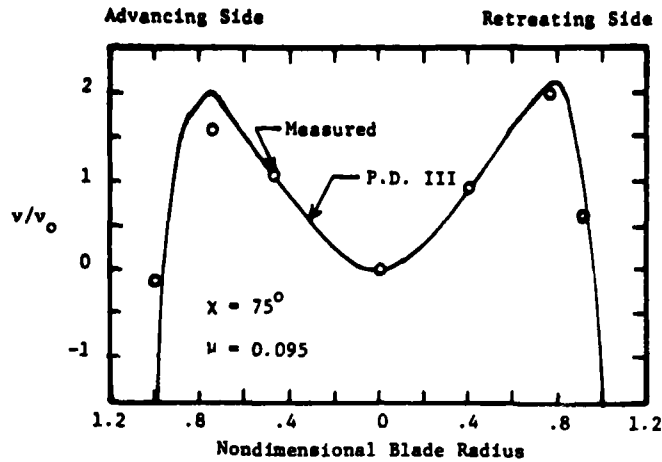


Figure 6. Comparison of Measured and Mangler-Squire's Calculated Values of Induced Velocity Along the Rotor Lateral Axis.

An ellipsoidal coordinate system is utilized in the solution of the three dimensional Laplace's equation. The pressure distribution in its general form is given by

$$P = \sum_{\substack{m, n \\ m < n}}^{\infty} P_n^m(v) \cdot Q_n^m(in) \cdot \{C_n^m \cos(m\psi) + D_n^m \sin(m\psi)\} \quad (8)$$

Joglekar and Loewy drop all combinations of m, n in the equation that result in an even $(m + n)$ because $P_n^m(v)$ will be even if $(m + n)$ is even. An even $P_n^m(v)$ will yield a nonphysical pressure distribution. The coefficients for equation (13), C_1^0 , C_3^0 , C_2^1 , and D_2^1 , are calculated in terms of rotor thrust, pitching moment and rolling moment.

Joglekar and Loewy also developed a method of expressing the coefficients C_n^m and D_n^m in terms of flapping moments

experienced by the blades. The induced velocity was subsequently determined by numerical integration. Again we note that the induced velocities in the more complex actuator disc theories are incapable of being represented by a closed form solution.

2.2 DYNAMIC INFLOW THEORIES

Recent research has demonstrated that the low-frequency properties of the helicopter rotor wake can have a significant effect on the rotor control power, dynamic response, and stability. An integral part of this research has been the development of various inflow models that characterize the low-frequency rotor wake. It is these theories that we categorize as dynamic inflow models. Table 1 is a chronological list of the research and literature that pertain to the concept of dynamic inflow. The early work, prior to 1970, will be discussed in a general fashion. The more recent work will be presented in greater detail so as to develop the foundations for this research.

2.2.1 Early Work

Amer, reference 44, developed a theory to predict the pitch and roll damping of a rotor. He disclosed that the damping decreases with increasing blade pitch. Sissingh (2) noted that for extreme inflow conditions, uniform momentum theory did not adequately predict rotor damping when compared to experimental data. He postulated that this discrepancy was due to changes in induced velocities caused by transient

TABLE 1
Dynamic Inflow History

RESEARCHERS	YEAR	THEORY	STEADY	UNSTEADY	REMARKS
AMER	1948	MOMENTUM	X		ROTOR DAMPING IS FUNCTION θ
SISSINGH	1952	MOMENTUM	X		ROTOR DAMPING FUNCTION OF INFLOW λ
CARPENTER & FRIDOVICH	1953	MOMENTUM	X	X	INTRODUCED APPARENT MASS. USED 3 EQS AND 3 UNKNOWNNS
LOEWY	1957	VORTEX	X	X	2 DIMENSIONAL LIFT DEFICIENCY FUNCTION
REBONT	1960	MOMENTUM	X	X	2 EQS AND 2 UNKNOWNNS DID NOT CONSIDER FLAPPING
TARARINE & DELEST	1960	VORTEX	X	X	SINUSOIDAL AND STEP INPUTS. NEGLECTED APPARENT MASS FOR TWO BLADE ROTOR
MILLER	1962	VORTEX	X		THREE DIMENSIONAL WAKE GEOMETRY. STEP INPUT
JONES	1965	VORTEX	X		TRIED TO OBTAIN CLOSED FORM SOLUTION
SEGEL	1965	VORTEX	X		RIGID WAKE, TRAILING VORTICES ONLY. BLADE LOADS
SHUPE	1970	MOMENTUM	X		EQUIVALENT LOCK NUMBER γ^*
KUCZYNSKI & SISSINGH	1971		X	X	MEASURED HINGELESS ROTOR RESPONSE
ORMISTON & PETERS	1972	MOMENTUM & VORTEX	X		DERIVED $[L]$ AND $[L]$ EMPIRICAL
CREWS HONENHESER & ORMISTON	1973	MOMENTUM	X	X	IDENTIFIED INFLOW GAIN AND TIME LAG
SHIPMAN	1974	VORTEX	X		CALCULATED ROTOR STABILITY DERIVATIVES
PETERS	1974	MOMENTUM	X	X	UNSTEADY $[L]$ AND $[L]$ EMPIRICAL
AZUMA	1974	LOCAL MOMENTUM	X	X	EXPERIMENTAL
CREWS SANEJEE & HONENHESER	1977	MOMENTUM	X	X	PARAMETER IDENTIFICATION OF ROTOR WAKE

changes in the rotor thrust. The lift distribution and induced velocity were each formulated as a Fourier series with the first harmonic sine and cosine terms. It was reasoned that the lift of the rotor varies with azimuth angle causing corresponding changes in the induced velocity. Sissingh shows that the induced velocity distribution results in an increase in damping in autorotation and a loss in damping for helicopter flight, especially at higher tip speed ratios or in climbing flight.

Other researchers reasoned that the time rate of change of thrust perturbations would affect the magnitude of the transient changes in the velocity field of the rotor. From the point of view of the momentum theory, a time interval must elapse during which the air mass associated with the rotor is accelerated to its new steady state inflow. Carpenter and Fridovich (39) measured the response of a hovering rotor to rapid changes in collective pitch, and they correlated their experimental data with a modified momentum theory that they developed. Their experiments disclosed that the time lag between full pitch and full induced velocity was less than one second. They assumed that the uniform induced velocity of the initial flow field is analogous to the flow field produced by an impermeable disc which is moved normal to its plane. The apparent mass of the fluid associated with an accelerating impermeable disc was found to be 64 percent of the mass of the fluid in the

circumscribed sphere. A certain part of the transient thrust was directly attributable to the acceleration of the apparent mass which they included in the classical momentum theory. Rotor thrust was expressed as a function of induced velocity, blade flapping, and the rotor hub vertical motion. This yielded three equations to be solved simultaneously. The inclusion of blade flapping and hub motion, however, greatly complicated the analysis. Tip loss effects were included by integration of thrust only up to 97 percent of the geometric blade radius. Even with the inclusion of a tip loss, the calculated thrust coefficients were 10 percent greater than the actual measured thrust.

Rebont, in a series of papers (45-47) experimentally measured the response of a rotor to an increase in collective pitch during vertical flight. He showed, as did Carpenter, that the thrust response is highly sensitive to the rate of change of the collective pitch. Although Rebont's analysis neglected rotor blade flapping, he used Froude momentum theory in conjunction with blade-element theory and developed (from the charts of Oliver) induced velocity relations for descending flight. This resulted in an equation in the form of a Riccati differential equation which included an apparent mass term to describe the thrust perturbations. An interesting anomaly was that Rebont had to double Carpenter's apparent mass term to correlate the experimental data with his analysis.

Loewy, reference 48, investigated unsteady wake effects on rotor lift. He developed a two-dimensional, lift-deficiency function that is based on classical nonstationary flow theory. This theory accounts for both the reduction in lift and the phase shift due to the shed wake. Miller (49) used a rigid-wake concept to develop a lift-deficiency function similar to the aspect-ratio effect of finite wing theory. Miller states that the apparent mass effects are lost in the lifting-line approximation, but that they can be included separately by increasing the effective moment of inertia of the blade. Along this same line Jones (50) develops an actuator-disc theory that takes into account the shed vorticity in the wake. His model provides a "closed-form" solution for the aerodynamic damping in the vicinity of hover. Jones also shows that the Miller and Loewy lift-deficiency functions are equal in hover. Tararine and Delest (51) tried to relate static lift to dynamic lift by a mathematical transformation of static lift which takes into account the amplitude and phase modifications. From photographs of smoke trails, they developed their formula based on the rotor circulation. They neglected the apparent mass for a two-bladed rotor system because it was small compared to their blade shape parameter.

Segel (52) developed a method (based on Piziali's classical-wake computer program, references 23 and 24) to predict the nonperiodic air loads caused by collective

inputs to a helicopter in forward flight. Piziali's wake program was modified to yield a temporal and spatial history of rotor response variables as functions of time-varying changes in collective pitch. The calculated flapping and air-load distribution compared favorably with transient data obtained in wind-tunnel tests of a full-scale helicopter rotor. Segel claimed that the apparent mass approach of either Carpenter or Rebont was sufficient to relate the time-varying total thrust on a blade or rotor to the time variation of blade pitch. However, the apparent mass method was not considered suitable for computing the inflow distribution required to determine the blade loadings as a function of spanwise location, azimuth position, and time. He theorized that it was necessary to compute the inflow caused by a wake possessing elements of vorticity whose strengths vary nonperiodically as a direct result of the time-varying change in collective pitch. The following assumptions were made by Segel to simplify the analysis

- (1) The rotor blades were assumed to be structurally rigid with only a flapping degree of freedom.
- (2) The hub of the rotor continued to translate in level, constant speed flight during the short time interval that collective pitch is varied.
- (3) The geometry of the wake was specified a priori; the transient-wake model employed only trailing vortex elements.

- (4) No account was taken of the shed vorticity in the wake.

2.2.2 Recent Work

The majority of the previous work was directed at obtaining improved blade loading calculations. The more recent dynamic inflow theories that have been developed are directed at improving rotor response and stability calculations. Shupe (53) follows the previously mentioned work of Sissingh and notes that perturbations in rotor lift (due to either control inputs or blade dynamics) can create perturbations in the induced flow which, in turn, create alterations in the expected lift perturbations. Shupe's analysis shows that for cases in which quasi-steady momentum theory is applicable, the reduction in expected lift can be accounted for by the use of a reduced (i.e., equivalent) Lock number. The equivalent Lock number is used by Shupe for the calculation of rotor control derivatives. The equivalent Lock number for forward flight is expressed as

$$\gamma^* = \frac{\gamma}{1 + a\sigma/8\mu} \quad (9)$$

Sissingh and Kuczynski in a series of reports, references 54-57, measure the steady-state and frequency-response characteristics of a variety of hingeless rotors. Rotor responses were found with respect to collective pitch, longitudinal and lateral cyclic pitch, and angle of attack

variations. A wide range of flight conditions was tested, which included high and low advance ratios and lightly and heavily loaded rotors. The rotor derivatives were found to be more linear at higher lift levels and high advance ratios. It was apparent from these tests that the rotor control power and damping did not agree with values calculated from the classical steady inflow theories.

Azuma, reference 58, develops a method of calculating the pitch damping of helicopter rotors utilizing nonuniform inflow. Azuma notes that classical rotor damping derivatives for pitch and roll sometimes result in overestimated values for the actual rotor damping, specifically for hingeless rotor systems in hover or low μ and C_T forward flight. The theoretical inaccuracies are assumed to arise from inadequate assumptions of the induced flow distribution and the treatment of pertinent flapwise motion of the blade. A theoretical method of estimating pitch and roll damping based on the simple momentum theory is developed by taking into account the nonuniformity of the induced-flow distribution. The nonuniform induced velocity is assumed to have an inclined funnel-shape distribution. Experimental tests conducted by Azuma showed that the pitch damping is still overestimated by his nonuniform inflow theory. Azuma also applies his "Local Momentum Theory" in reference 40 to the unsteady aerodynamic problems of the helicopter rotor in the low-frequency range. In particular, he used his method to

examine the response of rotor thrust and blade flapping motion to a sudden change of collective pitch. The theory did not consider the additional apparent mass term of air associated with blade pitching and flapping motion. Thus, the theory is only applicable to unsteady aerodynamic problem of the rotor in the range of very low frequencies, and is not applicable to more rapid changes.

Shipman (59) modified Sadler's free-wake analysis, references 26 and 27, to determine the wake effects on the stability and control derivatives for various rotor systems. The control derivatives were assumed to be changes in thrust, power required, rolling moment, and pitching moments at the hub due to perturbations in the blade pitch settings. In the analysis, the blade-loading and response are coupled together; and iterations are carried out until the two are compatible. It was shown that the wake had only a slight effect on most of the stability and control derivatives for the articulated, single-rotor system. However, the wake becomes significant in or near hover.

Ormiston and Peters, reference 60, employ a quasi-steady momentum theory and an extended equivalent Lock-number approach to calculate the control derivatives of a hingeless rotor in hover and in forward flight. They express the induced inflow of a rotor by a truncated Fourier series shown in equation (10), where λ_0 is the uniform inflow ratio of momentum theory.

$$\lambda_i = \lambda_o + \lambda_s \sin\psi + \lambda_c \cos\psi \quad (10)$$

They assume a linear relationship between perturbations of the inflow components and perturbations of the rotor thrust and moments.

$$\begin{bmatrix} d\lambda_o \\ d\lambda_s \\ d\lambda_c \end{bmatrix} = \begin{bmatrix} \frac{d\lambda_o}{d(C_T/a\sigma)} & \frac{d\lambda_o}{d(C_L/a\sigma)} & \frac{d\lambda_o}{d(C_M/a\sigma)} \\ \frac{d\lambda_s}{d(C_T/a\sigma)} & \frac{d\lambda_s}{d(C_L/a\sigma)} & \frac{d\lambda_s}{d(C_M/a\sigma)} \\ \frac{d\lambda_c}{d(C_T/a\sigma)} & \frac{d\lambda_c}{d(C_L/a\sigma)} & \frac{d\lambda_c}{d(C_M/a\sigma)} \end{bmatrix} \begin{bmatrix} d\frac{C_T}{a\sigma} \\ d\frac{C_L}{a\sigma} \\ d\frac{C_M}{a\sigma} \end{bmatrix} \quad (11)$$

Equation (11) can be rewritten in matrix notation as

$$\{d\lambda\} = [L] \{dF\} \quad (12)$$

The column matrices $\{dF\}$ and $\{d\lambda\}$ represent perturbations of the generalized rotor forces and inflow components respectively, while matrix $[L]$ is the nonuniform induced inflow matrix. Simple momentum theory is used to develop an inflow model for hover and forward flight.

$$[L]_{\text{hover}} = \frac{a\sigma}{\lambda_o} \begin{bmatrix} 1/4 & 0 & 0 \\ 0 & -3/4 & 0 \\ 0 & 0 & -3/4 \end{bmatrix} \quad (13)$$

$$[L]_{\text{forward flight}} = \frac{a\sigma}{\mu} \begin{bmatrix} 1/2 & 0 & 0 \\ 0 & -3/2 & 0 \\ 0 & 0 & -3/2 \end{bmatrix} \quad (14)$$

A second method, based on the simple vortex system is also used to find the L matrix in forward flight. A bound vortex is located at the lateral axis with two trailing vortices extending rearward in the plane of rotation. The results are

$$[L]_{\text{vortex}} = \frac{a\sigma}{\mu} \begin{bmatrix} 1/2 & 0 & 1 \\ 0 & -8/3 & 0 \\ 1/2 & 0 & 0 \end{bmatrix} \quad (15)$$

Various combinations of equations (14) and (15) were investigated, and a final form

$$[L]_{\text{combined}} = \frac{a\sigma}{\mu} \begin{bmatrix} 1/2 & 0 & 0 \\ 0 & -3/2 & 0 \\ 1/2 & 0 & 0 \end{bmatrix} \quad (16)$$

was found to give the best agreement with experimental data of references 54-57. However, for the definition of [L] in equation (16), $[L]^{-1}$ does not exist as opposed to the [L] matrices of equation (14) and (15) which have well-behaved inverses.

The above inflow theory can be incorporated in a rotor-response program as follows. The steady-state

components of the thrust and moment response are expressed in terms of the control input parameters. This relation is expressed in matrix notation as

$$\{dF\} = [M]\{d\theta\} + [N]\{d\lambda\} \quad (17)$$

The matrices $[M]$ and $[N]$ are the rotor response partial derivatives from the generalized harmonic balance method where

$$[M] = \begin{bmatrix} \frac{\delta(C_T/a\sigma)}{\delta\theta_o} & \frac{\delta(C_T/a\sigma)}{\delta\theta_o} & \frac{\delta(C_T/a\sigma)}{\delta\theta_c} \\ \frac{\delta(C_L/a\sigma)}{\delta\theta_o} & \frac{\delta(C_L/a\sigma)}{\delta\theta_s} & \frac{\delta(C_L/a\sigma)}{\delta\theta_c} \\ \frac{\delta(C_M/a\sigma)}{\delta\theta_o} & \frac{\delta(C_M/a\sigma)}{\delta\theta_s} & \frac{\delta(C_M/a\sigma)}{\delta\theta_c} \end{bmatrix} \quad (18)$$

$$[N] = \begin{bmatrix} \frac{\delta(C_T/a\sigma)}{\delta\lambda_o} & \frac{\delta(C_T/a\sigma)}{\delta\lambda_s} & \frac{\delta(C_T/a\sigma)}{\delta\lambda_c} \\ \frac{\delta(C_L/a\sigma)}{\delta\lambda_o} & \frac{\delta(C_L/a\sigma)}{\delta\lambda_s} & \frac{\delta(C_L/a\sigma)}{\delta\lambda_c} \\ \frac{\delta(C_M/a\sigma)}{\delta\lambda_o} & \frac{\delta(C_M/a\sigma)}{\delta\lambda_s} & \frac{\delta(C_M/a\sigma)}{\delta\lambda_c} \end{bmatrix} \quad (19)$$

The physical control inputs $\{d\theta\}$ are considered independent parameters while the inflow components are treated as dependent variables related to the thrust and moment response of the rotor by equation (11). Equations (11) and (17) are

combined to yield the generalized rotor response forces

$$\{dF\} = [M']\{d\theta\} \quad (20)$$

The matrix $[M']$ is comprised of the rotor response partial derivatives and nonuniform induced inflow. Matrix $[M']$ is expressed explicitly as

$$[M'] = \left[I - [N][L] \right]^{-1} [M] \quad (21)$$

Ormiston and Peters show that, given both experimental measurements of the rotor response derivatives $[M']$ and the theoretical partial derivatives for the control and inflow inputs $[M]$ and $[L]$, equation (21) can be manipulated to yield an empirical inflow matrix $[L]$.

$$[L_E] = [N]^{-1} \left[I - [M][M']^{-1} \right] \quad (22)$$

The empirical model assumes linear but coupled relationships between the three induced flow distributions (uniform, side-to-side, and fore-to-aft) and the three loading conditions (thrust, roll moment, and pitch moment). The nine coupling derivatives were chosen to give the best fit of the experimental data of references 54-57. These are given in Table 2.

From their test data, Ormiston and Peters confirm that the induced flow perturbations have a large effect on control derivatives. They also conclude that momentum theory adequately predicts all the response derivatives in hover, and

TABLE 2
Empirical L-Matrix

*element/ μ	.1	.2	.3	.4	.5	Momentum Theory
L_{11}	+0.50	0.50	0.60	0.90	1.40	0.5
L_{12}	+0.30	+0.30	+0.30	+0.30	+0.50	0
L_{13}	0	0	-0.30	-1.00	-1.65	0
L_{21}	0	0	0	-0.10	-0.95	0
L_{22}	-6.60	-6.60	-6.70	-6.90	-7.30	-2.0
L_{23}	+1.35	+1.35	+1.35	+1.60	+2.20	0
L_{31}	0.55	0.55	0.55	0.55	0.55	0
L_{32}	-1.50	-1.50	-1.70	-1.85	-2.00	0
L_{33}	0	0	0	0	0	-2.0

*Each entry must be divided by v to give the element of L .

adequately predicts some of the forward flight derivatives. For the other derivatives in forward flight, momentum theory was found to be inadequate. Using the empirical inflow matrix $[L_E]$, the accuracy of the predicted responses improved beyond those obtained using the momentum and vortex $[L]$ matrix. An additional point, not noticed in reference 60 but mentioned in reference 61, is that $[L]^{-1}$ for the empirical model does not exist at the point $\mu = .32$.

The nonuniform inflow theory of reference 60 is extended to include unsteady rotor dynamics in references 62 and 63. In reference 62 an unsteady dynamic rotor hovering wake is modeled as an approximate steady-state wake with a time lag. The wake model is derived from the hovering unsteady moment of momentum equation. The effect of the dynamic inflow is shown to be equivalent to replacing the Lock number by an unsteady equivalent Lock number for the special case of harmonic inputs.

$$\gamma^* = \gamma / \{1 + B^4 \gamma L / 8(1 + i\omega_f \tau)\} \quad (23)$$

The inflow gain L and time constant τ were selected by parameter identification to obtain a reasonable fit of the test data.

The unsteady inflow theory is extended by Peters in reference 63 to encompass more general inflow models. The total inflow of the rotor as previously given by equation (10) is modified to include unsteady effects and a linear

variation with rotor radius. The unsteady, nonuniform inflow is approximated by equation (24).

$$\lambda(r, \psi) = \bar{\lambda} + \{\lambda_o + \lambda_s \bar{r} \sin \psi + \lambda_c \bar{r} \cos \psi\} e^{i\omega\psi} \quad (24)$$

The steady portion of the total inflow λ contains contributions from the free stream velocity, $V/\Omega r$, and from the steady induced flow, v , due to rotor thrust. The unsteady inflow components λ_o , λ_s , λ_c contain contributions from harmonic plunging $ze^{i\omega\psi}$, rolling $\phi e^{i\omega\psi}$, and pitching $\alpha e^{i\omega\psi}$, of the shaft, as well as contributions from the unsteady induced flow components v_o , v_s , v_c due to perturbations in rotor thrust and moments. The total induced flow is analogously expressed as

$$v = \bar{v} + (v_o + v_s \bar{r} \sin \psi + v_c \bar{r} \cos \psi) e^{i\omega\psi} \quad (25)$$

Where \bar{v} is the induced flow contribution from the steady rotor thrust. The blade pitch angle θ is expressed in terms of a steady value $\bar{\theta}$ and control system perturbations θ_o , θ_s and θ_c as delineated in equation 26.

$$\theta = \bar{\theta} + (\theta_o + \theta_s \bar{r} \sin \psi + \theta_c \bar{r} \cos \psi) e^{i\omega\psi} \quad (26)$$

With the assumption that the rotor inflow perturbations λ_o , λ_s , λ_c are small compared with unity, it follows that the induced flow perturbations v_o , v_s , v_c and control perturbations θ_o , θ_s , θ_c , Z , ϕ , α are also small quantities which results in linear perturbation equations. Peters

follows previous investigators, i.e. Carpenter, Azuma, Crews and Hohenemser, and reasons that the apparent mass terms of a lifting rotor must be written in terms of the reaction forces (or moments) on an impermeable disc which is instantaneously accelerated (or rotated) in still air. The reactions for an impermeable disc are obtained from potential flow-theory in terms of elliptic integrals yielding an apparent mass and inertia values of

$$m_A = \frac{8}{3} \rho R^3 \quad I_A = \frac{16}{45} \rho R^5 \quad (27)$$

These values for apparent mass and inertia represent 64 percent of the mass and 57 percent of the rotary inertia of a sphere of air having radius R. The steady induced-flow equation and the unsteady, induced-flow perturbation equation are integrated and yield the following results

$$C_T = 2\bar{v} \sqrt{\mu^2 + \lambda^2} + 2v\dot{v}_O + K_m \dot{v}_O \quad (28a)$$

$$-C_L = 1/2v\dot{v}_S + K_I \dot{v}_S \quad (28b)$$

$$-C_M = 1/2v\dot{v}_C + K_I \dot{v}_C \quad (28c)$$

The first term in equation (28a) is the steady thrust term of the rotor and is used to calculate the steady induced flow v given λ , μ and C_T . The second two terms in equation (28a) are the thrust perturbation components, while equations (28b) and (28c) represent the pitch and rolling

moment perturbation equations. The parameters K_m and K_I are, respectively, the nondimensional apparent mass and inertia terms of an impermeable disc and have values of

$$K_m = \frac{m_A}{\rho \pi R^3} = \frac{8}{3\pi} = 0.8488 \quad (29a)$$

$$K_I = \frac{I_A}{\rho \pi R^5} = \frac{16}{45\pi} = 0.1132 \quad (29b)$$

The time constants associated with the induced flow model utilized in equation (28) are

$$\tau_m = \frac{K_m}{2v} = 0.4244/v \quad (30a)$$

$$\tau_I = \frac{2K_I}{V} = 0.2264/v \quad (30b)$$

and the flow parameter, v , is given by

$$v = \{\mu^2 + \bar{\lambda}(\bar{\lambda} + \bar{v})\}/(\mu^2 + \bar{\lambda}^2)^{1/2} \quad (31)$$

A harmonic balance yields the resulting complex nonuniform induced flow matrix, $[L]$, for unsteady momentum theory.

$$[L(K)] = \begin{bmatrix} \frac{\sigma a}{2v + K_m i \omega} & 0 & 0 \\ 0 & \frac{-\sigma a}{v/2 + K_I i \omega} & 0 \\ 0 & 0 & \frac{-\sigma a}{v/2 + K_I i \omega} \end{bmatrix} \quad (32)$$

An unsteady empirical model analogous to that of reference 60, is developed in reference 63. The empirical flow model of reference 60, $[L_E]$, is utilized for the quasi-steady portion of the induced flow law, while the apparent mass terms rendered from the potential flow theory, are used for the unsteady portion of the induced flow. The resulting empirical unsteady inflow matrix is written below.

$$[L(K)]_E = \left[\begin{bmatrix} K_m & 0 & 0 \\ 0 & -K_I & 0 \\ 0 & 0 & -K_J \end{bmatrix} \frac{i\omega}{\sigma a} + [K_E] \right]^{-1} \\ = [L_E] \left[\begin{bmatrix} K_m & 0 & 0 \\ 0 & -K_I & 0 \\ 0 & 0 & -K_J \end{bmatrix} \frac{i\omega}{\sigma a} + I \right]^{-1} \quad (33)$$

Where $[K_E] = [L_E]^{-1}$. It should be noted that in order to obtain the empirical unsteady L-matrix, the steady empirical L_E matrix need not be invertible. Thus, $[L_E(K)]$ exists at $\mu = .32$, despite the singularity of L_E . By using a single harmonic balance of the root moment equation, Peters also develops a complex equivalent Lock number γ^* as another method of accounting for the unsteady induced flow.

$$\frac{\gamma^*}{\gamma} = 1 - \frac{1}{1 + 8v/\sigma a + 16K_I i\omega/\sigma a} \quad (34)$$

It is readily seen from the above equation, that one effect of induced flow perturbations is to decrease the effective Lock number, (i.e. to decrease the aerodynamic effectiveness).

The dynamic inflow model is used successfully by Ormiston in conjunction with an eigen analysis for the case of blade flapping dynamics of a hovering rotor in reference 64. Ormiston further went on to show in this reference that the dynamic-inflow effects change the transient behavior of rotor flapping dynamics at low collective pitch, where rotor thrust and the mean inflow are small. Peters and Gaonkar in references 61 and 65 examine the effects of the dynamic inflow model on the flap-lag dynamic stability of a helicopter rotor. They find that, when lead-lag motions are included, the equivalent lock number must be augmented by an equivalent drag coefficient, C_{do}^* .

Banerjee, Crews, and Hohenemser (66-67) used parameter identification from transient rotor response tests to determine the dynamic inflow characteristics without performing flow measurements. Two different analytical inflow models were used. The first was the equivalent Lock number and the second was the $[L]$ matrix from unsteady momentum inflow. They had difficulty in identifying the (1,1) term of the $[L]$ matrix and the K_m term. Both of these terms are associated with the average induced velocity, v_o . Their results showed that at low advance ratios, the $[L]$ matrix model gives a better prediction of the flapping response than does the γ^* model.

The synopsis of the inflow theories shows that the theories range from the simple static momentum theory to

the more complex wake-vortex and dynamic, nonuniform-inflow theories. The most promising static theories are the complex actuator theories of Mangler-Squire and Joglekar-Loewy. The static actuator theories provide good correlation of the mean velocity inflow both along the longitudinal and lateral axis. The dynamic inflow models that are based on momentum theory are shown to correlate well with experimental data for the hover condition. Momentum theory does not satisfactorily model dynamic inflow in forward flight. The various inflow theories: momentum, simple vortex, flat vortex wake, local momentum, Goldstein Classical Wake, Piziali Rigid Wake, Free Wake, Prescribe-Wake and Mangler-Squire Actuator Disc contain the necessary components to model the dynamic inflow of hingeless rotors. However, the primary utilization of these diverse inflow theories has been in the realm of rotor-performance verification and prediction (and a subsequent coupling with computer programs for calculating detailed rotor blade loads). To date, the majority of these inflow theories have not been exercised to determine the overall dynamic inflow characteristics of a rotor. Ormiston (18), Segel (52), and Shipman (59) attempt somewhat to determine the overall dynamic inflow characteristics, but fall short of this goal. In all cases, the inclusion of blade dynamics over-complicate the problem and mask the true objective of the dynamic inflow theory. The purpose of this research is to manipulate various inflow theories, without inclusion of associated blade dynamics, to obtain the pure dynamic inflow characteristics.

3. MATHEMATICAL FORMULATION OF INFLOW MODELS

Two distinct inflow models are utilized to obtain the dynamic inflow characteristics of a helicopter rotor. The first inflow theory considered is the actuator-disc theory developed by Mangler-Squire and extended by Joglekar-Locwy. The second aspect of the research utilizes the prescribed-vortex, wake-inflow computer program of Piziali-Landgrebe.

These two inflow theories are vastly different in their basic assumptions and solution procedures. However, both of the models are capable of being extended to provide dynamic inflow characteristics of a rotor. The use of two diverse theories allows a comparison of the various assumptions of each theory, and their effects on dynamic inflow.

The mathematical modifications to the inflow theories are discussed in detail in this section. The first theory to be considered is the actuator-disc theory which is extended to model steady and unsteady aerodynamics.

3.1 ACTUATOR-DISC THEORY

3.1.1 Steady Aerodynamics

The actuator disc theory of Mangler-Squire is re-structured along the lines of Peters' dynamic-inflow theory. The general expression for the lift distribution of Mangler-Squire is given by equation (8). We have previously discussed the general criteria for the selection of the constants

C_n^m and D_n^m . By choosing the constants wisely, one is able to model any rotor thrust condition. The method utilized to choose the constants C_n^m and D_n^m for this proposed research will now be described in more detail.

Equation (35) is the expanded form of the pressure distribution, equation (8), and is utilized in the actuator-disc research.

$$\begin{aligned} \phi = \frac{p}{\rho V^2} = & P_1^0(v) Q_1^0(in) C_1^0 + P_3^0(v) Q_3^0(in) C_3^0 \\ & + P_2^1(v) Q_2^1(in) [C_2^1 \cos \psi + D_2^1 \sin \psi] \\ & + P_4^1(v) Q_4^1(in) [C_4^1 \cos \psi + D_4^1 \sin \psi] \\ & + P_3^2(v) Q_3^2(in) [C_3^2 \cos 2\psi + D_3^2 \sin 2\psi] \end{aligned} \quad (35)$$

The nondimensional pressure distribution, ϕ , is expressed in terms of an ellipsoidal coordinate system. The ellipsoidal coordinate system allows development of a pressure distribution that solves the Laplace equation with a pressure discontinuity at a circular disc. It will be shown that this pressure distribution can be used to yield the induced velocity.

Besides the ellipsoidal coordinate system, we define both the cartesian coordinate system X, Y, Z , which is parallel to the forward velocity streamlines, and the X', Y', Z' coordinate system, which is located on the rotor disc. Following the convention of Mangler and Squire, the coordinate

system is nondimensionalized on the rotor blade or disc radius. Appendix 7.1 contains all the coordinate system transformations as well as the figures that depict the relations between the coordinate systems.

The constants C_n^m and D_n^m are obtained by judicious application of physical boundary conditions concerning the lift on the rotor disc. Over the area of the rotor disc, the lift density will correspond to the difference in the pressure p just below the disc surface ($\eta=0, v<0$) and above the disc ($\eta=0, v>0$). Thus, the equation for the thrust of the rotor disc is

$$T = \int_{\text{lower}} p dA - \int_{\text{upper}} p dA \quad (36)$$

The pressure p is given in general form by equation (8) and when combined with equation (36) yields

$$T = \sum_{\substack{m,n \\ m < n}} \rho V^2 \left[\int_0^{2\pi} (C_n^m \cos m\psi + D_n^m \sin m\psi) d\psi \right] \int_0^R P_n^m(v) Q_n^m(i0) r dr \quad (37)$$

(lower - upper)

It should be noted that the thrust is obtained by integrating on the disc surface; consequently, $\eta=0$ in equation (37). In equation (37), the terms $P_n^m(v)$ and $Q_n^m(in)$ are Legendre Polynomials of the "first" and "second" kind respectively. Appendix 7.2 list the Legendre polynomials used in this segment of the research and some of their associated properties.

This appendix also contains plots of the $P_n^m(v)$ distributions on the rotor disc and the $Q_n^m(in)$ variations with n . The thrust equation in its present form can be integrated in the azimuthal direction. We note that $\cos m\psi$ and $\sin m\psi$, when integrated over the interval 0 to 2π , are zero for all values of m except $m=0$. This yields $2\pi C_n^0$ as the only non-zero term. Our equation for thrust is now written as

$$T = \sum_n \rho V^2 2\pi C_n^0 Q_n^0(i0) \int_0^R P_n^0(v) r dr \quad (38)$$

(lower - upper)

The $Q_n^0(i0)$ terms can be pulled outside the integral because $n=0$ on the rotor disc. The $Q_n^m(in)$ are constants on the rotor disc, and their values are given in Appendix 7.2. Prior to the final integration of equation (38), the variable of integration rdr has to be expressed in terms of v in the ellipsoidal coordinate system. This change in variable is given in Appendix 7.1 by equation 7.1.7. Thus the thrust is written as

$$T = -\rho V^2 2\pi R^2 \sum_n C_n^0 Q_n^0(i0) \int_{-1}^{+1} P_n^0(v) v dv \quad (39)$$

Noting that $P_1^0(v) \equiv v$ and using the orthogonality relations given in Appendix 7.2, only the ($n=1$) term will have a non-vanishing integral, which yields for the final value of thrust

$$T = 4/3 \pi R^2 \rho V^2 C_1^0 \quad (40)$$

Equation (40) is solved for the constant C_1^0 in terms of standard thrust coefficient C_T and the definition of v employed by Peters in reference 63. (v = free stream velocity/ ΩR for this case.)

$$C_1^0 = 3/4 \frac{C_T}{v^2} \quad (41)$$

Thus, using the combination $m=0$ and $n=1$ will result in a steady thrust from the pressure field of equation (35). This thrust is manifested by the term $P_1^0(v)$ which vanishes as the edge of the rotor disc, thus causing the thrust to vanish at the edge of the disc. To better represent the lift distribution of an actual helicopter rotor, the lift should also vanish at the center of the disc (i.e., the rotor hub). This is readily accomplished by including other terms in the pressure distribution which will have no effect on the total lift as calculated by equation (39), but which will alter the radial thrust distribution. The Legendre Polynomials of the first kind (with $m=0$ and $n=\text{even integers}$) do not vanish at the edge of the rotor disc and consequently are not used, only the polynomials with n equal to an odd integer are used. This ensures that the hub thrust density is zero. If we include the term $m=0, n=3$ in the pressure distribution in order to ensure that the pressure distribution will be zero at the hub, equation (35) yields

$$C_0^1 P_1^0(0) Q_1^0(i0) + C_3^0 P_3^0(0) Q_3^0(i0) = 0 \quad (42)$$

Using the values for the Legendre Polynomials given in Appendix 7.2, the above equation yields the hub density correction factor C_3^0

$$C_3^0 = 3/2 C_1^0 \quad (43)$$

Combining equations (41) and (43) allows us to relate the hub density correction factor to the thrust coefficient C_T and the induced flow parameter v .

$$C_3^0 = 9/8 \frac{C_T}{v^2} \quad (44)$$

The effects of the hub correction factor on the rotor thrust distribution can be seen by examining the figures of Appendix 7.2 and 7.3. In Appendix 7.3 all the loading distributions investigated are described in more detail and displayed pictorially.

Using the above procedure, we can evaluate the constant D_2^1 by employing the equation for the rolling moment of the rotor disc

$$L = -T r \sin \psi. \quad (45)$$

Expressing the thrust by equation (37) allows us to rewrite the equation for the rolling moment as

$$L = -\rho V^2 \sum_{\substack{m,n \\ m < n}} Q_n^m(i0) \int_0^R \int_0^{2\pi} P_n^m(v) (C_n^m \cos m\psi + D_n^m \sin m\psi) (-r \sin \psi) r dr d\psi \quad (46)$$

The harmonic functions in equation (46), $\sin \psi \cos m\psi$ and $\sin \psi \sin m\psi$, integrated over the interval 0 to 2π , will be zero for all values of m except $m=1$ which yields the value πD_n^1 . Changing the variable of integration of equation (46) from $r^2 dr$ to the value given by equation (7.1.7) of Appendix 7.1 allows us to write the equation for the rolling moment as

$$L = -\rho V^2 \pi R^3 \sum_n D_n^1 Q_n^1(i0) \int_{-1}^1 P_n^1(v) v \sqrt{1-v^2} dv \quad (47)$$

Using the orthogonal relationship for Legendre Polynomials of the first kind will make equation (47) zero for all values of n except for $n=1$. When $n=1$ the rolling moment equation can be written as

$$L = 8/5 i \pi R^3 \rho V^2 D_2^1 \quad (48)$$

Using the definition of rolling moment coefficient, C_L , equation (48) can be solved for the constant D_2^1 .

$$D_2^1 = -5/8 i \frac{C_L}{v^2} \quad (49)$$

Correspondingly, the pitching moment equation can be written as

$$M = - T r \cos \psi \quad (50)$$

Which, when combined with the thrust given by equation (37) yields

$$M = -\rho V^2 \sum_{\substack{m,n \\ m < n}} Q_n^m(i0) \int_0^R \int_0^{2\pi} P_n^m(v) (C_n^m \cos m\psi + D_n^m \sin m\psi) (-r \cos \psi) r dr d\psi \quad (51)$$

Analogous to the rolling moment equation, the harmonic functions in equation (51) will be zero over the integration interval for all values of m except $m=1$ which yields πC_n^1 . Changing the variable of integration from dr to dv allows us to write the equation for the pitching moment as

$$M = -\rho V^2 \pi R^3 \sum_n C_n^1 Q_n^1(i0) \int_{-1}^{+1} P_n^1(v) v \sqrt{1-v^2} dv \quad (52)$$

Using the same technique employed on equation (47) the resulting pitching moment is

$$M = 8/5 i \pi R^3 \rho V^2 C_2^1 \quad (53)$$

We then solve for the constant C_2^1

$$C_2^1 = -5/8 i \frac{C_M}{v^2} \quad (54)$$

Up to this point, the evaluation of the constants C_1^0 , C_3^0 , C_2^1 and D_2^1 have followed the theory of Mangler and Squire.

The constants C_1^0 , C_2^1 , and D_2^1 respectively represent the total thrust, pitching moment, and rolling moment experienced by a helicopter rotor under the pressure distribution of equation (8). The constant C_3^0 , hub thrust correction factor, ensures that the thrust is zero at the hub.

The determination of the constants C_4^1 , D_4^1 , C_3^2 and D_3^2 for this research program will be different from the theory employed by Joglekar-Loewy in which they were taken as zero. The constants C_4^1 and D_4^1 will be utilized to enforce the physical boundary condition that the pitching and rolling moment slopes at the hub are zero. This technique allows a logical selection of the constants as well as a direct measure of the effect on induced flow distribution.

The hub moment correction factors, C_4^1 and D_4^1 , are determined by enforcing the boundary condition that the slope of the pitching and rolling forces are zero at the hub. This boundary condition is mathematically expressed as

$$\left. \frac{d\phi}{dr} \right|_{\eta=0} = - \frac{\sqrt{1-v^2}}{v} \left. \frac{d\phi}{dv} \right|_{\eta=0} = 0 \quad (55)$$

Using equation (55) and considering only those terms of the pressure distribution, equation (35), which contribute to the pitching moment, yield zero values except for the following terms

$$C_2^1 Q_2^1 (in) \left(-\frac{\sqrt{1-v^2}}{v} \right) \frac{dP_2^1(v)}{dv} \Big|_{\substack{v=1 \\ \eta=0}} + C_4^1 Q_4^1 (in) \left(-\frac{\sqrt{1-v^2}}{v} \right) \frac{dP_4^1(v)}{dv} \Big|_{\substack{v=1 \\ \eta=0}} = 0 \quad (56)$$

Solving equation (56) for the unknown constant C_4^1 we obtain

$$C_4^1 = 9/40 C_2^1 \quad (57)$$

Using the value for C_2^1 given by equation (54) allows us to express C_4^1 in terms of the pitching moment coefficient and induced velocity flow parameter v

$$C_4^1 = -9/64 i \frac{C_M}{v^2} \quad (58)$$

The rolling moment hub correction factor D_4^1 is determined using equations (35) and (55) with their rolling moment terms in the above procedure. For purposes of brevity only the result will be shown. Thus, the rolling moment hub correction factor is

$$D_4^1 = -9/64 i \frac{C_L}{v^2} \quad (59)$$

This leaves two constants for the pressure distribution of equation (35), C_3^2 and D_3^2 , which have not yet been determined. These constants will be used to represent a second harmonic of the pressure distribution. The two-per-rev load is defined as

$$L_2 = -T r^2 \sin 2\psi \quad (60)$$

When the value of the thrust given by equation (37) is substituted into equation (60) the two-per-rev rolling moment can be written as

$$L_2 = -\rho V^2 \sum_{\substack{m,n \\ m < n}} Q_n^m(i0) \int_0^R \int_0^{2\pi} P_n^m(v) (C_n^m \cos m\psi + D_n^m \sin m\psi) (-r^2 \sin 2\psi) r dr d\psi \quad (61)$$

The harmonic functions of equation (61) will be zero over the integration interval of 0 to 2π for all values of m , except when $m=2$. For this case the term $D_n^2 \sin^2 2\psi$ when integrated over the interval becomes πD_n^2 . Changing the variable of integration from $r^3 dr$ to the value given by equation (7.1.7) of Appendix 7.1 allows us to write the equation for the 2/rev load as

$$L_2 = -\rho V^2 R^4 \pi \sum_n Q_n^2(i0) D_n^2 \int_{-1}^1 P_n^2(v) (1-v^2) v dv \quad (62)$$

The orthogonal relationship of the Legendre Polynomials results in $n=3$ being the only non-zero term. When $n=3$ the 2p rolling moment is

$$L_2 = 128/7 \rho V^2 \pi R^4 D_3^2 \quad (63)$$

The definition for a 2-per-revolution pressure coefficient, C_{2L} , and the inflow parameter, v , can be used to yield the constant D_3^2 .

$$D_3^2 = 7/128 \frac{C_{2L}}{v^2} \quad (64)$$

Repeating the above procedure, the constant C_3^2 can be determined in terms of the second harmonic pitching moment, C_{2M} , and the inflow parameter, v .

$$C_3^2 = 7/128 \frac{C_{2M}}{v^2} \quad (65)$$

All the constants pertaining to the pressure distribution given by equation (35) have now been defined. Up to this point, we have only discussed the rotor pressure distribution itself. We will now discuss how the pressure distribution is used to solve for the induced velocities of the rotor.

Mangler, in reference 42, utilizes the fact that the pressure distribution, equation (8), is a solution of the Laplace equation. Consequently, the nondimensional induced velocity caused by the prescribed nondimensional pressure distribution can be determined from the following equation

$$\bar{Q}_i(X,Y,Z) = v \int_{-\infty}^X \phi_{,i}(\xi,Y,Z) d\xi \quad i = X,Y,Z \quad (66)$$

The above equation yields the induced velocity components at the field point (X,Y,Z) . It should be noted that equation (66) determines the components of the induced velocity of the rotor disc along the X , Y , and Z axis of the wind coordinate system.

The dynamic inflow theories were developed and structured around the premise that the dynamic inflow components normal to the disc are of primary interest. In view of this, the conversion of the Mangler actuator theory to a dynamic inflow theory requires the determination of the induced velocity normal to the disc. This implies that we need only determine the induced velocity in the Z' direction of the disc coordinates, which is readily accomplished by rewriting equation (66) as

$$\bar{W}(X',Y',0) = -v \int_0^{\infty} \phi_{,Z'}(\bar{X}',\bar{Y}',\bar{Z}') d\xi \quad (67)$$

where $\bar{X}' = X' + \xi \cos \alpha$, $\bar{Y}' = Y'$, $\bar{Z}' = -\xi \sin \alpha$, and where $\phi_{,Z'}$ is the partial derivative of the pressure field with respect to the Z' axis of the disc coordinate system. The variable ξ in equation (67) is a dummy variable of integration in the X direction. Thus, the integration is performed from the disc to the infinite field along the streamline parallel to the X axis in the wind system. Figure 7.1.3 of Appendix 7.1 depicts the integration

technique. To find ϕ, z' , we have to employ the chain rule because the pressure distribution of equation (8) is given in terms of the ellipsoidal coordinate system.

$$\phi, z' = \frac{\partial \phi}{\partial z'} = \frac{\partial \zeta^i}{\partial z'} \cdot \frac{\partial \phi}{\partial \zeta^i} \quad i = \sum 1, 2, 3 \quad (68)$$

where ζ^i represents the ellipsoidal coordinate system.

In expanded form equation (68) can be written as

$$\frac{\partial \phi}{\partial z'} = \frac{\partial v}{\partial z'} \cdot \frac{\partial \phi}{\partial v} + \frac{\partial \eta}{\partial z'} \cdot \frac{\partial \phi}{\partial \eta} + \frac{\partial \psi}{\partial z'} \cdot \frac{\partial \phi}{\partial \psi} \quad (69)$$

The terms $\frac{\partial v}{\partial z'}$, $\frac{\partial \eta}{\partial z'}$, and $\frac{\partial \psi}{\partial z'}$ are determined by taking the the derivative of the ellipsoidal coordinate transformations listed in Appendix 7.1. The term $\frac{\partial \psi}{\partial z'}$ is zero, and thus need not be considered.

$$\frac{\partial v}{\partial z'} = \frac{-\eta(1-v^2)}{v^2 + \eta^2} \quad (70 \text{ a-b})$$

$$\frac{\partial \eta}{\partial z'} = \frac{-v(1+\eta^2)}{v^2 + \eta^2}$$

The terms $\frac{\partial \phi}{\partial v}$ and $\frac{\partial \phi}{\partial \eta}$ are obtained by taking the partial derivative of the pressure distribution that we are utilizing for this research, equation (35). These terms can be determined by taking the derivative term by term or using the recursive formula for the derivatives given in Appendix 7.2. The induced velocity normal to disc (i.e., in the z'

direction) is

$$\bar{w}(X', Y', Z') = -v \int_0^\infty \left[\frac{-\eta(1-v^2)}{v^2+\eta^2} \cdot \frac{\partial \phi}{\partial v} + \frac{-v(1+\eta^2)}{v^2+\eta^2} \cdot \frac{\partial \phi}{\partial \eta} \right] d\eta \quad (71)$$

where v and η are functions of ξ . This equation is extremely complex and is evaluated by a computer program that is described in the next section.

A specialization of equation (71) can be made for the condition of $\alpha = 90^\circ$ (axial flow). For such a condition Z and ξ are parallel; and equation (71) reduces to

$$\bar{w}(X', Y', Z') = -v \phi \Big|_{\eta=0} \quad (72)$$

Thus, the induced flow may be found directly from the non-dimensional pressure distribution ϕ with no integration for the axial flow case. Another specialization of equation (71) is the case of edgewise flow, $\alpha = 0^\circ$. Here, ξ is parallel to the X axis, and a portion of the integration is on the disc.

$$\bar{w}(X', Y', Z') = -v \int_{-\infty}^{\sqrt{1-y^2}} \frac{1}{\eta} \frac{\partial \phi}{\partial v} \Big|_{v=0} dx \quad (73)$$

$$-v \int_{\sqrt{1-y^2}}^x \frac{1}{v} \frac{\partial \phi}{\partial \eta} \Big|_{\eta=0} dx$$

Equations (72) and (73) yield the induced velocities for

$\alpha = 90^\circ$ and $\alpha = 0^\circ$ and are used as a check on the induced velocity calculated by the computer program.

The induced flow perturbation equation that is used in the actuator disc research is

$$v = v_o + v_s \bar{r} \sin \psi + v_c \bar{r} \cos \psi + v_{2s} \bar{r}^2 \sin 2\psi + v_{2c} \bar{r}^2 \cos 2\psi \quad (74)$$

The induced flow perturbations will be obtained by integrating the induced velocity \bar{w} over the disc area. For our purposes the induced low perturbations are defined as

$$\begin{aligned} v_o &= \frac{1}{\pi} \int_0^{2\pi} \int_0^1 \bar{w} \bar{r} \, d\bar{r} \, d\psi \\ v_s &= \frac{4}{\pi} \int_0^{2\pi} \int_0^1 \bar{w} \bar{r}^2 \sin \psi \, d\bar{r} \, d\psi \\ v_c &= \frac{4}{\pi} \int_0^{2\pi} \int_0^1 \bar{w} \bar{r}^2 \cos \psi \, d\bar{r} \, d\psi \\ v_{2s} &= \frac{6}{\pi} \int_0^{2\pi} \int_0^1 \bar{w} \bar{r}^3 \sin 2\psi \, d\bar{r} \, d\psi \\ v_{2c} &= \frac{6}{\pi} \int_0^{2\pi} \int_0^1 \bar{w} \bar{r}^3 \cos 2\psi \, d\bar{r} \, d\psi \end{aligned} \quad (75 \text{ a-e})$$

Due to the symmetries of the problem, only one half of the induced velocity field need be calculated for a given coefficient. For example, for all of the C coefficients

$$(c_1^0, c_3^0, c_2^1, c_4^1, c_3^2)$$

$$v_o = \frac{2}{\pi} \int_0^\pi \int_0^1 \bar{w} \bar{r} \, d\bar{r} \, d\psi, \quad v_s = v_{2s} = 0$$

$$v_c = \frac{8}{\pi} \int_0^\pi \int_0^1 \bar{w} \bar{r}^2 \cos\psi \, d\bar{r} \, d\psi$$

$$v_{2c} = \frac{12}{\pi} \int_0^\pi \int_0^1 \bar{w} \bar{r}^3 \cos\psi \, d\bar{r} \, d\psi \quad (75 \text{ a,c,e})$$

For all the D coefficients (D_2^1, D_4^1, D_3^2)

$$v_o = v_c = v_{2c} = 0, \quad v_s = \frac{8}{\pi} \int_0^\pi \int_0^1 \bar{w} \bar{r}^2 \sin\psi \, d\bar{r} \, d\psi$$

$$v_{2s} = \frac{12}{\pi} \int_0^\pi \int_0^1 \bar{w} \bar{r}^3 \sin 2\psi \, d\bar{r} \, d\psi \quad (75 \text{ b,d})$$

These flows, calculated for each coefficient, can be formed into an \bar{L} matrix

$$\begin{bmatrix} v_o \\ v_s \\ v_c \\ v_{2s} \\ v_{2c} \end{bmatrix} = v \begin{bmatrix} \bar{L} \end{bmatrix} \begin{bmatrix} C_1^o \\ C_3^o \\ iD_2^1 \\ iD_4^1 \\ iC_2^1 \\ iC_4^1 \\ D_3^2 \\ C_3^2 \end{bmatrix} = v \begin{bmatrix} \bar{L} \end{bmatrix} \{CD\} \quad (76)$$

Other definitions of v 's are also possible. The above are chosen, however, on the basis of ease of implementation, mathematical consistency, and physical significance.

The $\{CD\}$ coefficients can be related to the lift distribution by the formulas previously obtained.

$$\begin{bmatrix} C_1^o \\ C_3^o \\ iD_2^1 \\ iD_4^1 \\ iC_2^1 \\ iC_4^1 \\ D_3^2 \\ C_3^2 \end{bmatrix} = \frac{1}{v^2} \begin{bmatrix} 3/4 & 0 & 0 & 0 & 0 \\ 9/8 & 0 & 0 & 0 & 0 \\ 0 & 5/8 & 0 & 0 & 0 \\ 0 & 9/64 & 0 & 0 & 0 \\ 0 & 0 & 5/8 & 0 & 0 \\ 0 & 0 & 9/64 & 0 & 0 \\ 0 & 0 & 0 & -7/128 & 0 \\ 0 & 0 & 0 & 0 & -7/128 \end{bmatrix} \begin{bmatrix} C_T \\ C_L \\ C_M \\ C_{2L} \\ C_{2M} \end{bmatrix} \quad (77)$$

$$\text{or } \{CD\} = \frac{1}{v^2} [T] \{F\}$$

The $[L]$ matrix, including the hub correction factors (C_3^0, D_4^1, C_4^1) is obtained by combining equations (76) and (77).

$$[L] = \frac{1}{V} [\bar{L}] [T] \quad (78)$$

The $[L_5]$ matrix without correction factors (i.e., for a different radial distribution) is obtained by setting the C_3^0, D_4^1, C_4^1 rows of $[T]$ to zero. The first three rows and columns of $[L_5]$ correspond to the classical $[L_3]$ matrix. Comparing $[L_3]^{-1}$ with the first three rows and columns of $[L_5]^{-1}$ will provide a measure of the effect of azimuthal lift distribution on induced flow.

3.1.2 Unsteady Aerodynamics

Part of the research was concerned with extending the steady actuator-disc theory of Mangler to the unsteady case. This represents a significant modification to the steady inflow theory, and will be developed in detail in this section. The general momentum equation for incompressible fluid flow is

$$\frac{\delta q_i}{\delta t} + q_j q_{i,j} = -\frac{1}{\rho} p_{,i} \quad i, j = 1, 2, 3 \quad (79)$$

where the terminology $q_{i,j}$ means the partial derivative of q_i with respect to j . The continuity equation can be written as

$$q_{i,i} = 0 \quad i = 1, 2, 3 \quad (80)$$

Equation (79) can be rewritten for the particular geometry of the actuator disc problem in conjunction with linearization. This equation, as originally given by Mangler can be written as

$$\frac{\partial q_i}{\partial t} - V_{FS} q_{i,x} = - \frac{1}{\rho} p_{,i} \quad (81)$$

The above momentum equation can be nondimensionalized with respect to time by making use of the following definitions and equations.

$$\begin{aligned} \psi &= rt \\ (*) &= \frac{d}{d\psi} \\ v &= \frac{V_{FS}}{\Omega R} \\ \hat{\phi} &= \frac{P}{\rho \Omega^2 R^2} \\ \bar{q} &= \frac{q}{\Omega R} \\ x &= X/R \end{aligned} \quad (82 \text{ a-f})$$

The nondimensional linearized momentum equation is

$$\frac{\partial \bar{q}_i}{\partial \psi} - v q_{i,x} = -\hat{\phi}_{,i} \quad (83)$$

The above equation will be solved by two different methods. In the first method, we assume that the pressure field can be expressed as mutually in-phase simple harmonic motion. This will be referred to as "superposition of velocities". In the

second method, we assume that the inflow distribution varies as a simple harmonic function. This will be referred to as "superposition of pressures".

In the superposition of velocities method, all the components of pressure are assumed to be in-phase.

$$\hat{\phi} = \bar{\phi} e^{j\omega\psi} \quad (84)$$

where the term $\bar{\phi}$ is assumed to be a real function. Equation (84) will be used in conjunction with equation (83) to calculate the induced velocities that result from the pressure fluctuations. The velocity field is represented by the complex expression

$$q = \bar{q} e^{j\omega\psi}$$

$$\text{where } \bar{q} = w + ju \quad (85)$$

This is a superposition of the complex velocity field. Substituting equations (84) and (85) into equation (83) and performing the indicated operations results in the following equations

$$(w_i \omega j - u_i \omega) e^{j\omega\psi} - v[w_{i,x} + ju_{i,x}] e^{j\omega\psi} = - \bar{\phi}_i e^{j\omega\psi} \quad (86)$$

Dividing both sides of equation (86) by $e^{j\omega\psi}$ and segregating the real and imaginary components allows us to write the following two equations

$$\begin{array}{ll} \text{REAL COMPONENTS} & \omega u_i + v w_{i,x} = \bar{\phi}_{,i} \\ \text{IMAGINARY COMPONENTS} & \omega w_i - v u_{i,x} = 0 \end{array} \quad (87 \text{ a-b})$$

We let the derivatives with respect to the X axis, or wind axis, be noted by a prime ($q_{,i} = q'$) and solve equation (87b).

$$\begin{array}{ll} w_i = \frac{v}{\omega} u'_i \\ u'_i = \frac{\omega}{v} w_i \end{array} \quad (88 \text{ a-b})$$

Substituting equations (88 a-b) into equation (87a) yields two equations

$$\begin{array}{ll} \omega^2 u_i + v^2 u'_{i'} = \omega \bar{\phi}_{,i} \\ \omega^2 w_i + v^2 w'_{i'} = v \bar{\phi}'_{,i} \end{array} \quad (89 \text{ a-b})$$

Taking the derivative of equations (89 a-b) with respect to i and employing the continuity equation, (80), yields

$$\begin{array}{ll} \bar{\phi}_{,ii} = 0 \\ \text{i.e. } \nabla^2 \bar{\phi} = 0 \end{array} \quad (90)$$

Thus, we note that, for the complex frequency response problem, the pressure distribution in equation (84) must satisfy the Laplace equation, i.e. (90). This is very significant in that it allows the use of Mangler's static pressure distribution for the unsteady theory, since equations (8) and

(35) are solutions to the Laplace equation. It is also assumed that the induced velocity is zero at a large distance from the rotor disc, that is to say $w_i(\infty) = u_i(\infty) = 0$.

A special case of equation (87) exists when the actuator-disc is in still air. This means $v=0$ and equation 87a reduces to

$$u_i = \frac{1}{\omega} \bar{\phi}_{,i} \quad (91)$$

Thus, the complex or out-of-phase axial induced velocity for this case can be determined by taking the derivatives of the pressure field. No integration is required.

$$\bar{u} = \frac{1}{\omega} \bar{\phi}_{,z} \quad (92)$$

Evaluating equation (92) on the rotor disc yields

$$\bar{u} = - \frac{1}{\omega} \frac{1}{v} \frac{\partial \bar{\phi}}{\partial \eta} \bigg|_{\eta=0} \quad (93)$$

This special case is extremely useful for checking the unsteady calculations of the computer program. Equations (89a-b) will be solved by taking the Laplace transform of the equations. Thus, the equations can be written in the Laplace domain as

$$u_i(s) = \frac{1}{v} \cdot \frac{\omega/v}{s^2 + \omega^2/v^2} \cdot \bar{\phi}_{,i}(s) \quad (94 \text{ a-b})$$

$$w_i(s) = \frac{1}{v} \cdot \frac{s}{s^2 + \omega^2/v^2} \cdot \bar{\phi}_{,i}(s)$$

Taking the inverse Laplace transform of equations (96 a-b) will yield the real and imaginary part of the induced velocity, u_i and w_i respectively. Before performing the inverse Laplace transform we note that the inverse Laplace transform of $\bar{\phi}(s)$ will yield the Mangler pressure distribution, $\phi_{,i}$. We also make use of the Laplace transform of the sine and cosine functions, which are

$$\begin{aligned} \sin \frac{\omega}{v} t &= \mathcal{L}^{-1} \left\{ \frac{\omega/v}{s^2 + \omega^2/v^2} \right\} \\ \cos \frac{\omega}{v} t &= \mathcal{L}^{-1} \left\{ \frac{s}{s^2 + \omega^2/v^2} \right\} \end{aligned} \quad (95 \text{ a-b})$$

Employing the convolution integral, we can readily determine the induced velocity components as

$$\begin{aligned} w_i(x', y', z') &= \frac{1}{v} \int_{-\infty}^{x'} \bar{\phi}_{,i}(\xi) \cos \left[\left(\frac{\omega}{v} \right) (x' - \xi) \right] d\xi \\ u_i(x', y', z') &= - \frac{1}{v} \int_{-\infty}^{x'} \phi_{,i}(\xi) \sin \left[\left(\frac{\omega}{v} \right) (x' - \xi) \right] d\xi \end{aligned} \quad (96 \text{ a-b})$$

where ξ is defined along the x axis with $\xi=0$ at the plane of the rotor disc.

We define a reduced frequency K based on air speed, not tip speed, as ω/v . This allows us to write the normal

velocity components at the disc as

$$\begin{aligned} w_{z'} &= \frac{1}{v} \int_{-\infty}^0 \bar{\phi}_{,z'} \cos(K\xi) d\xi && \text{(in-phase)} \\ u_{z'} &= -\frac{1}{v} \int_{-\infty}^0 \bar{\phi}_{,z'} \sin(K\xi) d\xi && \text{(out-of-phase)} \end{aligned} \quad (97 \text{ a-b})$$

Several interesting aspects of these equations should be pointed out. First, these are identical to the integrals in the steady aerodynamic theory, equation (67), except for the weighting functions that have been added. Second, these weighting functions, $\cos(K\xi)$ and $\sin(K\xi)$, have direct physical interpretation. They can be associated with an oscillatory pressure field that varies as a wave traveling at velocity v and frequency ω . Third, for $\omega=0$, the above formulas reduce to equation (67). Fourth, the effect of unsteadiness is only a function of K . Thus, for a given rotor angle-of-attack, a single sweep of K will suffice to give the behavior for all ω, v combinations. Lastly, the similarity of equations for the steady and unsteady induced velocities allows the utilization of the same numerical integration technique.

The second assumption used with equation (83) is called the superposition of pressures. In this method it is assumed that the inflow distribution varies harmonically but is in-phase. Thus, the induced velocities are expressed as

$$q_i = \bar{q}_i e^{j\omega\psi} \quad (98)$$

where \bar{q} is assumed to be a real number. The pressure distribution will be represented by the following complex expression

$$P_o = (A_o + B_o j) e^{j\omega\psi} \quad (99)$$

hence the name superposition of pressures. Substituting equations (98) and (99) into the momentum equation, (83), and performing the indicated operations yields

$$j\omega\bar{q}_i e^{j\omega\psi} - v\bar{q}_{i,x} e^{j\omega\psi} = - (A_{o,i} + B_{o,i} j) e^{j\omega\psi} \quad (100)$$

Dividing both sides of equation (100) by $e^{j\omega\psi}$ and segregating the real and imaginary components allows us to write the following two equations.

$$\text{REAL COMPONENTS} \quad v\bar{q}_{i,x} = A_{o,i} \quad (101a-b)$$

$$\text{IMAGINARY COMPONENTS} \quad \omega\bar{q}_i = - B_{o,i}$$

Taking the derivative of equations (101a-b) with respect to i and employing the continuity equation (80) yields

$$\nabla^2 B_o = 0 \quad (102a-b)$$

$$\nabla^2 A_o = 0$$

Thus, both pressure functions (A_o and B_o) can be represented by the Mangler-Squire series seen earlier. (They both solve the same equations and boundary conditions.) It follows directly, under the assumption of in-phase velocities, that

the relationship between these velocities and the in-phase pressure (A_0) is identical to the existing Mangler-Squire theory, equation (101a). The out-of-phase pressure distribution (B_0) is then given by equation (101b) which states that the velocity simply equals $-1/\omega$ times the pressure (with no integration from $0 \rightarrow \infty$ as previously required). The implications of equation (102) are very important. It implies that the pressure from q and \dot{q} (i.e., A_0 and B_0) can be superimposed. This has been an underlying assumption in all dynamic inflow work to date. Furthermore, since $\bar{q}_i = -1/\omega B_{0,i}$, the velocity field is independent of either the magnitude or direction of the free-stream velocity (another assumption of previous work in dynamic inflow).

It is reasonable to consider the correlation between the two above theories (pressure in-phase, velocity in-phase) and the true solution. One would expect the actual case to have neither in-phase pressure nor velocity. Thus, a comparison of results under the two assumptions can be used to obtain reasonable bounds on the effect of unsteadiness.

In the superposition of velocities method, we assume that the pressure field is in-phase with itself. The general form of the equation can be written as

$$\{v\} = [L]\{F\} + [Q]\{\dot{F}\} \quad (103)$$

Where the column matrix $\{v\}$ is the induced velocity perturbations v_o, v_s, v_c . The generalized rotor response vector $\{F\}$ consists C_T, C_L, C_M , while $\{\dot{F}\}$ contains the unsteady terms. The $[L]$ matrix will contain the real part of the induced inflow, while the $[Q]$ matrix will contain the imaginary part of the induced inflow determined by method one. Using our assumed pressure distribution we can solve equation (103) for $\{F\}$.

$$\{F\} = [[L] + [Q]i\omega]^{-1} \{v\} \quad (104)$$

We define a complex $[L]$ matrix as $[L(K)]$. Equation (104) can then be written as

$$\{F\} = [L(K)]^{-1} \{v\} \quad (105)$$

In the superposition of pressure method we assume that the induced velocities are in-phase and we determine the resulting complex pressure distribution. The general form of the equation is

$$[M]\{\dot{v}\} + [L]^{-1} \{v\} = \{F\} \quad (106)$$

Substituting the assumed induced velocity $\{v\} = \{\bar{v}\}e^{j\omega\psi}$ in equation (106) allows us to rewrite the equation as

$$[[L]^{-1} + [M]i\omega] \{\bar{v}\} = \{F\} \quad (107)$$

Thus, the unsteady aerodynamic research is concerned with the equivalence of equations (105) and (107) i.e.

$$\begin{aligned}
 & [[L] + [Q]i\omega]^{-1} \stackrel{?}{=} [L]^{-1} + [M]i\omega \\
 & [L] + [Q]i\omega \stackrel{?}{=} [[L]^{-1} + [M]i\omega]^{-1}
 \end{aligned}
 \tag{108 a-b}$$

where $[L(K)] = [L] + [Q]i\omega$

3.2 PRESCRIBED-WAKE VORTEX THEORY

The United Technologies Research Center's Prescribed Wake program was used to investigate the effects of a finite number of blades and wake geometry on the dynamic inflow $[L]$ matrix. This program was developed by Landgrebe (68) and is based on the lifting line analysis of Piziali (23,24). The program originally was developed to calculate the induced velocity distribution of a rotor, for a given wake geometry. The program is capable of generating a classical wake which is based on the momentum induced velocity, or a wake geometry can be inputted from prescribed wake data. The program has a capability of modeling the tip vortex roll up by combining a designated number of vortices after a specified number of azimuth positions.

The program had to be modified to calculate the aerodynamic loading coefficients, $\{F\}$, as previously defined in the dynamic inflow section. The formulas for the aerodynamic loading coefficients are given below. In the formulas, l' is the lift per blade radial station, b is the number of rotor blades, and N is the number of rotor azimuth

positions used in the calculations.

$$C_T = \frac{b \sum_{i=1}^N \int_0^1 \ell'(i) dr}{N \rho \pi \Omega^2 R^4} \quad (109 \text{ a-c})$$

$$C_L = \frac{b \sum_{i=1}^N \int_0^1 \ell'(i) r \sin \psi dr}{N \rho \pi \Omega^2 R^5}$$

$$C_M = \frac{b \sum_{i=1}^N \int_0^1 \ell'(i) r \cos \psi dr}{N \rho \pi \Omega^2 R^5}$$

The induced flow perturbations v_o , v_s and v_c are obtained by integrating the axial induced velocity over the disc. The integration of equation (75 a-c) had to be included in the program.

To uniquely determine the 3x3 [L] matrix, which has 9 unknowns, requires three perturbations of the rotor inputs, $(\theta_o, \theta_s, \theta_c)$ from the trim condition. Thus, upon trimming the rotor for a given flight condition equations (75) and (109) are used to obtain

$$\begin{bmatrix} v_o \\ v_s \\ v_c \end{bmatrix}_{\text{TRIM}} = \{v\}_{\text{TRIM}} \quad (110)$$

$$\begin{bmatrix} C_T \\ C_L \\ C_M \end{bmatrix}_{\text{TRIM}} = \{F\}_{\text{TRIM}}$$

The rotor inputs are in turn perturbed for three separate cases, which yields three distinct $\{v\}$ and $\{F\}$ matrices.

$$\begin{matrix} \{v\}_i & i=1,3 \\ \{F\}_i \end{matrix} \quad (112)$$

However, we are interested in the $\{v\}$ and $\{F\}$ as a result of the input perturbations, so we define a $\{\bar{v}\}$ and $\{\bar{F}\}$ which result from the perturbations

$$\{\bar{v}\}_i = \{v\}_i - \{v\}_{\text{TRIM}} \quad (113)$$

$$\{\bar{F}\}_i = \{F\}_i = \{F\}_{\text{TRIM}}$$

We can now write the $[L]$ matrix as

$$\begin{bmatrix} \bar{v}_o(1) & \bar{v}_o(2) & \bar{v}_o(3) \\ \bar{v}_s(1) & \bar{v}_s(2) & \bar{v}_s(3) \\ \bar{v}_c(1) & \bar{v}_c(2) & \bar{v}_c(3) \end{bmatrix} = \frac{1}{v} \begin{bmatrix} L(1,1) & L(1,2) & L(1,3) \\ L(2,1) & L(2,2) & L(2,3) \\ L(3,1) & L(3,2) & L(3,3) \end{bmatrix} \begin{bmatrix} \bar{c}_T(1) & \bar{c}_T(2) & \bar{c}_T(3) \\ \bar{c}_L(1) & \bar{c}_L(2) & \bar{c}_L(3) \\ \bar{c}_M(1) & \bar{c}_M(2) & \bar{c}_M(3) \end{bmatrix} \quad (114)$$

$$\text{or } [\bar{v}] = \frac{1}{v} [L] [\bar{F}]$$

Upon inverting $[\bar{F}]$ and post-multiplying by it, we obtain the $[L]$ matrix we desire.

$$[L] = v [\bar{v}] [\bar{F}]^{-1} \quad (115)$$

It should be noted, that for the above solution technique of the $[L]$ matrix, the $[\bar{F}]$ matrix must be non-singular. Thus independent loading conditions must be prescribed.

4. DEVELOPMENT OF COMPUTER MODELS

The computer programs utilized in this research will be discussed in this section. Two large Fortran computer programs were utilized in the bulk of the research. One of the programs was written and developed as a specific part of this research. This program was used in the actuator-disc calculations of the steady and unsteady [L] matrices. The second program was the UTRC prescribed wake computer program which was modified to calculate the steady dynamic inflow [L] matrix.

4.1 ACTUATOR-DISC PROGRAM

A Fortran computer program was written to numerically integrate equation (71) in order to obtain the induced velocities at the rotor disc. As this program is quite lengthy (over 1300 lines of code) it will only be discussed in a general manner. The basic calculation procedure and some developmental history is presented in the following paragraphs. The computer program was first developed to perform the calculations of the steady [L] matrix. This allowed a verification of the program logic and a development of a reliable steady [L] matrix before modification of the program to perform the unsteady calculations.

4.1.1 Steady Calculations

The actuator-disc computer program is designed to perform numerical integrations of five induced velocities

simultaneously. This allows the simultaneous calculation of induced velocities at a particular blade radial station and azimuth position for five loading conditions. This results in a considerable savings of computer time over five sequential calculations. The induced velocities are obtained at a particular azimuth position for all the radial blade stations from the hub to the tip, after which the azimuth position is incremented and the process repeated. The direction of integration is the reverse of that shown in equation (71). That is to say, the program is designed to integrate from the disc to infinity. This process allows the program to stop when the integrand becomes relatively small.

The first step in the integration of equation (71) is the transformation of the disc coordinates into ellipsoidal coordinates. Simpson's 1/3 rule is used to integrate along the streamline parallel to the X axis. At each point of integration, a coordinate transformation is required, the polynomials $P_n^m(v)$ and $Q_n^m(in)$ are evaluated, and the derivatives of the polynomials P_n^m and Q_n^m are evaluated using the recursive formulas of Appendix 7.2. Generally, the program integrates to a final eta of 15 to 20 before the integral converges. The $P_n^m(v)$ and $Q_n^m(in)$ polynomials are calculated using double precision because, for $n \geq 10$, the $Q_n^m(in)$ oscillate about a zero-mean (rather than decaying)

AD-A099 532

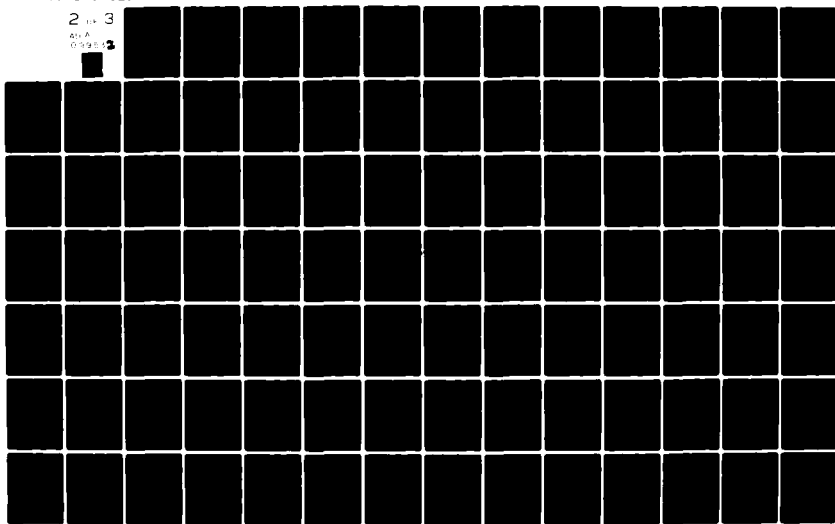
ARMY TROOP SUPPORT AND AVIATION MATERIEL READINESS CO--ETC F/8 20/4
ROTOR DYNAMIC INFLOW DERIVATIVES AND TIME CONSTANTS FROM VARIOU--ETC(U)
DEC 80 D M PITT
TSARCOM-TR-81-2

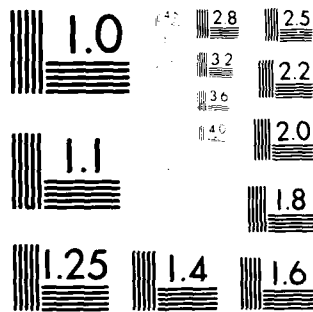
UNCLASSIFIED

NL

2 1 3

01A
019 1 2





MICROCOPY RESOLUTION TEST CHART
NATIONAL BUREAU OF STANDARDS-1963-A

when only single-precision is used. This is because the $Q_n^m(in)$ contain the differences between two relatively large numbers, which results in high round-off errors.

After a complete azimuth sweep, the induced velocities are stored in a 3-dimensional array of size (A,B,5) where A is the number of azimuth positions, B is the number of blade radial stations, and the numbers 1 through 5 represent the C_T , C_L , C_M , C_{2L} and C_{2M} loading conditions respectively. Due to the symmetry and antisymmetry properties of the polynomials, the induced velocities are only calculated for $0 \leq \psi \leq 180$. The induced velocities are then integrated in the radial and azimuthal direction for each separate loading condition in accordance with equations (75,76,77, and 78) to obtain the 5x5 and 3x3 [L] matrix. Gauss Quadrature integration is performed in the radial direction and Simpson's 1/3 rule is used to perform the azimuthal integrations.

As mentioned in the previous section, for the special case of steady, axial flow, the induced velocity on the rotor disc is given by equation (72). For this case, the induced velocity on the disc is the negative of the pressure distribution. This yields an exact induced-velocity distribution that is used for comparison with the induced-velocity calculated by the integration of equation (71). Figure 7 depicts the results of varying the integration increment along the streamline. This figure also depicts the Gauss-point locations for 10 blade radial stations. It is obvious

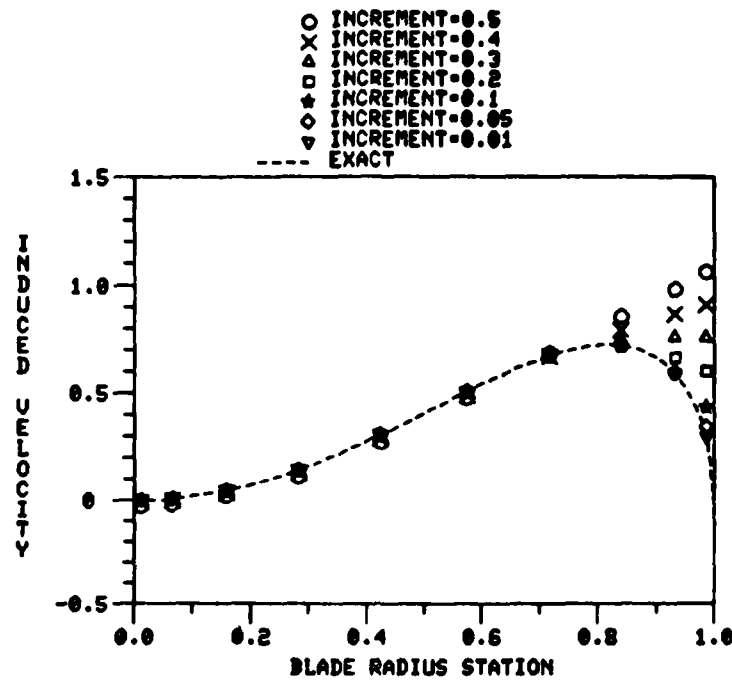


Figure 7. Effects of Streamline Integration Increments on the Induced Velocity Distribution. Corrected Thrust Distribution and $\alpha = 90^\circ$.

from this figure that the numerical integration becomes more difficult for blade stations with $r \geq .7$. To calculate the induced velocity close to the tip requires very small integration increments, while the increments can be considerably larger in the inboard blade area. To take advantage of this fact, the computer program uses a nominal integration increment of .05 for $r \leq .7$ and an increment of .01 for $r > .7$. This results in a savings of computer time, without sacrificing accuracy of the induced velocity calculations.

We now wish to discuss the numerical accuracy of this program. Equation (72), when substituted into equation (75), yields the exact value of the $[L]$ matrix for the case of $\alpha = 90^\circ$. This equation can be integrated in closed form to yield the $L(1,1)$ element as 0.5. Thus, numerical experiments were conducted with the exact induced velocity being used to calculate the $L(1,1)$ term. Figure 8 shows the results of the various integration techniques used to integrate the resultant induced velocity in the radial direction. (Note that, for the case $\alpha = 90^\circ$, the induced velocity attributable to C_T is only a function of the radial position.) Rectangular integration required the calculation of the induced velocities at approximately 500 blade stations at one azimuthal position to obtain a deviation of .0001 from the exact value of 0.5. The results with the trapezoidal rule and Simpson's integration show that these require fewer

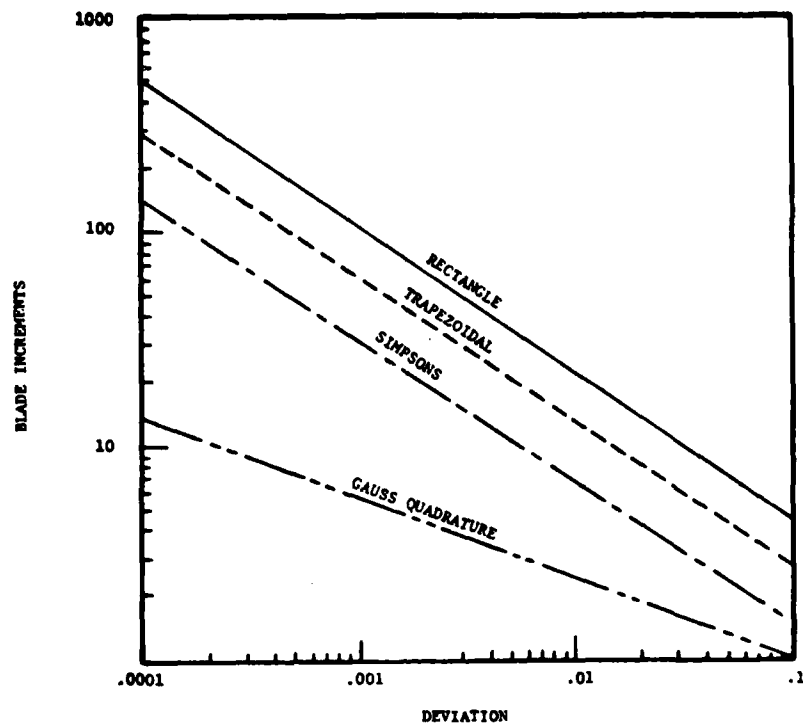


Figure 8. Effects of Different Integration Techniques on the Accuracy of the L(1,1) Term. Corrected Thrust Distribution and $\alpha = 90^\circ$.

blade stations to obtain $L(1,1)$ with the same accuracy as rectangular integration. Figure 8 shows that the method of Gauss Quadrature gives an order-of-magnitude improvement. This shows that Gauss Quadrature integration with 11 radial blade stations will result in a deviation of only .0001 for the $L(1,1)$ term. This results in significant savings in computer time, because the induced velocities can be calculated at only a relatively few blade radial stations for each azimuth position. Another significant advantage of Gauss Quadrature is that the induced velocity is only evaluated at the Gauss point locations. This allows integration in the radial direction from the hub to the tip without explicitly finding the induced velocity at the tip. This is of great importance because the induced velocity (equation (71)) has a singularity at the edge of the rotor disc, $\eta = v = 0$. To obtain the $[L]$ matrix, the induced velocity has to be integrated in the azimuthal as well as the radial direction, as defined by equation (75). Gauss Quadrature is not convenient for the azimuth integration. Consequently, Simpson's rule is employed with azimuthal increments varying from 5° to 30° .

The increment for the streamwise integration is determined such that all the terms of the $[L]$ matrix are calculated with an adequate accuracy. Figure 9 shows that the $L(4,4)$ and $L(5,5)$ terms, which are equal when $\alpha = 90^\circ$, converge at a slower rate than do the other diagonal

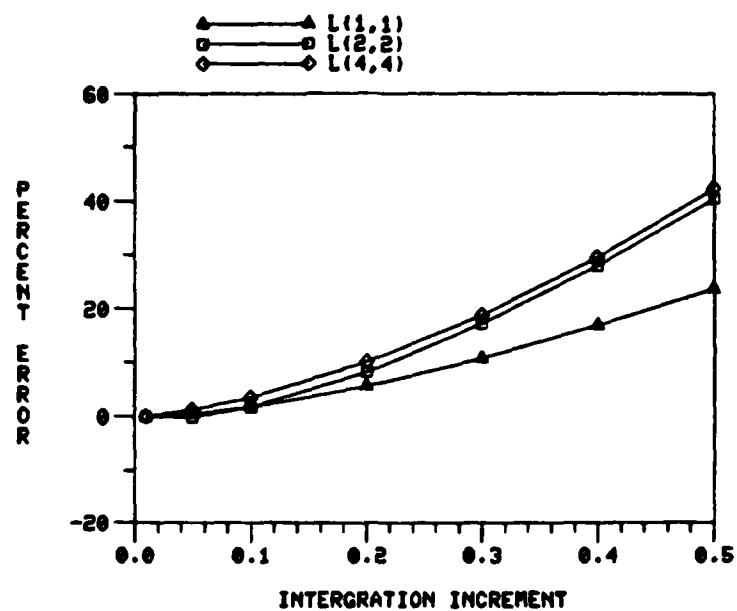


Figure 9. Effects of the Streamline Integration Increment Size on the Accuracy of the Diagonal Elements of the (L) Matrix. Corrected Thrust Distribution and $\alpha = 90^\circ$.

elements. Consequently, the streamwise integration increment was chosen to give accurate answers for all terms of the [L] matrix with a minimum of computer time. (Excessively small increments result in excessive computer time.)

Typically, the azimuth increment must be decreased as the rotor angle-of-attack, α , approaches 0° (edgewise flow). This is because, as α approaches zero, the induced velocity changes rapidly in the azimuthal direction since the disc is in its own wake. The computer program was unable to calculate the induced velocity at $\alpha \equiv 0$ because the streamlines coincide with the rotor disc and create singularities. However, α values as small as 0.2° were possible. The computer time for the steady calculations ranged from 1-4 minutes for $\alpha = 90^\circ$, $\Delta\psi = 30^\circ$ to 19 minutes for $\alpha = .2^\circ$, $\Delta\psi = 5^\circ$. This is the time required to calculate the induced velocity at 10 blade stations, at each azimuth increment, for all 5 loading conditions. Both the [L] matrix and $[L]^{-1}$ are calculated for the 5x5 and 3x3 cases for the given angle of attack during each computer run.

The actuator-disc computer program had the capability of printing the induced-velocity and pressure distributions at all radial and azimuthal positions for all five pressure distributions. This was useful in debugging the computer program, but was not implemented in the majority of the computations.

4.1.2 Unsteady Calculations

The computer code for the steady condition was extended to perform the unsteady calculations of equation (97). The in-phase induced velocities, w , and the out-of-phase induced velocities, u , are integrated in the same manner as the steady calculations except that the weighting functions, $\cos(K\xi)$ and $\sin(K\xi)$ are included. The weighting functions cause the function $\bar{\phi}_z$ to oscillate as a sine or cosine function. As the reduced frequency K is increased, the frequency of oscillation also increases. This means that the streamwise integration increment must decrease as K increases. Consequently, computer time will increase with K . The complex induced velocity is integrated over the rotor disc to obtain the complex 5×5 and 3×3 $[L(K)]$ matrices. The program then inverts both the 5×5 and 3×3 complex matrices $[L(K)]$. The magnitude and phase angle of each element of $[L(K)]^{-1}$ is then calculated. The inverted elements of the 3×3 complex $[L(K)]$ are compared with the upper 3 rows and columns of the inverted 5×5 complex $[L(K)]$ matrix. The program also compares the inverted steady 3×3 and 5×5 $[L]$ matrices with the real parts of the inverted 3×3 and 5×5 complex $[L(K)]$ matrices. The imaginary terms of the inverted 3×3 complex $[L(K)]$ matrix are also compared with the imaginary terms of the upper three rows and columns of the 5×5 inverted $[L(K)]$ matrix. The complex pressure

distribution and complex induced velocities are printed for all azimuth and radial positions, if desired.

As with the steady case, a special case was used to verify the complex induced velocity calculations. Equation (93) was integrated on the disc in closed form to yield the exact value of the apparent mass matrix $[M]$. The exact values were used to check the numerical integration of the complex induced velocities on the disc. The program was found to give accuracy of .0001.

The program is designed such that a single program performs either the steady or the unsteady calculation. If the value of the reduced frequency, K , is zero, then only steady calculations and results are obtained. The computer time required for the unsteady cases is, of course, larger than for the steady cases. The computer time varied from 6 minutes (for the case of $K=0.1$, $\alpha=90^\circ$, and $\Delta\psi=15^\circ$) to 2.5 hours (for $K=300$, $\alpha=90^\circ$, and $\Delta\psi=15^\circ$). As the reduced frequency K is increased, the streamline integration increment must be decreased in order to integrate the oscillating functions of equation (97). To save computation time for large values of K , an approximation is made to equation (97) for values of $\xi > 7$. Equation (97) is approximated by a sinusoidal decaying exponential function of the form

$$\int_{-\infty}^{\xi} \bar{\phi}_{,2} \cos(K\xi) d\xi = \int_{-\infty}^{\xi} c^{-A\xi} \cos(K\xi) d\xi$$

$$\int_{-\infty}^{\xi} \bar{\phi}_{,2} \sin(K\xi) d\xi = \int_{-\infty}^{\xi} c^{-A\xi} \sin(K\xi) d\xi$$

(116)

The advantage of this approximation is that the integration of the exponentially decaying function is evaluated in closed form and added to the numerically integrated values obtained integrating from the disc to $\xi = 7.0$. This approximation results in a 40% savings in computer time with only a 0.25% change in the complex induced-velocity calculations. It should be noted that the 2.5 hours for $K=300$ reflects the use of this approximation. As in the steady case, as the angle-of-attack, α , is decreased, the azimuthal integration increments must also be decreased to account for the more rapid azimuthal variation of induced velocities. The computer time is 40 minutes for $\alpha=1.0^\circ$, $\Delta\psi=5^\circ$, and streamline integration increments of .01 for $r \leq .7$ and .0025 for $.7 < r \leq 1.0$ with the approximation being utilized.

4.2 PRESCRIBED-WAKE COMPUTER PROGRAM

The UTRC prescribed-wake computer program is a large computer program, approximately 4000 lines of code, that requires extensive input data. In addition to the normal blade geometry, airfoil data, control settings, and flight

conditions, that are used; some of the other input variables are number of wake revolutions, number of trailing vortices with their radial locations on the blade, vortex core size, tip roll up geometry, and prescribed-wake geometry. Due to the lack of prescribed-wake data, this last feature was not employed in the research.

The blade geometry and characteristics of the rotor tested by Kuczynski (54-57) were used as blade inputs. This allowed us to compare the calculated thrust with actual data. This also allows a direct comparison with the empirical [L] matrix derived from this test data. Hover calculations, for $\theta_0 = 1^\circ$ and 6° , showed very good agreement with the measured data. During these hover calculations, it was found that the thrust coefficient, C_T , was sensitive to the number of wake revolutions considered. The best results were with 6 wake revolutions, but this resulted in an increase of computer time to 8 minutes for a given pitch setting.

The momentum induced velocity, v_0 , had to be estimated prior to each run. A certain amount of trial and error was required before the v_0 input would agree with the calculated C_T . Equations (1) through (3) depict the relationship between v_0 and C_T . To help in the process the equations of reference 3 were used to find θ_0 for hover and climbing flight. Using these equations reduced the number of runs required to trim. The equations of Wei and Peters (69)

were also used to obtain values for θ_o , θ_s and θ_c in forward flight.

The UTRC program had the capability to interpolate the induced velocities at any number of points on the blade station. Normally, the induced velocity and thrust were calculated at the 9 radial stations of the trailing vortices. The vortices are unevenly spaced with a significant concentration at the tip to model the higher tip circulation of the rotor. To improve accuracy, the induced velocities were interpolated at 10 Gauss points. This allowed us to use both Gauss Quadrature integration of the induced velocity in the radial direction and rectangular integration in the azimuthal direction to obtain v_o , v_s , v_c . The load calculations of equation (109) were performed using rectangular integration of the lift at the trailing-vortex locations in both the radial and azimuthal directions.

To obtain the steady [L] matrix for one flight condition required a minimum of 4 runs at different pitch settings. A separate Fortran program was written to obtain the steady [L] matrix by inverting the [\bar{F}] matrix and performing the matrix multiplication of equation (115).

5. RESULTS AND DISCUSSIONS

The results of the research will be presented in the following order: first, the steady, actuator-disc results will be discussed. Second, the unsteady results will be presented; and, third, the results of the prescribed-wake research will be discussed.

5.1 ACTUATOR-DISC RESULTS

5.1.1 Steady Results

The actuator-disc theory and program previously described has been exercised to obtain the following results. The steady 5x5 [L] matrix, its inverse, and the deviation between the 3x3 and 5x5 inverted [L] matrices were calculated for a range of alphas from 90° to 0.5° . Calculations were made at 10° increments $40^\circ < \alpha < 90^\circ$ and at 5° increments for $0^\circ < \alpha < 40^\circ$. The smaller increments were required to sufficiently define the slopes of the curves near $\alpha = 0$. Each column of the 5x5 [L] matrix is presented for this alpha sweep, figures 10-14.

Figure 10 depicts the first column of the [L] matrix for both the corrected and uncorrected thrust distributions. The shaded symbols represent the uncorrected thrust loading (i.e. only C_1^0 term in the pressure distribution). The star symbols depict the exact results obtained for axial flight, $\alpha = 90^\circ$, and edgewise flight, $\alpha = 0^\circ$, by closed-form integration of equations (72) and (73). Table 3 lists the closed

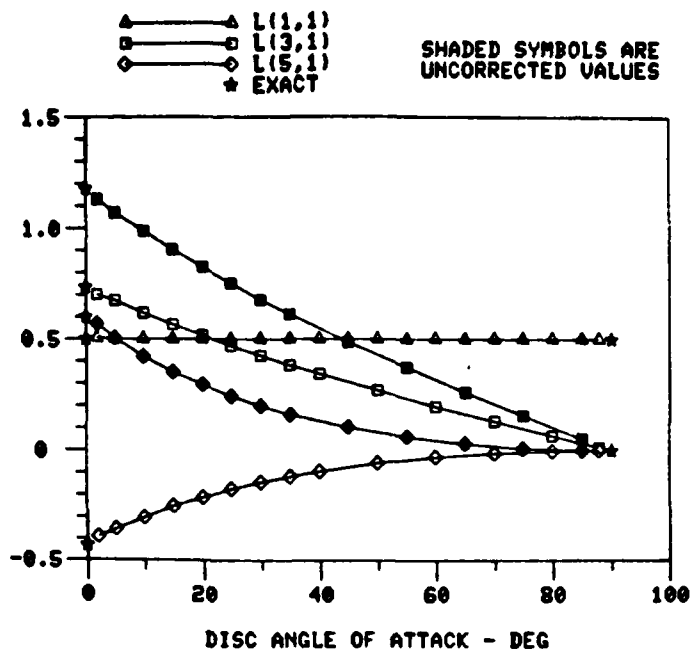
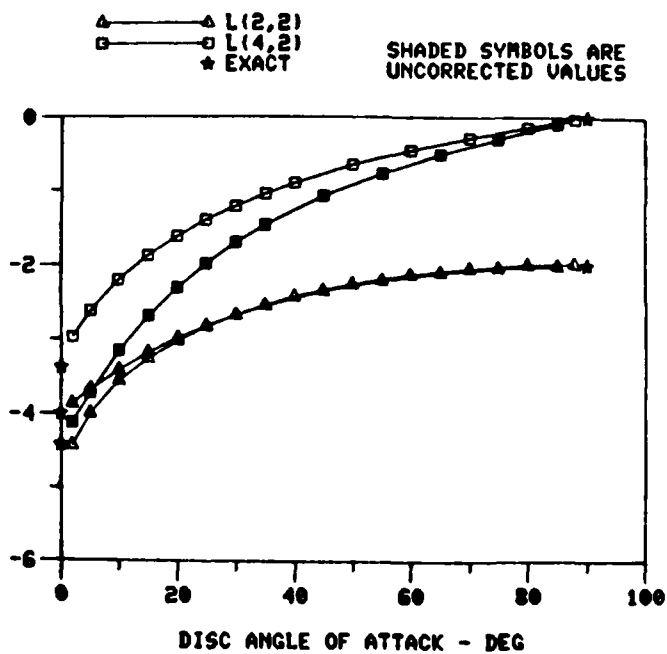


Figure 10. First Column of the [L] Matrix

Figure 11. Second Column of the [L] Matrix



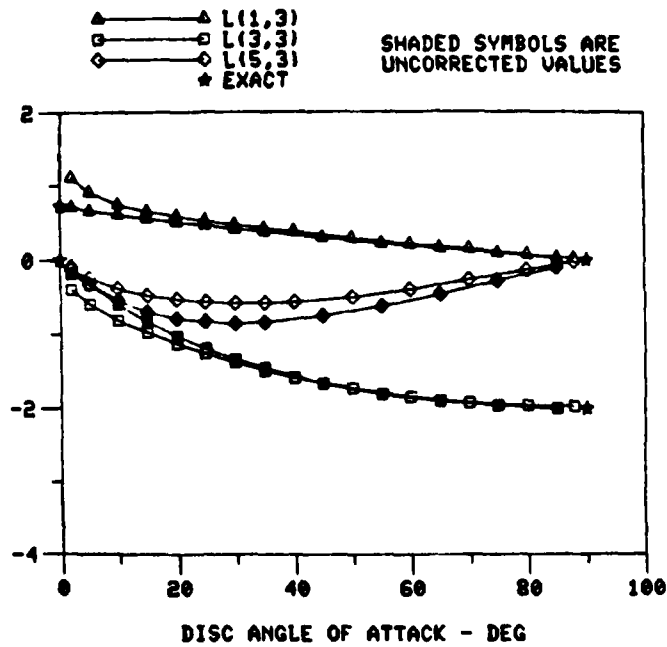


Figure 12. Third Column of the [L] Matrix

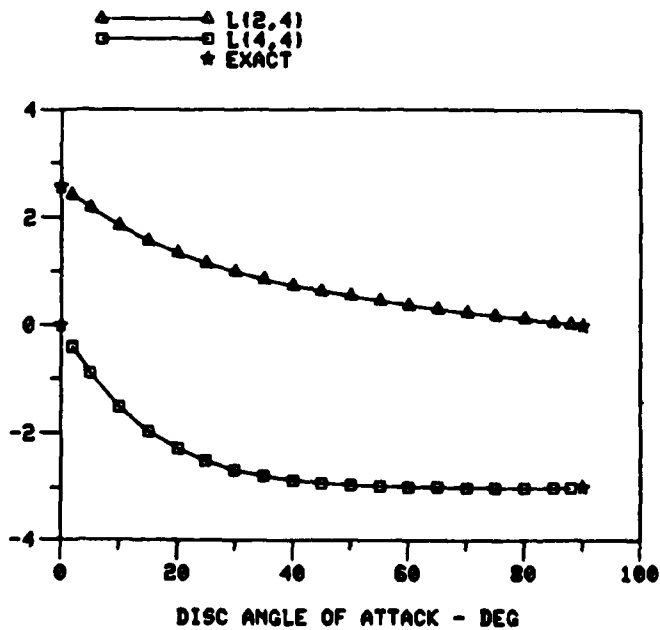


Figure 13. Fourth Column of the [L] Matrix

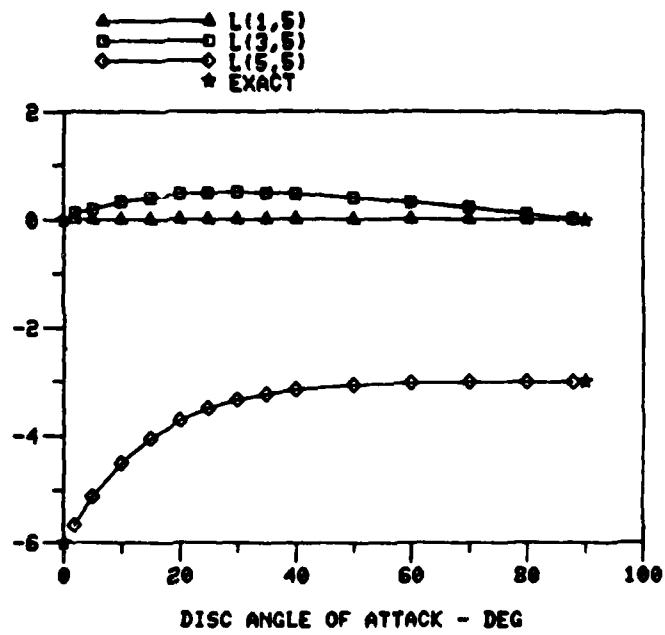


Figure 14. Fifth Column of the [L] Matrix

TABLE 3

L-Matrix for Edgewise Flow[▲]

Element	Uncorrected	Corrected	Vortex	Momentum
L_{11}	$\frac{1}{2} = .500$	$\frac{1}{2} = .500$	$\frac{1}{2} = .5$	$\frac{1}{2} = .5$
L_{22}	-4*	-4*	$-\frac{8}{3} = -2.7$	-2
L_{33}	0	0	0	-2
L_{31}	$\frac{3\pi}{8} = 1.178$	$\frac{15\pi}{64} = .736$	$\frac{1}{2} = .5$	0
L_{13}	$\frac{15\pi}{64} = .736$	$\frac{525\pi}{2048} = .804$	1.0	0
L_{51}	$\frac{3}{5} = .600$	$-\frac{3}{7} = -.429$		
L_{42}	$-\frac{45\pi}{32} = -4.418$	$-\frac{2205\pi}{2048} = -3.382$		
L_{55}	-6*	▲ multiply entries by 1/v *limited numerical integration required		
L_{26}	$\frac{105\pi}{128} = 2.577$			
$*L_{15} + L_{35} + L_{54}$	0			

form results (exact values) for both the uncorrected and corrected pressure distributions for the case of edgewise flow. These values are compared with the results of the vortex and momentum theories of reference (60). The $L(1,1)$ term, v_o due to C_T , is 0.5 for the complete range of α and is also independent of lift distribution. This is the same value predicted by the momentum theory of reference (63). The $L(3,1)$ term, v_o due to C_T , is zero for the case of axial flow (i.e. hover and vertical climbing flight). As α approaches zero, the edgewise flight condition, the $L(3,1)$ term appears to have a linear variation as it approaches the exact value. The uncorrected value of $L(3,1)$ is approximately 60% larger than the corrected value. Interestingly, this term is zero for momentum theory, but is present in the vortex theories. Because the $L(3,1)$ term is positive and greater than $L(1,1)$ it implies that there is an upwash at the front of the rotor. That is to say, since $\cos(\psi)$ is negative for $90^\circ < \psi < 270^\circ$, the resulting induced velocity is negative indicating an upwash. This upwash has physically been measured and is documented in references (13 and 14). The corrected $L(3,1)$ term is essentially the K-factor used by Glauert to obtain a fore-to-aft linear distribution of the induced velocity, equation (4). This term is approximately linear with α and is identical to the K determined by the simple vortex theory of reference (9), as given in equation (6). The $L(5,1)$ term is the second

cosine harmonic of induced flow due to thrust, or v_{2c} due to C_T .

Similar to $L(3,1)$, the $L(5,1)$ term is zero at $\alpha = 90^\circ$ and displays a smooth transition to $\alpha = 0^\circ$. However, it is very interesting that $L(5,1)$ changes sign as the thrust loading is varied from the corrected thrust to the uncorrected thrust distribution. This variation shows that $L(5,1)$ is heavily dependent on the lift distribution. The uncorrected $L(5,1)$ is always positive and increases in a more nonlinear fashion than $L(3,1)$. Because of the $\cos 2\psi$ term, a positive $L(5,1)$ will yield a downwash (or positive induced velocity) at the front of the disc. The harmonic induced velocity perturbation v_{2c} due to an uncorrected thrust distribution, $L(5,1)$, is relatively large; and for $\alpha < 10^\circ$ it is larger than the average value of the induced velocity, v_0 . The $L(5,1)$ term for a corrected thrust distribution appears to have the same general slope but with the opposite sign of the uncorrected $L(5,1)$. The corrected $L(5,1)$ is negative for all values of α up to $\alpha = 90^\circ$ where it is zero. A negative $L(5,1)$ will yield an upwash at the front of the rotor disc, because for $\psi = 180^\circ$ $\cos 2\psi$ is positive and a negative $L(5,1)$ will contribute a negative v_{2c} from equation (74).

In addition to the above numerical results, the variation with α of the first column of the 5×5 $[L]$ matrix was obtained in closed form. Mangler in reference (70)

developed Fourier components of the induced velocity due to C_T . Upon substitution of these values into equation (75) with the indicated integration, the first column of the [L] matrix can be determined. For the corrected lift distribution, the results are

$$L(1,1) = \frac{1}{2v}$$

$$L(3,1) = \frac{15\pi}{64v} \sqrt{\frac{1-\sin\alpha}{1+\sin\alpha}}$$

(117a-c)

$$L(5,1) = \frac{-3}{7v} \left(\frac{1-\sin\alpha}{1+\sin\alpha} \right)$$

For the uncorrected pressure distribution, the α variations are the same as in equation (117); but the coefficients are altered to match the $\alpha=0^\circ$ presented in Table 3.

The second column of the 5x5 [L] matrix and its variation with thrust distribution and angle-of-attack is plotted in figure 11. The only non-zero terms for the second column are $L(2,2)$ and $L(4,2)$. The $L(2,2)$ term is v_s , the sine variation of induced velocity, due to C_L ; and $L(4,2)$ is v_{2s} , the second harmonic sine variation of induced velocity, due to C_L . Figure 11 shows a smooth transition for $L(2,2)$ and $L(4,2)$ as α is varied from 90° to 0° ; with all the curves approaching the exact values as α approaches 0° . The $L(2,2)$ term is nearly independent of lift distribution for $\alpha > 10^\circ$; but for $\alpha < 10^\circ$ a noticeable difference

develops between the corrected and uncorrected values. The uncorrected $L(2,2)$ at $\alpha=0$ represents a 100% increase from its value at $\alpha=90^\circ$. The corrected $L(2,2)$ shows an even larger difference between its values at $\alpha=90^\circ$ and $\alpha=0^\circ$. Both the corrected and uncorrected $L(2,2)$ are negative throughout the complete α range. This is interpreted as an upwash, or negative induced velocity, on the starboard side of the rotor disc ($\psi=90^\circ$, $\sin 90^\circ = +1.0$) and as a downwash, positive induced velocity, on the port side ($\psi=270^\circ$ and $\sin 270^\circ = -1.0$) for a positive rolling moment. The $L(4,2)$ term has a dependence on lift distribution that is independent of α . The corrected and uncorrected $L(4,2)$ are both zero at $\alpha=90^\circ$ and they increase nonlinearly as α varies from 90° to 0° . At $\alpha < 10^\circ$ the magnitude of the uncorrected $L(4,2)$ is larger than that of the corrected $L(4,2)$. At $\psi=135^\circ$ the $L(4,2)$ value is positive ($\sin 2\psi = -1$ at $\psi=135^\circ$) and $L(2,2)$ is negative ($\sin \psi = .707$ at $\psi=135^\circ$) with the resulting induced velocity from a positive rolling moment being positive at this point on the rotor. This phenomenon is also apparent at $\psi=225^\circ$ where the signs are reversed. This phenomenon is not apparent for the corrected thrust case, where the $L(2,2)$ term is larger than $L(4,2)$ for all alphas.

Figure 12 gives the third column of the 5×5 $[L]$ matrix, which is the induced flow due to pitching moment, C_M . At $\alpha=90^\circ$ the $L(3,3)$ term is -2.0 , which is the same value as $L(2,2)$ for $\alpha=90^\circ$ and is the same as predicted by momentum theory. Thus, for the case of $\alpha=90^\circ$ the $L(2,2)$ and $L(3,3)$ terms are equal, which is to be expected due to the symmetry of the airflow through the rotor for axial flight. The $L(1,3)$ is the average induced velocity, v_o ; $L(3,3)$ is the fore-to-aft induced velocity, v_c ; and $L(5,3)$ is the second harmonic of the fore-to-aft induced velocity distribution, v_{2c} . The corrected and uncorrected $L(1,3)$ and $L(5,3)$ terms are zero at $\alpha=90^\circ$. The $L(1,3)$ term varies smoothly with α , with a difference between the corrected and uncorrected results for $\alpha < 30^\circ$. The difference between the corrected and uncorrected $L(1,3)$ is a maximum at $\alpha=0$ where the corrected term appears to have a linear variation; and the uncorrected term becomes increasingly nonlinear for $\alpha < 15^\circ$. The $(1,3)$ term for a positive pitching moment will yield a positive average induced flow, v_o , which will add to the v_o due to thrust causing it to increase. The $L(3,3)$ term is very interesting in that it varies from a value of -2 at $\alpha=90^\circ$ to zero at $\alpha=0$. This term has a smooth nonlinear variation that is independent of lift distribution over the range of $30^\circ \leq \alpha \leq 90^\circ$. For $\alpha < 30^\circ$ the corrected value has a slightly larger absolute value. However, both the corrected and uncorrected $L(3,3)$ values are zero at $\alpha=0$. This means that there is no

fore-to-aft or cosine component of induced velocity at $\alpha=0$ for a pitching moment. $L(5,3)$ is also zero at $\alpha=0$ which means that there is no second-harmonic variation of the fore-to-aft gradient. The $L(5,3)$ term varies from 0 at $\alpha=90^\circ$ to 0 at $\alpha=0^\circ$ with small negative values between. This term shows a dependence on lift distribution, with the absolute value being the largest at $\alpha=30^\circ$ for the uncorrected pressure distribution.

Figures 13 and 14 depict the effects of the second-harmonic loading distribution on the induced flow. These results can be used to determine if perturbations in the higher-harmonic air loads will cause significant changes in v_o , v_s , or v_c and thereby invalidate one of the basic assumptions of dynamic inflow theory. For the higher-harmonic loadings, a single radial loading distribution was used, (i.e., an uncorrected pressure distribution).

The fourth column of the 5×5 $[L]$ matrix yields the induced flow due to C_{2L} which is a second-harmonic sine variation in load. The results for C_{2L} are presented in figure 13. At $\alpha=90$ the $L(2,4)$ term is zero and $L(4,4)$ is -3. The term $L(4,4)$ represents a second-harmonic of the side-to-side induced velocity variation. Figure 13 shows a smooth variation of $L(2,4)$ and $L(4,4)$ with alpha. At $\alpha=0$ $L(4,4)$ is zero but $L(2,4)$ is 2.577. It appears that the positive $L(2,4)$ will decrease the magnitude of v_s (for a positive C_L) because $L(2,2)$ is negative. This effect is independent of α .

The terms $L(2,4)$ and $L(4,4)$ vary nonlinearly with α , both displaying increasing slopes as α is decreased from 90° . The $L(4,4)$ term is more steep and has a slightly larger variation in its magnitude as α varies from 90° to 0° . The $L(4,4)$ term, second-harmonic sine variation of induced velocity due to $\sin 2\psi$ loading, is zero at α of 0° . However, $L(4,2)$ of figure 11, which is the second-harmonic sine variation of induced velocity due to a sine loading, is nonzero at $\alpha=0^\circ$.

Figure 14 depicts the fifth column of the $[L]$ matrix, which is the induced velocity due to a second-harmonic cosine variation of the pressure distribution. The $L(1,5)$ term, v_o due to C_{2M} , is zero for all α . This is in contrast to the $L(1,3)$ term which is nonzero. The $L(3,5)$ term is observed to vary from 0 at $\alpha=90^\circ$ to a maximum at $\alpha=30^\circ$. It returns to zero at $\alpha=0^\circ$. This means that the second harmonic cosine loading will result in a small positive first harmonic cosine variation of the induced flow, v_c . The $L(5,5)$ term is equal to $L(4,4)$ at $\alpha=90^\circ$, which is expected due to the symmetry of the airflow. The $L(5,5)$ term has a smooth nonlinear variation with α and appears to be of the opposite sign of the $L(4,4)$ term. Thus, as α approaches zero the magnitude of $L(5,5)$ is increasing to a maximum of -6 at α equal zero. This shows that for the case of edgewise flight, there is a second harmonic cosine variation of the induced velocity due to a

second-harmonic cosine variation of the pressure distribution. This is in contrast to $L(3,3)$ and $L(5,3)$ for edge-wise flight, in that there is neither a first nor second cosine variation of induced velocity due to a first-harmonic cosine variation of the pressure distribution.

The inverse of the steady $[L]$ matrix is required in determining the unsteady induced velocities as given by equation (32) and (106). Consequently, it is important to determine the effects of the corrected and uncorrected pressure distribution on the inverse of the $[L]$ matrix.

Figure 15 is the first column of the inverted $[L]$ matrix; and for the steady case, $\{\dot{v}\} = 0$, it represents the aerodynamic loading $\{F\}$ due to v_0 . Figure 15 shows a smooth transition for all terms from $\alpha = 90^\circ$ to 0° . At $\alpha = 90^\circ$, all terms are zero except the $L[1,1]^{-1}$ term, which is 2.0. It should be noted that for axial flight the $[L]$ matrix is a diagonal matrix with no cross-coupling terms. Consequently, the inverse of the $[L]$ matrix for $\alpha = 90^\circ$ is straight-forward and is the reciprocal of each element of the $[L]$ matrix. The $L[1,1]^{-1}$ term, C_T due to v_0 , is dependent on the lift distribution and has a nonlinear variation from $\alpha = 90^\circ$ to $\alpha = 0^\circ$; where the term is zero. The $(3,1)$ term, C_M due to v_0 , is also dependent on the lift distribution and appears to be a linear variation from 0 at $\alpha = 90^\circ$ to its maximum at $\alpha = 0^\circ$. At $\alpha = 0^\circ$ there is considerable difference in the $(3,1)$ term for the corrected and uncorrected load distributions.

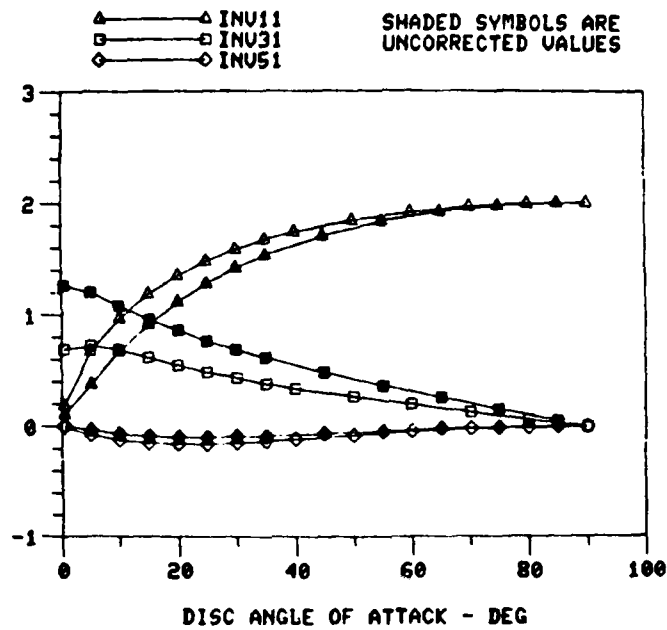


Figure 15. First Column of Inverted [L] matrix

Figure 16 is the second column of the inverted [L] matrix and represents the loading due to v_s for the steady condition. The $L(2,2)^{-1}$ term is shown to vary from a maximum at $\alpha=90^\circ$ to zero at $\alpha=0$. There is little variation of $L(2,2)$ term with thrust distribution. The (4,2) term, however, shows some dependence on lift distribution, except at $\alpha=0^\circ$ and 90° where there is no difference. The (4,2) term is zero at $\alpha=90^\circ$ and increases smoothly to its maximum at $\alpha=0^\circ$.

The third column of the inverted [L] matrix is plotted in figure 17. The $L(1,3)^{-1}$ term shows a nonlinear variation from 0 at $\alpha=90^\circ$ to a maximum at $\alpha=90^\circ$. A significant difference between the corrected and uncorrected values indicate this term's dependency on lift. The $L(1,3)^{-1}$ term is C_T due to v_c . The $L(3,3)$ term is invariant with α and lift distribution for practical purposes. The negative value for this term indicates that a positive v_c , reflects a negative C_M . The $L(5,3)^{-1}$ term, C_{2M} due to v_c , is nearly zero for all alpha with a slight variation for $\alpha < 30$. In this same alpha range, there is a slight dependency of the $L(5,3)^{-1}$ term on lift distribution.

The fourth column of the inverted [L] matrix represents the aerodynamic loading, {F}, due to v_{2s} which is the second-sine-harmonic of the induced velocity. Figure 18 is the fourth column of the inverted [L] matrix. Both the $L(2,4)^{-1}$ and $L(4,4)^{-1}$ terms are dependent on the lift distribution for $\alpha < 60^\circ$. The corrected thrust distribution results in larger absolute values for both terms. $L(2,4)^{-1}$, C_L due to v_{2s} is

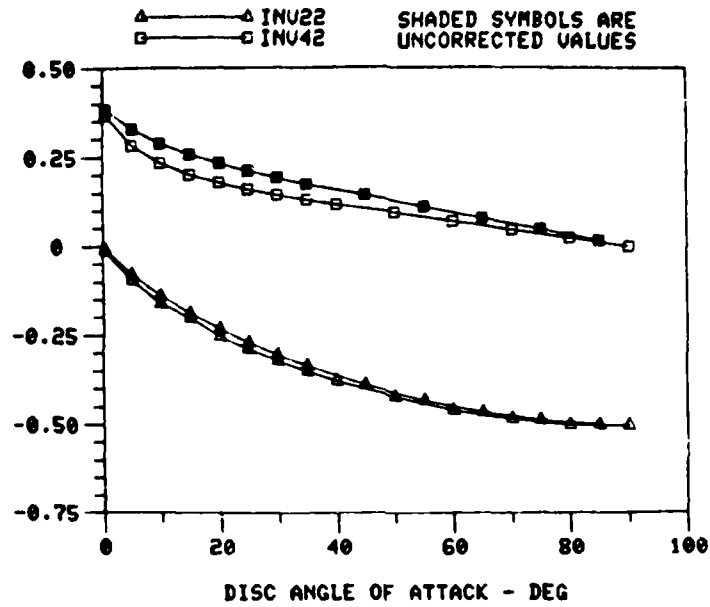


Figure 16. Second Column of Inverted [L] Matrix

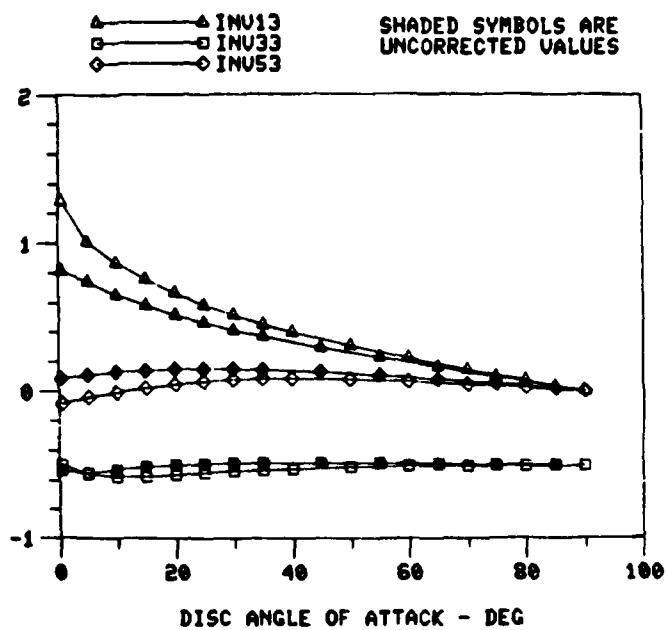


Figure 17. Third Column of Inverted [L] Matrix

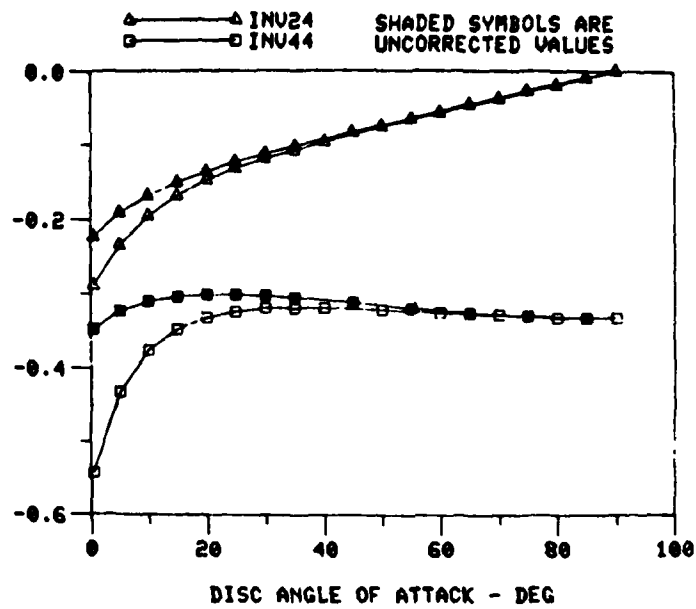


Figure 18. Fourth Column of Inverted [L] Matrix

zero at $\alpha=90^\circ$ appears to vary linearly in the range; $40^\circ \leq \alpha \leq 90^\circ$; and becomes very nonlinear as α approaches zero. The corrected $L(4,4)^{-1}$ term is seen to be extremely nonlinear for $\alpha < 20^\circ$ and appears to have an almost infinite slope at $\alpha=0$. This term is C_{2L} due to v_{2s} .

The fifth and last column of the inverted [L] matrix is presented in figure 19. It is apparent that the terms in this column are essentially independent of thrust distribution. The $L(1,5)^{-1}$ term, C_T due to v_{2c} , and $L(3,5)^{-1}$, C_M due to v_{2c} , are zero at $\alpha=0^\circ$ and $\alpha=90^\circ$, with a somewhat symmetric variation between these angles-of-attack. The $L(5,5)^{-1}$ term C_{2M} due to v_{2c} , varies smoothly from $\alpha=90^\circ$ to $\alpha=0^\circ$, with its absolute value being the largest at $\alpha=90^\circ$.

When inverting a nondiagonal matrix, changing the values of some of the elements will affect the total inverted matrix. As part of this research, the difference between the 5x5 and 3x3 inverted [L] matrices was investigated. The elements of the 3x3 [L] matrix are readily obtainable by just eliminating the fourth and fifth columns and rows of the 5x5 [L] matrix. However, this procedure is not valid on the inverted matrix due to the interaction of all the elements. Thus we wish to compare the upper 3x3 portion of the two matrices.

Instead of showing the elements of the 3x3 inverted [L] matrix, we show the deviation between the inverted 5x5 [L] matrix and the inverted 3x3 [L] matrix. The deviation matrix is defined as

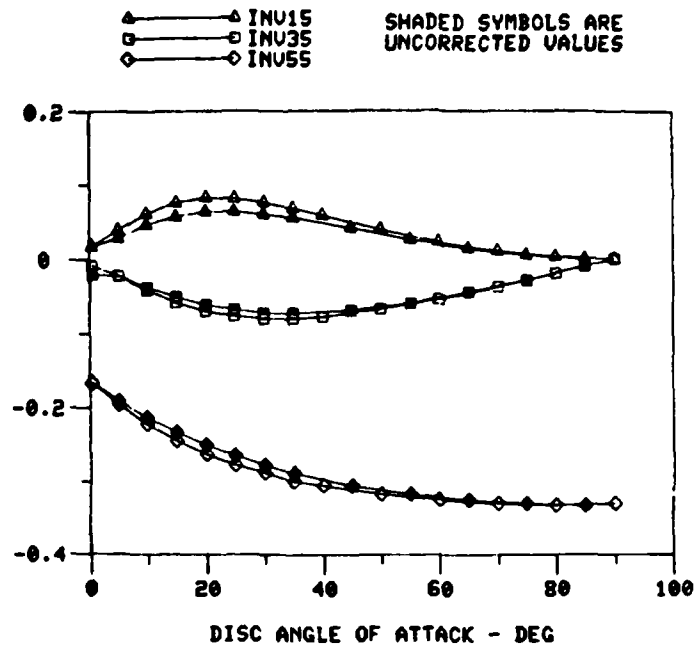


Figure 19. Fifth Column of Inverted [L] Matrix

$$\begin{aligned} \text{DMAT}(I,J) &= L_5(I,J)^{-1} - L_3(I,J)^{-1} \\ I &= 1,3 \\ J &= 1,3 \end{aligned} \quad (118)$$

Figures 20 and 21 give the difference between the inverted 5x5 and 3x3 [L] matrices. It is apparent from both of these figures that the deviation at $\alpha=90^\circ$ is zero for all elements and all loading conditions. Elements (1,1) and (3,1) vary smoothly from 0 at $\alpha=90^\circ$ to nearly zero at $\alpha=0^\circ$ with a maximum deviation occurring at $\alpha=20^\circ$. The absolute values of the corrected (1,1) and (3,1) terms have a larger deviation than the uncorrected values. The L(1,3) and L(3,3) terms plotted in figure 21 have a shape similar to the elements of the first column shown in figure 20. However, for the (1,3) and (3,3) terms, the absolute values of the corrected distributions are larger than those of the uncorrected. This is opposite to that shown in figure 20. The (2,2) element results in the largest deviation between the inverted 3x3 and 5x5 [L] matrices; for the case $\alpha=0^\circ$ and an uncorrected loading. It should be noted that neither the 3x3 nor 5x5 inverted matrices are singular, and all elements display smooth variations with α .

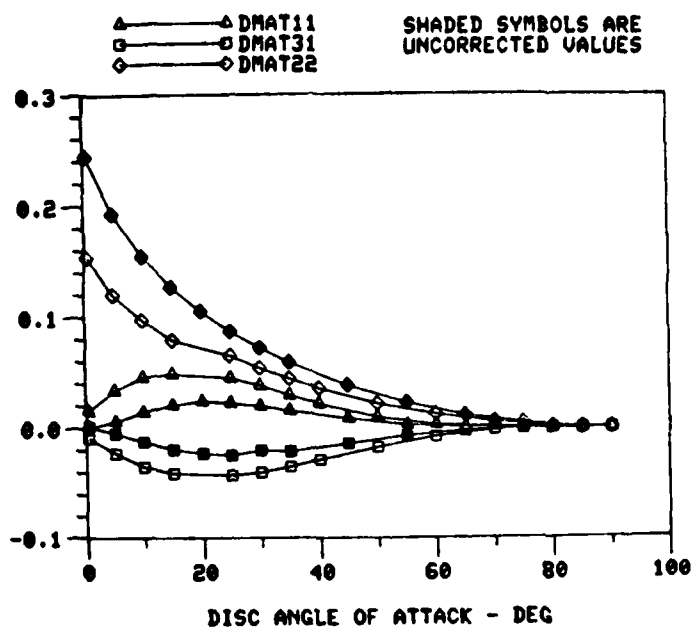
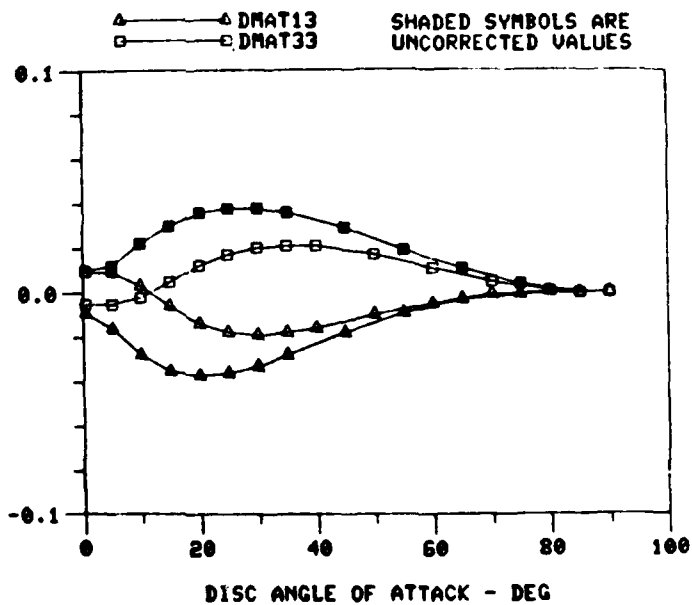


Figure 21. Third Column of the Deviation Matrix



5.1.2 Unsteady Results

In this section, the properties of the inverted complex $[L]$ matrix will be examined. The complex $[L]$ matrix was calculated as described in the previous sections, considering the two different solution techniques of Superposition of Velocities (S.V.) and Superposition of Pressures (S.P.). The significance of the results to be presented in this section is that a true rotor should behave somewhere between the two theories. Thus, the results will represent an upper and lower boundary of the dynamic inflow model.

The first case to be presented is the case of axial or hovering flight. The unsteady effects of axial flight have been fairly well documented by previous analyses and tests. Both the complex $[L(K)]$ matrix and the inverted complex $[L(K)]^{-1}$ matrix are diagonal matrices for $\alpha=90^\circ$. This is advantageous in that none of the elements are coupled, meaning that each element is straightforward and independent of the other elements. Figures 22-24 give comparisons of the imaginary parts of the diagonal element of the inverted complex $[L]$ matrix as calculated by each method. These figures depict both the corrected and uncorrected load distributions. As mentioned in section 3.1.2, equation (93) is evaluated in closed form for the special case of $v=0$, $\alpha=90^\circ$ to obtain the apparent mass terms. The results of this closed-form apparent mass calculation is

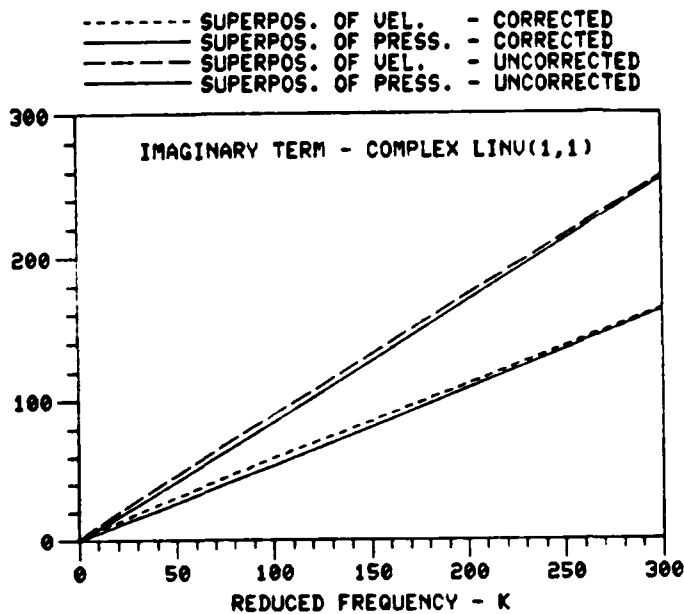
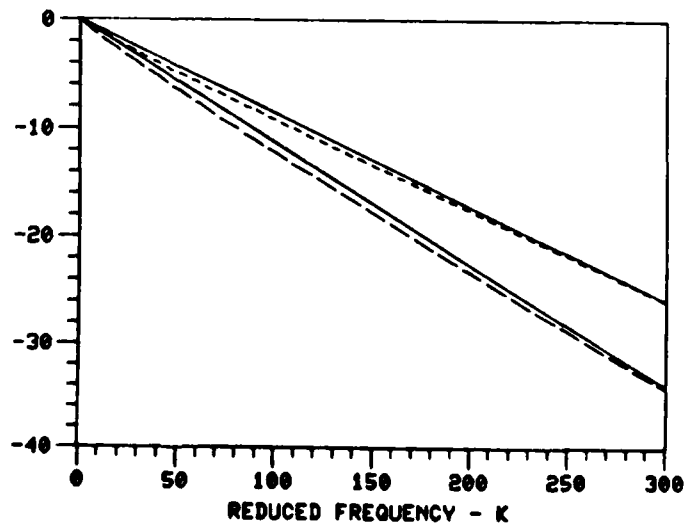


Figure 22. Imaginary Part of the (1,1) Element of the Inverted Complex L(K) Matrix, $\alpha = 90^\circ$

IMAGINARY TERMS - COMPLEX LINU(2,2) & M(3,3)

----- SUPERPOS. OF VEL. - CORRECTED
 ----- SUPERPOS. OF PRESS. - CORRECTED
 ----- SUPERPOS. OF VEL. - UNCORRECTED
 ----- SUPERPOS. OF PRESS. - UNCORRECTED

Figure 23. Imaginary Part of the (2,2) or (3,3) Element of the Inverted Complex L(K) Matrix, $\alpha = 90^\circ$



IMAGINARY TERMS - COMPLEX LINU(4,4) & LINU(5,5)

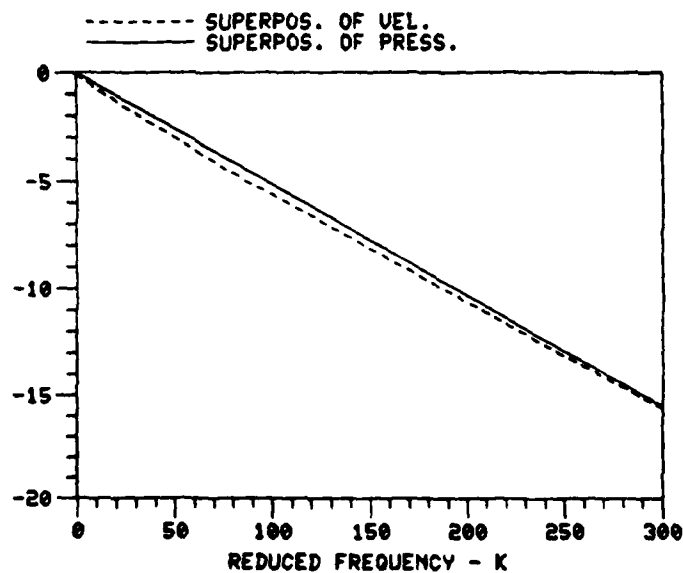


Figure 24. Imaginary Part of the (4,4) or (5,5) Element of Inverted L(K) Matrix, $\alpha = 90^\circ$

TABLE 4

Elements of M-Matrix

Element	Uncorrected	Corrected
M_{11}	$\frac{8}{3\pi} = .8488$	$\frac{128}{75\pi} = .5432$
$M_{22} = M_{33}$	$-\frac{16}{45\pi} = -.1132$	$-\frac{256}{945\pi} = -.0862$
$M_{44} = M_{55}$	$-\frac{256}{1575\pi} = -.0517$	-
$M_{4j}, 1 \neq j$	0	0

given in Table 4. Several points are noteworthy. First, the uncorrected values of M_{11} , M_{22} , and M_{33} are identical to the values obtained by Peters (63) who used potential theory to determine the apparent mass of an impermeable disc. Second, there are significant differences between the apparent mass for corrected and uncorrected lift distributions. Therefore, the apparent mass terms are more sensitive to pressure distributions than are the steady terms. Third, the apparent mass terms decrease with increasing harmonics of induced flow, v . The apparent mass terms of Table 4, both corrected and uncorrected, are used in obtaining the inverted complex $[L]$ matrix by the superposition of pressure (S.P.) theory.

From comparing figures 22 through 24, it is apparent that all elements of the complex $[L]$ matrix are zero for a reduced frequency of zero. The reduced frequency, $K=\omega/v$, is defined as the ratio of the rotor oscillating frequency, ω , to the free-stream velocity-ratio, v , of the rotor. The (1,1) term is always positive and all other terms are negative. At relatively large reduced frequencies, $K \approx 300$, the S.V. and S.P. give the same results. The rate of convergence appears to be independent of thrust distribution or of harmonics of the induced velocity. The latter statement implies that the rate of convergence for all elements is about the same. Comparison of the imaginary values of each element of the matrix at $K=300$ verifies the closed-form

result that stated that the apparent mass terms decrease with increasing harmonics of v . It is interesting to note that the uncorrected thrust distribution results in a larger imaginary term for figures 22 and 23 than does the corrected thrust distribution. A comparison of the two solution techniques shows that the largest absolute differences are in the range $50 \leq K \leq 200$. The difference between results of the two solution techniques appears to be the same for either the corrected or uncorrected load distribution. Finally, for a reduced frequency in the range of $0 \leq K \leq 20$ the differences between the solution techniques is small, although the percentage difference is large. This can be seen more clearly in the apparent mass terms.

The apparent mass for either solution technique can be obtained from the ratio $L^{-1}(K)/K$ in figures 22-24. Thus K times each apparent mass term will yield the imaginary part of the inverted complex L -matrix. A comparison of the apparent mass terms as calculated by each solution technique is presented in figures 25-27 for the case of axial flow. Due to the symmetry of the airflow through the rotor for axial flow, $\alpha=90^\circ$, the $M(2,2)$ and $M(3,3)$ terms are equal and the $M(4,4)$ and $M(5,5)$ terms are also equal. Figures 25-27 give a comparison of the relative magnitude of the apparent mass terms. It is seen that the $M(1,1)$ term is larger than the $M(2,2)$ and $M(3,3)$ terms which, in turn, are larger than the $M(4,4)$ and $M(5,5)$ terms. The $M(1,1)$ term is

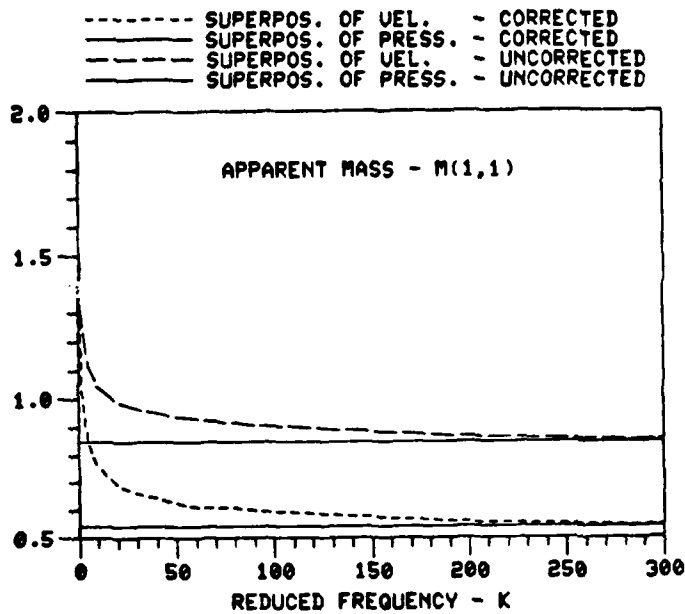
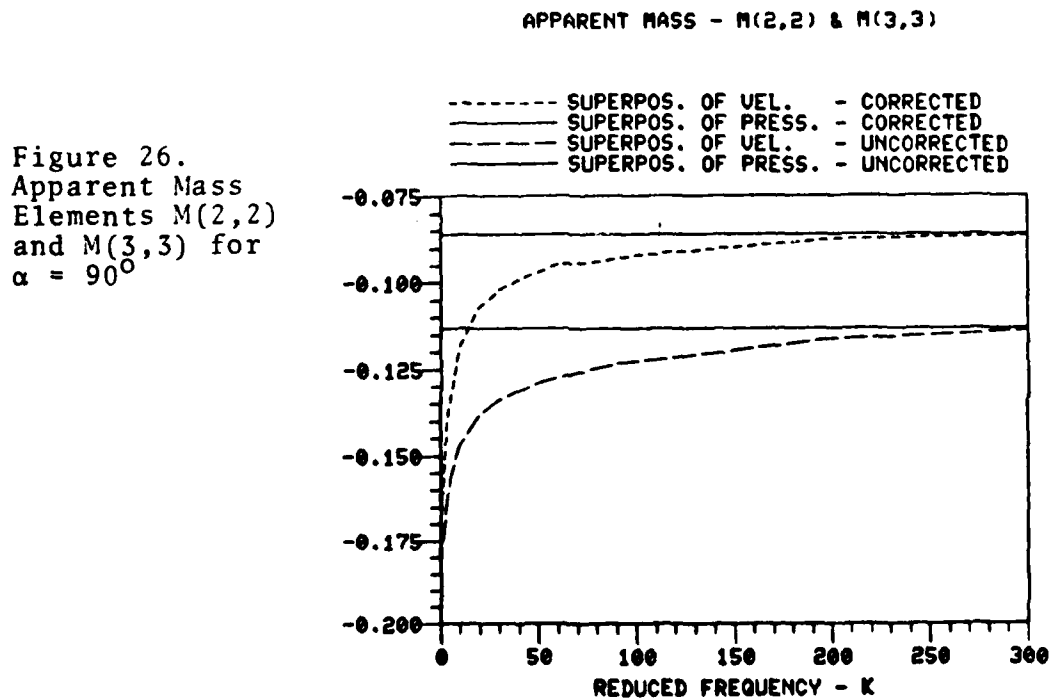


Figure 25. Apparent Mass Element $M(1,1)$ for $\alpha = 90^\circ$



positive and the other terms are negative. It is interesting to note that the apparent mass terms due to the corrected pressure distribution are always smaller than the apparent mass associated with the uncorrected pressure distributions. This can possibly be explained by the fact that with the corrected pressure distribution the lift tends towards the edge of the disc, while for the uncorrected pressure distribution it tends towards the hub. The apparent mass elements calculated by the S.V. method asymptotically approach infinity as K approaches zero. This is exactly analogous to the case for an unsteady wing in which the $\log(K)$ term in the Theodorsen function given an infinite slope at $K=0$, Ref. (71). However, as K is increased, the apparent mass calculated by the method of S.V. exponentially approaches the apparent mass calculated by the S.P. method. At a reduced frequency of $K=300$, figures 25-27 show that the apparent mass of both methods agree. Even though there is a large difference in the apparent mass terms calculated by the superposition of pressures and velocities in the $K < 50$ range, the reduced frequency is small and consequently the imaginary terms are relatively small, and the effects of the different apparent masses are not great.

To better understand the difference between the inverted complex L-matrix as calculated by S.P. and S.V. methods, it is good to compare the magnitudes and phase angles of the

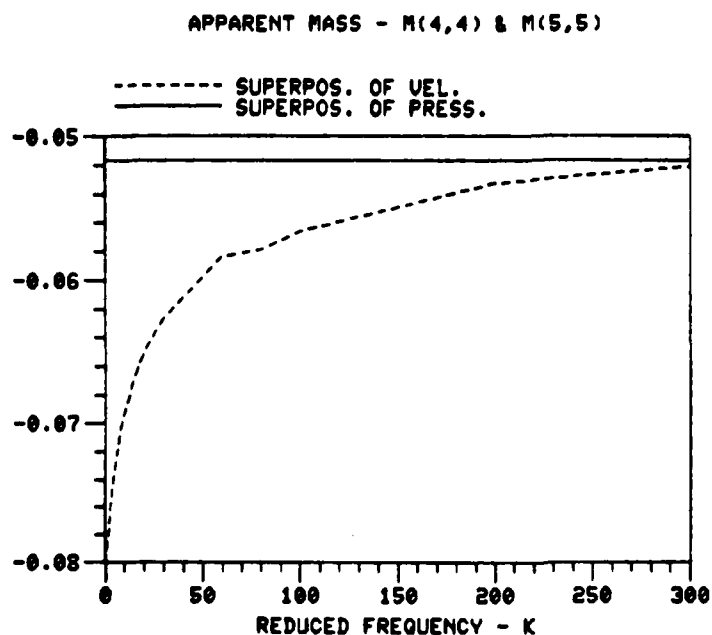
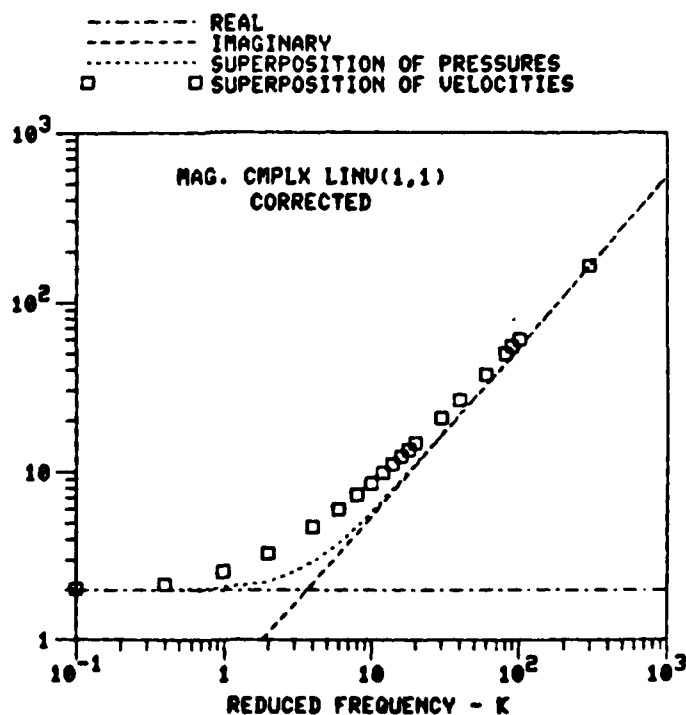


Figure 27.
 Apparent Mass
 Elements $M(4,4)$
 and $M(5,5)$ for
 $\alpha = 90^\circ$

Figure 28.
 Magnitude of the
 (1,1) Element of
 Inverted Complex
 $L(K)$ Matrix at
 $\alpha = 90^\circ$ with
 Corrected Pressure



complex elements for each method. The magnitudes of the elements of the inverted complex L-matrix are presented in figures 28-32. The magnitudes are given on a log-log graph for both the corrected and uncorrected pressure distributions for the case of axial flight. (We recall that the (4,4) and (5,5) elements are always uncorrected.)

Figure 28 presents the magnitude of the (1,1) element of the complex L-matrix as calculated by each theory for a corrected thrust distribution. The magnitudes were plotted on a log-log scale, because this affords the capability to compare magnitudes at both high and low K values without masking small differences. The S.V. magnitudes are for discrete K values over the range of interest, $.1 \leq K \leq 300$. The S. P. magnitudes are obtained from the square root of the sum of the squares of the real and imaginary terms. The real part, shown on the figure as a dot-dashed line, is the (1,1) term of the inverted steady L-matrix for $\alpha=90^\circ$. This value can be obtained from figure 15. The imaginary term for the S.P. method, shown on the figure as the large dashed line, is the apparent mass $M(1,1)$ multiplied by the reduced frequency K. The combined magnitude of the real and imaginary parts are shown as the dotted line. It is interesting to note that when the lines of the real or imaginary component coalesce with the magnitude line, then the respective component is predominantly larger than the other term. For example, in figure 28 for $K < .3$ the real part dominates and for $K > 30$ the imaginary part dominates. The maximum

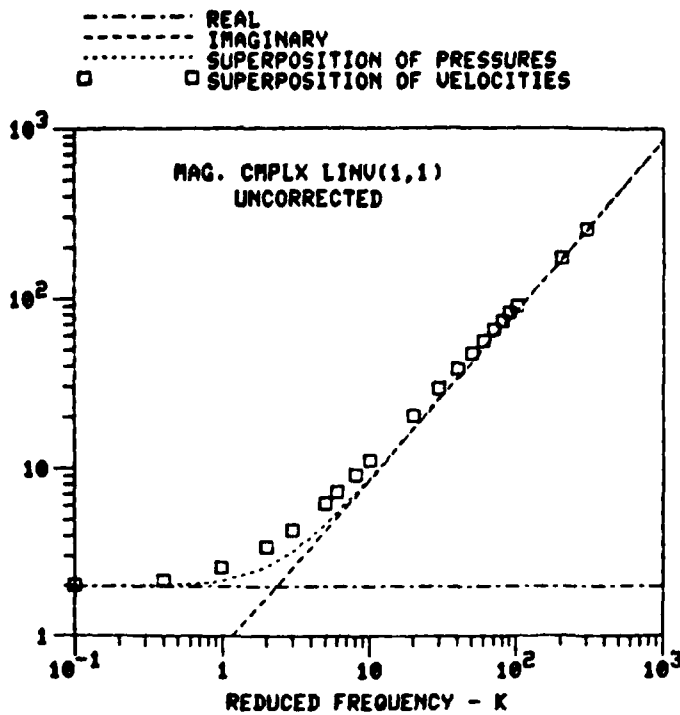
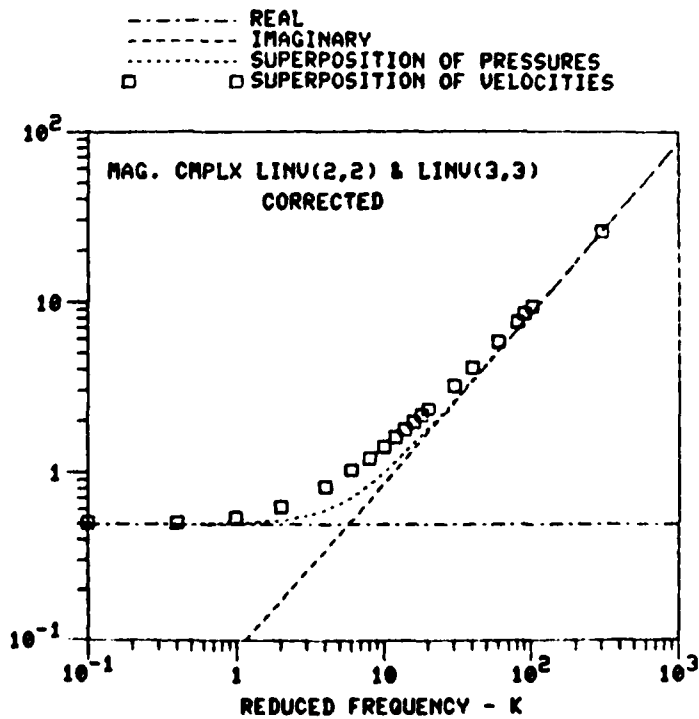


Figure 29.
Magnitude of the
(1,1) Element of
Inverted Complex
L(K) Matrix at
 $\alpha = 90^\circ$ with
Uncorrected Pressure

Figure 30.
Magnitude of the
(2,2) and (3,3)
Elements of Inverted
Complex L(K) Matrix
at $\alpha = 90^\circ$ with
Corrected Pressure



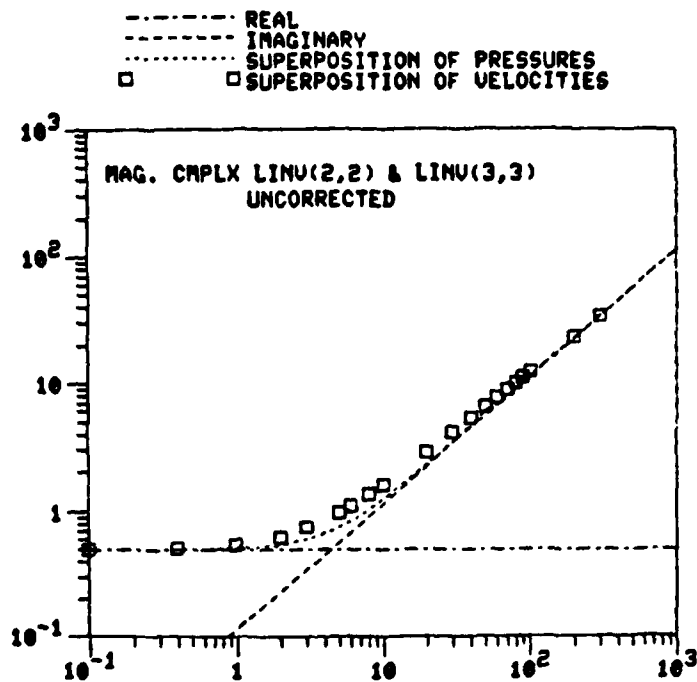
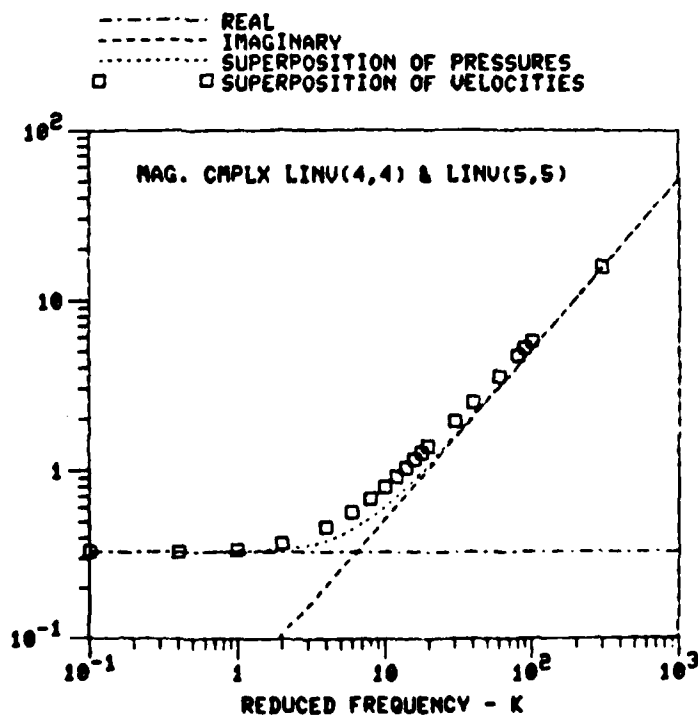


Figure 31.
Magnitude of the
(2,2) and (3,3)
Elements of
Inverted Complex
 $L(K)$ Matrix at
 $\alpha = 90^\circ$ with
Uncorrected
Pressure

Figure 32.
Magnitude of the
(4,4) and (5,5)
Elements of
Inverted Complex
 $L(K)$ Matrix at
 $\alpha = 90^\circ$



difference between the S.P. and S.V. theories is for the case of corrected thrust loading in the range of $1 \leq K \leq 10$. At $K = 3$, the difference is close to a factor of 2.0. Therefore, we conclude that either theory may deviate by $\pm 30\%$ from the true value at $K = 3$. Although this is disappointing, especially since this is in the range of most interest, we recall that the effect of dynamic inflow is itself a correction factor. Thus, errors of 30% in a correction term may be acceptable. Figure 29 gives the (1,1) term for uncorrected thrust, and it appears to have a closer agreement between the two theories than does the corrected. For axial flight, the real part for the corrected and uncorrected thrusts are the same. However, there is a difference in the apparent mass (i.e. complex part) of the L inverse matrices. Comparing figures 30 and 31, one can see that the uncorrected pitch and roll moments yield better agreement between the S.P. and S.V. Since most uses of dynamic inflow (such as air resonance) are primarily roll and pitch, this is further justification for the adequacy of dynamic inflow theory. These figures also show difference in the slopes of imaginary components (of the S.P. theory) between the corrected and uncorrected pressure distributions. This is due to the difference in apparent mass. Figure 32 shows very good agreement between the two solution techniques for the 2/rev elements but it also shows that these are smallest of all the elements. The good correlation for the (4,4) and (5,5) term is tempered by the fact that these terms are manifested

by the second-harmonic pressure distribution, which for real rotors is of a secondary effect.

To fully understand the behavior of the inverted complex L-matrix, it is beneficial to look also at the phase angle variation of each element as a function of reduced frequency. The phase angle can be considered to be a time lag between the in-phase and out-of-phase induced velocities. Figures 33 - 37 present the phase angle of all nonzero elements of the inverted complex L-matrix at $\alpha = 90^\circ$. The phase angles, similar to the magnitudes, are plotted for varying reduced frequencies in the range of $.1 \leq K \leq 300$ and for both the corrected and uncorrected pressure distributions. It should be noted that these are semi-log plots with reduced frequency being plotted on a logarithmic scale. For ease of comparison, the phase angles of both solution techniques, Superposition of Pressures (S.P.) and Superposition of Velocities (S.V.), are presented on the same figure. The phase angle is the arc tangent of the ratio of the imaginary part to the real part. For the S.P. method, the real part is the inverted, steady L-matrix and the imaginary term is the apparent mass multiplied by the reduced frequency. We recall from the results of section 5.1.1 that, for $\alpha = 90^\circ$, the real term is independent of thrust distribution. Therefore, the difference in the S.P. phase angles between the corrected and uncorrected pressure distributions is due to the difference in the apparent mass for these two distributions. The phase angle for S.V. is defined as the arc tangent of the

ratio of the imaginary part to the real part of the inverted complex L-matrix obtained by integration of the complex induced velocities of equation (97).

Figure 33 presents the phase angles for the (1,1) element for the corrected thrust distribution. This figure shows that for $K < 5$ that the phase angles calculated by the S.V. method are larger than the S.P. phase angles. This trend is reversed for $K > 11$ where the S.V. phase angles are smaller than the S.P. phase angles. The two techniques agree at a reduced frequency of approximately 5. It is interesting to note that at $K = 300$, the phase angles of the S.P. and S.V. differ by approximately 5 degrees, although figure 28 shows that the magnitudes of the two methods agree at this point. It can be noted that, at the higher reduced-frequency range, the slopes of the S.P. and S.V. phase angles differ slightly. Since the real part of the S.V. phase angle is larger than the real part of the S.P., which is itself constant for all K , one would expect the curves to be nearly parallel and the slopes to be equal for high reduced frequencies. However, the slopes appear to be different. This can be explained by the fact that the real part of the S.V. technique is becoming increasingly larger for an increasing K . (This will be shown later) The above comments are also applicable to the phase angle due to the pitch and roll moments shown in figure 35 and the phase angle from second-harmonic load distribution shown in figure 37.

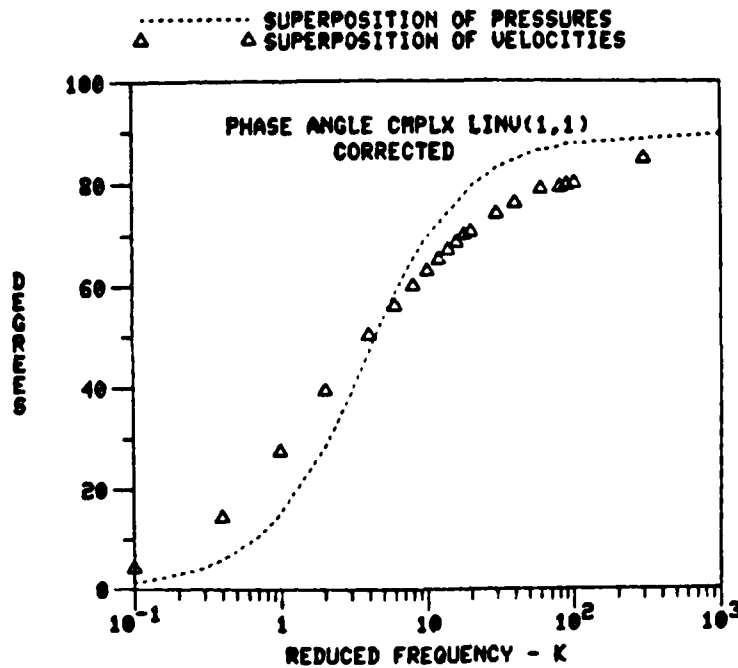
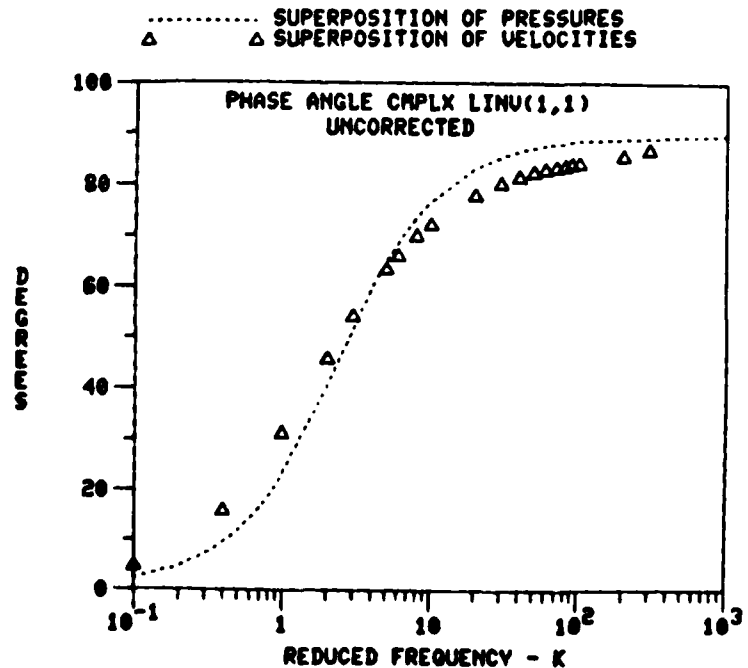


Figure 33. Phase Angle of the (1,1) Element of Inverted Complex L(K) Matrix at $\alpha = 90^\circ$ with Corrected Thrust Distribution

Figure 34. Phase Angle of the (1,1) Element of Inverted Complex L(K) Matrix at $\alpha = 90^\circ$ with Uncorrected Thrust Distribution



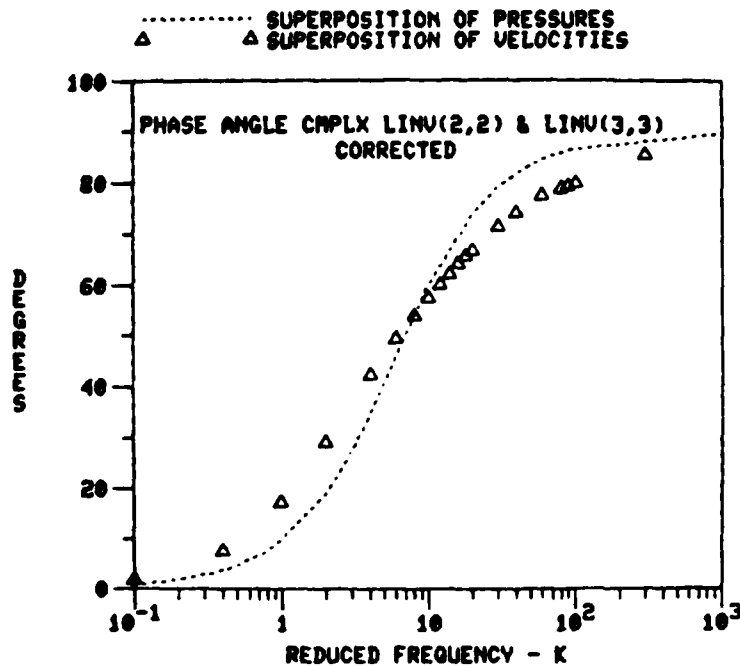
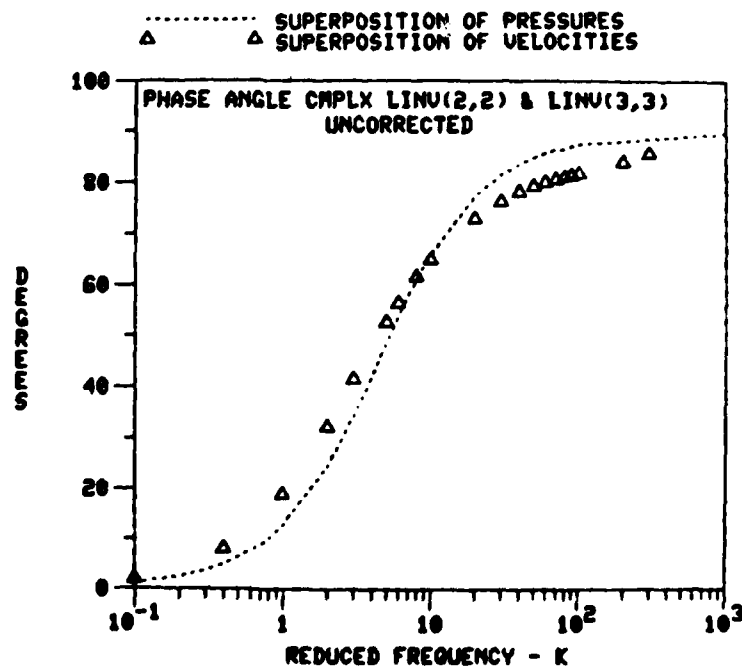


Figure 35.
Phase Angle of
the (2,2) and
(3,3) Elements of
Inverted Complex
 $L(K)$ Matrix at
 $\alpha = 90^\circ$ for
Corrected Moment
Distribution

Figure 36.
Phase Angle of
the (2,2) and
(3,3) Elements
of Inverted
Complex $L(K)$
Matrix at $\alpha =$
 90° for
Uncorrected
Moment
Distribution



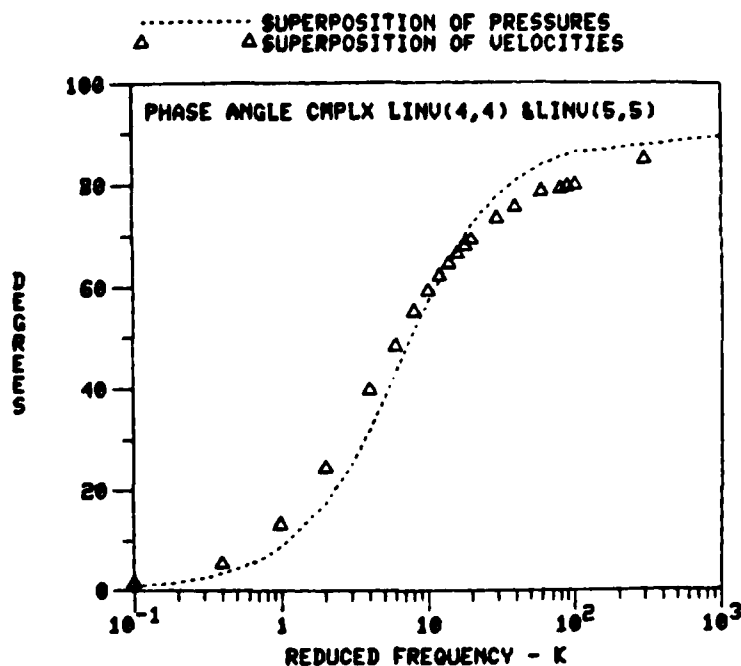
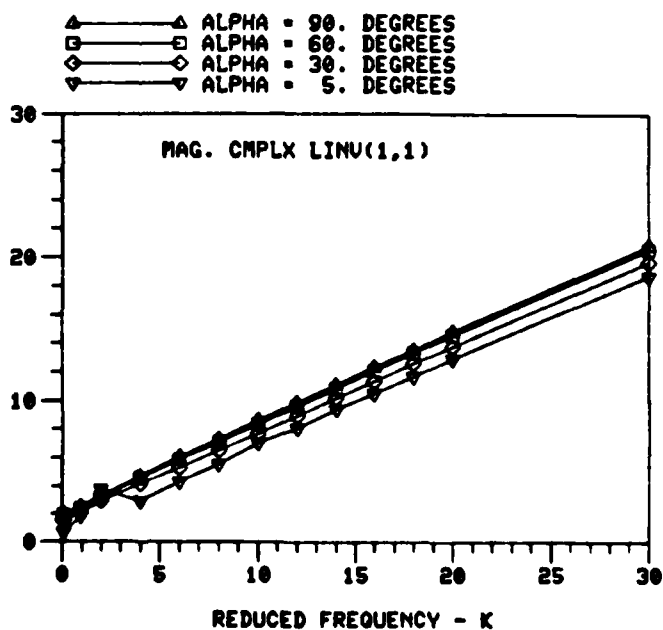


Figure 37.
Phase Angle of
the (4,4) and
(5,5) Elements
of Inverted
Complex L(K)
Matrix at $\alpha = 90^\circ$ for
Second Harmonic
Load
Distribution

Figure 38. Magnitude
of the (1,1) Element
of Inverted Complex
L(K) Matrix for α
Sweep (Corrected
Pressure)



The phase angle comparison for the uncorrected thrust distribution is depicted in figure 34. The uncorrected S.P. and S.V. phase angles have a better correlation than the phase angles for the corrected pressure distributions. A comparison of figures 33 and 35 with 34 and 36 shows that the S.P. phase angles for the uncorrected pressure distribution are almost identical to those of the corrected distribution, except that the former are shifted to the left. That is to say, that for a given K the uncorrected S.P. phase angles are slightly larger than their corresponding corrected phase angles. This is to be expected, because the S.P. real term is independent of pressure distribution for $\alpha = 90^\circ$ and the S.P. uncorrected apparent mass is larger than the corresponding uncorrected terms. Thus, the only difference between the S.P. phase angles for the correct and uncorrected distribution is due to the different apparent mass terms. For the S.V. method, there is a definite change in the slope and magnitude of the phase angles calculated for the corrected and uncorrected pressure distributions. This would imply that the real and imaginary parts of the S.V. inverted complex L-matrix are dependent on the radial load distribution. Finally, the closest agreement for the S.P. and S.V. phase angles are shown in figure 37 for the second-harmonic pressure distribution.

Up to this point, the unsteady results presented are for the axial flow case. A major part of this research is to determine the comparison of the complex interved L-matrix

obtained by S.P. and S.V. as the angle of attack varies from $\alpha = 90^\circ$ to $\alpha = 0^\circ$. The inverted complex L-matrix obtained by the S.P. method consists of the superposition of the inverted steady L-matrix and the apparent mass matrix. The apparent mass matrix, as given in Table 4, is a diagonal matrix that is independent of the rotor angle-of-attack and is the complex part of the inverted matrix. The real part is the inverted steady L-matrix, which varies with angle of attack. This variation was discussed in the steady results. The inverted complex matrix obtained by the S.V. method is found to vary with angle-of-attack. The inverted 5 X 5 complex L-matrix has the following nonzero elements; (1,1), (3,1), (5,1), (2,2), (4,2), (1,3), (3,3), (5,3), (2,4), (4,4), (1,5), (3,5) and (5,5). It would be quite lengthy to discuss the magnitude, phase angle, imaginary component, and real component of each of the 13 elements of the complex inverted L-matrix. Consequently, only the first column, elements (1,1), (3,1), and (5,1) and their variation with alpha will be discussed in detail. However, data and figures for the other elements are presented as supplemental data in Appendix 7.4. Furthermore, most of the comments about the elements in the first column also pertain to the figures in Appendix 7.4. The following data is based on a corrected pressure distribution unless otherwise noted.

The magnitudes as calculated by S.V. method are presented in figures 38 - 40. The magnitude of the (1,1) element is shown to vary slightly with angle-of-attack in figure 38.

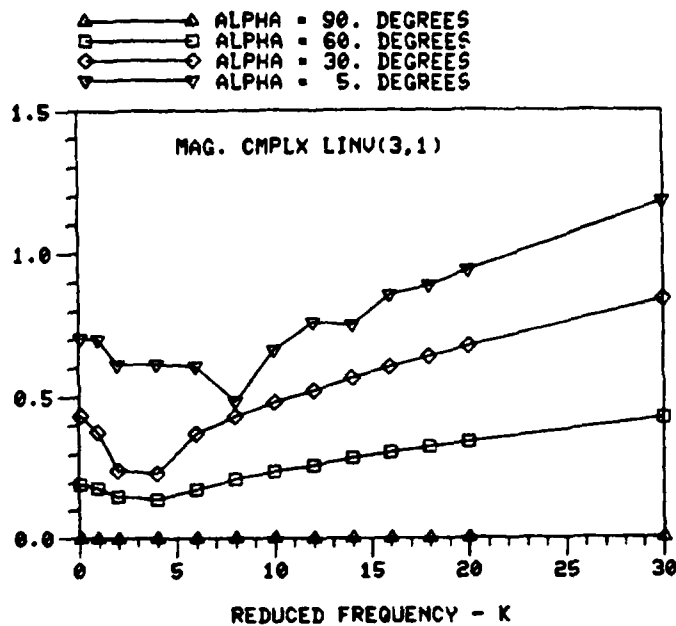
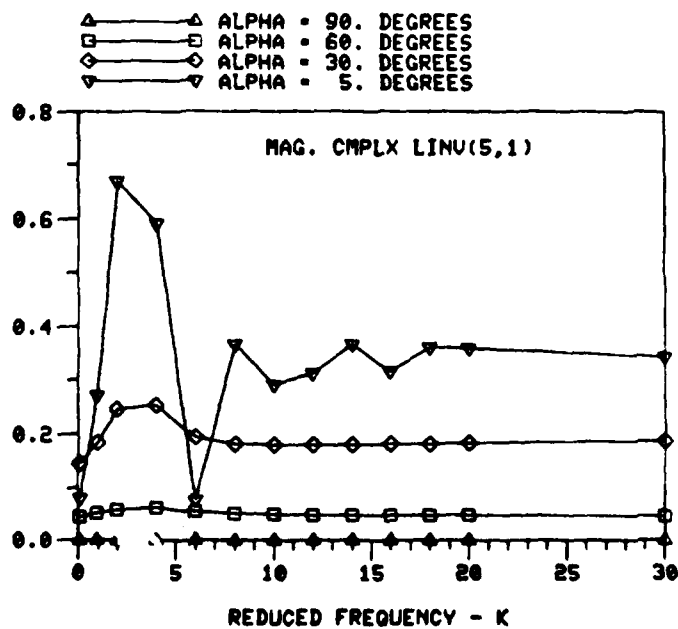


Figure 39.
Magnitude of the
(3,1) Element of
Inverted Complex
L(K) Matrix for
 α Sweep (Corrected
Pressure)

Figure 40.
Magnitude of the
(5,1) Element of
Inverted Complex
L(K) Matrix for
 α Sweep (Corrected
Pressure)



The magnitude decreases by a constant value for all values of K as α decreases. We also note that, at $K = 0$, the magnitude of the (1,1) element approaches zero as α approaches zero. This agrees with the steady inverted complex L-matrix of the S.P. method, shown in figure 15. We have previously discussed the comparison of the S.P. and S.V. for the (1,1) element at $\alpha = 90^\circ$. As α varies, the S.P. varies as the inverted, steady (1,1) element with the addition of the apparent mass effects. Figure 39 displays the magnitude of the (3,1) element as computed by the S.V. method for the α sweep. At $\alpha = 90^\circ$, both the S.P. and S.V. methods predict a magnitude of zero. As angle-of-attack is varied, the magnitude of this off-diagonal element of the S.P. complex, inverted L-matrix possesses only a real part, which is the inverted steady L term. Thus, at $K = 0$, the magnitudes predicted by the S.P. and S.V. are the same. As K increases, the magnitude of the S.P. remains constant and is a horizontal line drawn from the $K = 0$ point. (Note this line is not shown on figure 39 and 40 for sake of clarity). Interestingly, there seems to be a decrease in the magnitude of the (3,1) term for S.V. at $K \approx 5$. Also, the magnitude is seen to have a linear increase for all α as K increased beyond 10. This increase in magnitude implies that either the real or imaginary or possibly both parts are increasing. Figure 40 depicts the magnitude of the (5,1) term for various values of α . The S.V. magnitude at $\alpha = 90^\circ$, 60° , and 30° agrees well with the S.P. magnitude ($K = 0$). It is noted that the S.V. magnitude for

$\alpha = 5^\circ$ displays numerous peaks. Originally, the computer runs were made at $\alpha = 1^\circ$, however, the peaks were more prominent and pronounced. It is felt that the peaks are due to the rapid azimuthal variation in the complex induced velocity, combined with the numerical difficulty of integrating the oscillating streamwise functions. To verify this assumption, the complex induced velocities are plotted along the longitudinal and lateral rotor axis, figures 41 and 42. Both the unsteady induced velocities and the steady induced velocities are shown in the figures. A comparison of figures 41 and 42 shows that the unsteady induced velocities have oscillating lateral and longitudinal induced-velocity distributions. This oscillatory, induced-velocity field (combined with rapid azimuthal changes), increases the difficulty of the numerical integration of the complex L-matrix. It is also interesting to compare the magnitudes of the (1,1), (3,1) and (5,1) terms at $K = 30$. It is obvious that the relative size of the (1,1) term is larger than the (3,1) which is in turn, larger than the (5,1) term.

The effects of the α sweep on the phase angles of the first column of the inverted complex L-matrix are presented in the figures 43 - 45. Figure 43 shows the phase angle variations of the (1,1) term. The comparison of the phase angles obtained by the S.P. and S.V. methods at $\alpha = 90^\circ$ has already been discussed and is given in figure 33. As the angle-of-attack is varied, only the real part changes in the S.P. method. Therefore, the phase angles for the

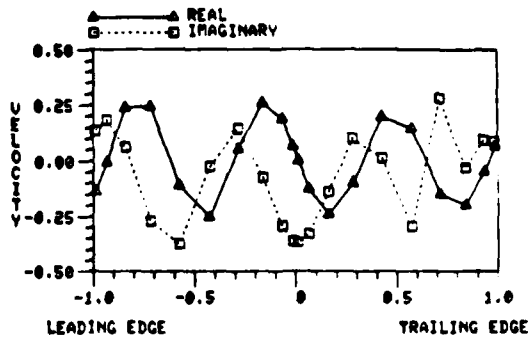


Figure 41. Complex Induced Velocity Distribution For $K = 10$, $\alpha = 1^\circ$, and Uncorrected Thrust Loading

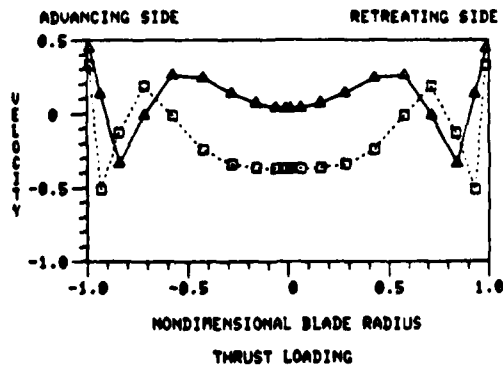
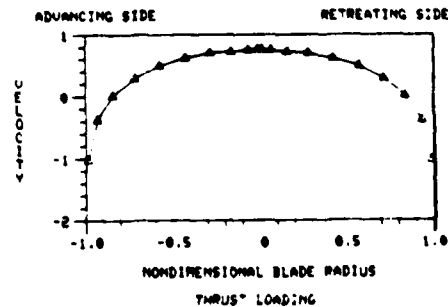
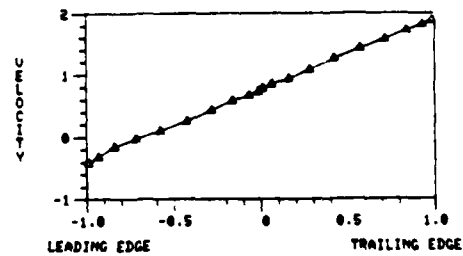


Figure 42. Steady Induced Velocity Distribution for $\alpha = 1^\circ$ and Uncorrected Thrust Loading



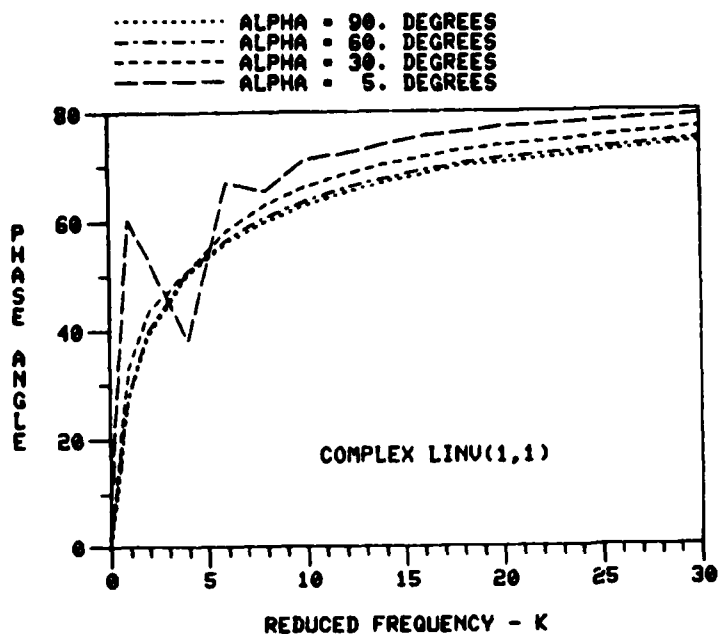
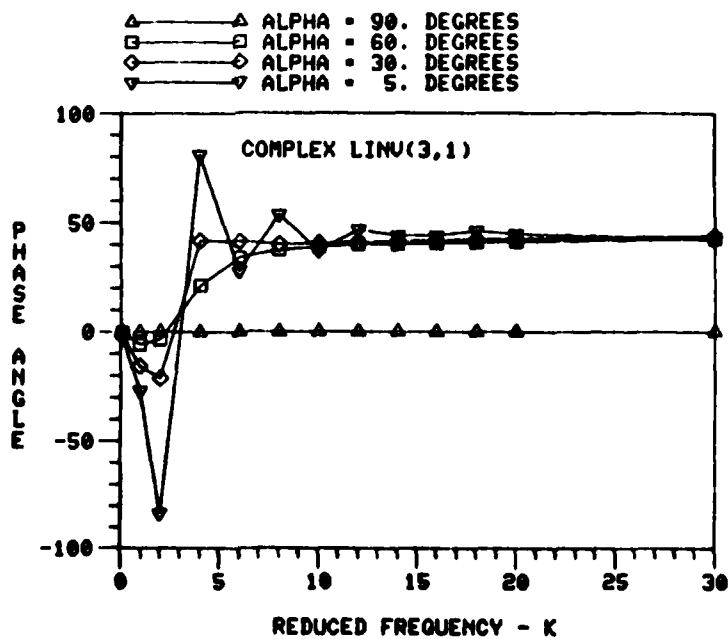


Figure 43. Phase Angle of the (1,1) Element of Inverted Complex L(K) Matrix for α Sweep (Corrected Pressure)

Figure 44. Phase Angle of the (3,1) Element of Inverted Complex L(K) Matrix for α Sweep (Corrected Pressure)



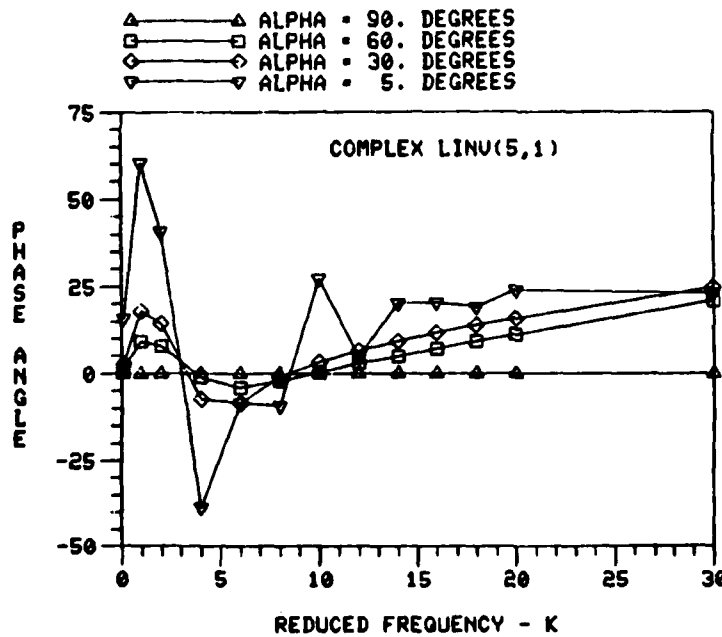
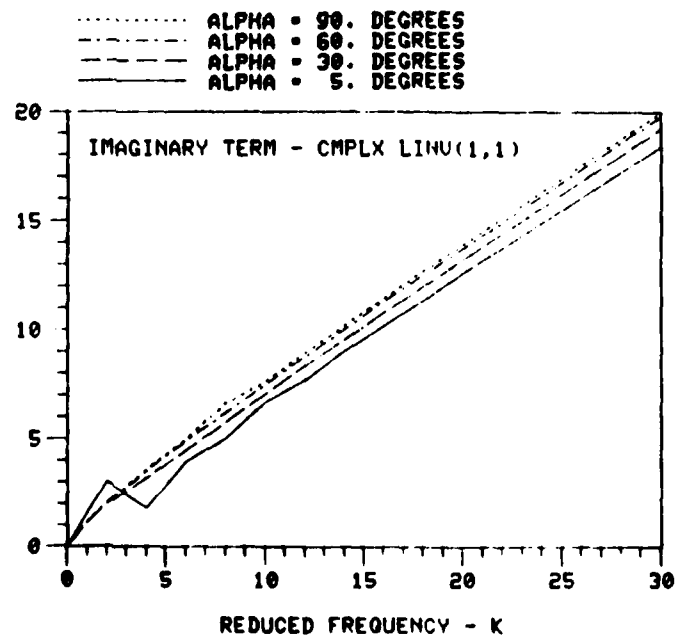


Figure 45.
Phase Angle of
the (5,1)
Element of
Inverted Complex
L(K) Matrix for
 α Sweep
(Corrected
Pressure)

Figure 46.
Imaginary Part of
the (1,1) Element
of the Inverted
Complex L(K)
Matrix for α
Sweep (Corrected
Pressure)



S.P. method are virtually independent of α . It is also seen that the S.V. phase angle of the (1,1) term increases slightly as α decreases. There is little difference between $\alpha = 90^\circ$ and $\alpha = 60^\circ$, and there is only a 5 degree difference between $\alpha = 30^\circ$ and $\alpha = 5^\circ$ at $K = 30$. The case for $\alpha = 5^\circ$ appears to have a few peaks. At $K = 30$, the phase angle appears to lie between 70 and 80 degrees for all α -values calculated. Figure 44 shows the phase angle for the (3,1) term. The phase angles for the S.P. method is zero over the complete α and K range for all the nondiagonal elements of the inverted complex L-matrix. The phase angle for S.V. is also zero for $\alpha = 90^\circ$; but, for all other values of α , the phase angle appears to approach 40° at $K = 30$. Interestingly, this is approximately 1/2 of the (1,1) phase angle at $K = 30$. The most noticeable aspect of figure 44 is that the phase angle changes sign and passes through zero at a reduced frequency of 4. This would indicate that either the real or imaginary part of the (3,1) term changes sign in this region. The phase angle of the (5,1) term is presented in figure 45. This figure shows that the (5,1) phase angle also varies with K and α . At $\alpha = 90$, the phase angle is zero which again implies that the S.P. and S.V. method give the same results at $\alpha = 90$. However, for all other α , the S.V. method predicts a phase angle which changes sign twice and passes through zero at both $K = 4$ and $K = 8$. The (5,1) phase angle is 20 degrees at $K = 30$ and appears to be independent of α . The value of 20 degrees is about 1/2 of the (3,1) phase angle and 1/4 the (1,1) phase angle at $K = 30$.

The imaginary parts of the first column of the inverted complex L-matrix are presented in figures 46 - 48. Figure 46 depicts the S.V. complex part of the (1,1) term for the α sweep of 90 to 5 degrees. It should be noted that the $\alpha = 90^\circ$ curve can be compared directly to figure 22 in order to determine the difference between the complex parts as predicted by the S.P. and S.V. methods. In accordance with the assumptions of the S.P. method, the (1,1) term is independent of α ; and the (3,1) and (5,1) terms have no imaginary part. However, from figure 46, it is noted that the S.V. imaginary term shows a slight decrease in value for a decreasing angle-of-attack. We assume that the imaginary part is determined by the apparent mass times the reduced frequency. Thus, the apparent mass for M(1,1) is slightly dependent on rotor angle-of-attack. We also note that for $\alpha = 5^\circ$ there are several small peaks, which are attributed to the rapid change of the induced velocities at low angle-of-attack. The imaginary part of the (3,1) term is given in figure 47. The (3,1) term is observed to change sign and pass through zero at approximately $K = 4$. For the imaginary part to be equal to zero means either K is zero or the apparent mass is zero. Thus, the (3,1) apparent mass is equal to zero at $K = 4$ for all angles-of-attack. As the angle-of-attack decreases, the imaginary part is observed to increase. The slope of the imaginary curves at $K = 30$ is small, which implies that the apparent mass term is small. Figure 48 shows that the imaginary (5,1) term changes sign twice and passes through zero at $K = 4$ and $K = 8$. This means

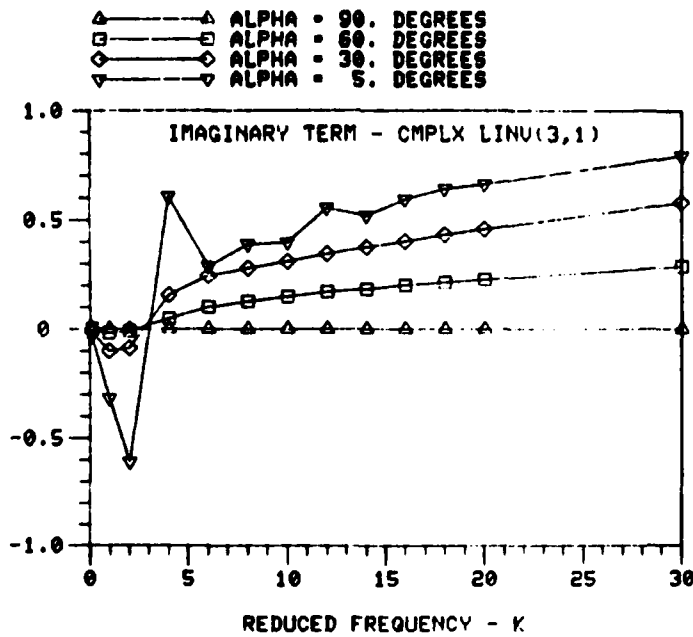
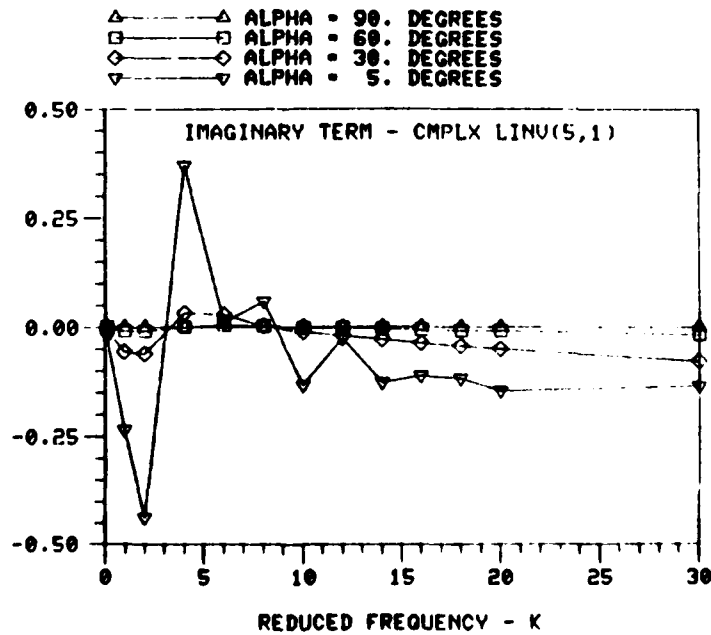


Figure 47.
Imaginary Part
of the (3,1)
Element of the
Inverted Complex
L(K) Matrix for
 α Sweep
(Corrected
Pressure)

Figure 48.
Imaginary Part of
(5,1) Element of
the Inverted
Complex L(K)
Matrix for α
Sweep (Corrected
Pressure)



that, at $K = 4$ and $K = 8$, the apparent mass $M(5,1)$ is zero and is independent of α . We also note that, as α decreases from 90° , the imaginary terms increase. From the slope of the curves at $K = 30$, the apparent mass term, $M(5,1)$ must be fairly small.

The real part of the inverted complex L-matrix as determined by the S.P. method is just the inverted steady L-matrix. In contrast, the real part of the S.V. inverted complex matrix is obtained by inverting the unsteady L-matrix that is obtained by integration of the complex induced velocities on the rotor disc. Figures 49 - 51 depict the deviation between the real portion of the inverted complex matrices (S.P. and S.V.) for various angles-of-attack. Figure 49 shows the deviation for the (1,1) term, and the deviation is shown to increase for increasing K . This means that the real part of the S.V. (1,1) element is dependent on K , whereas for the S.P. method, it is assumed to be independent. The (1,1) deviation is shown to decrease as α is decreased from 90° . The fact that the steady, inverted (1,1) term varies from a maximum of 2.0 at $\alpha = 90^\circ$ to zero at $\alpha = 0$, implies that even though the relative size of the deviation decreases with α , the percent error is increasing. The deviation of the (3,1) term is shown in figure 50. It changes sign and crosses through zero as K is increased. As α decreases from 90° , the relative deviation at $K = 30$ increases. Figure 51 depicts the deviation of the real part of element (5,1). For $\alpha > 30^\circ$, the (5,1) deviation

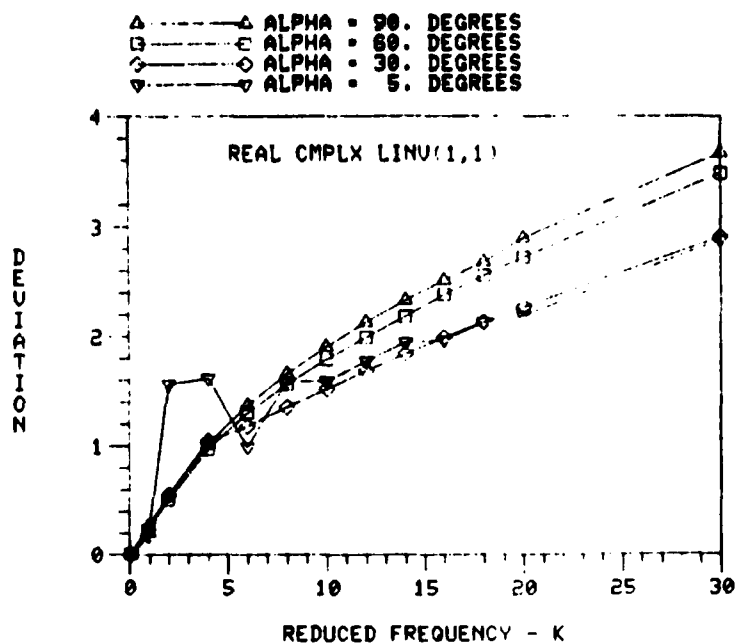
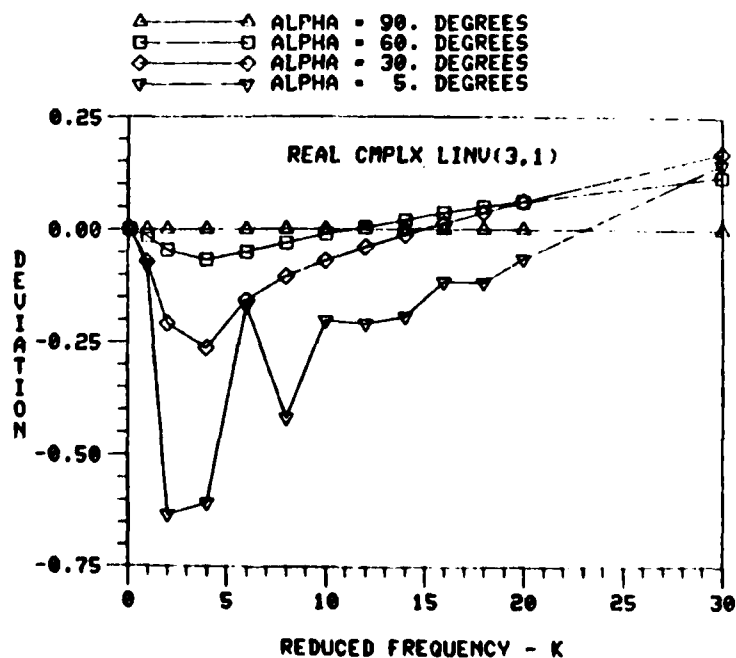


Figure 49.
Deviation of the
Real Part of the
(1,1) Element of
the Inverted
Complex L(K)
Matrix as
Calculated by
S.P. and S.V. for
 α Sweep (Corrected
Pressure)

Figure 50.
Deviation of the
Real Part of the
(3,1) Element of
the Inverted
Complex L(K)
Matrix as
Calculated by
S.P. and S.V.
for α Sweep
(Corrected
Pressure)



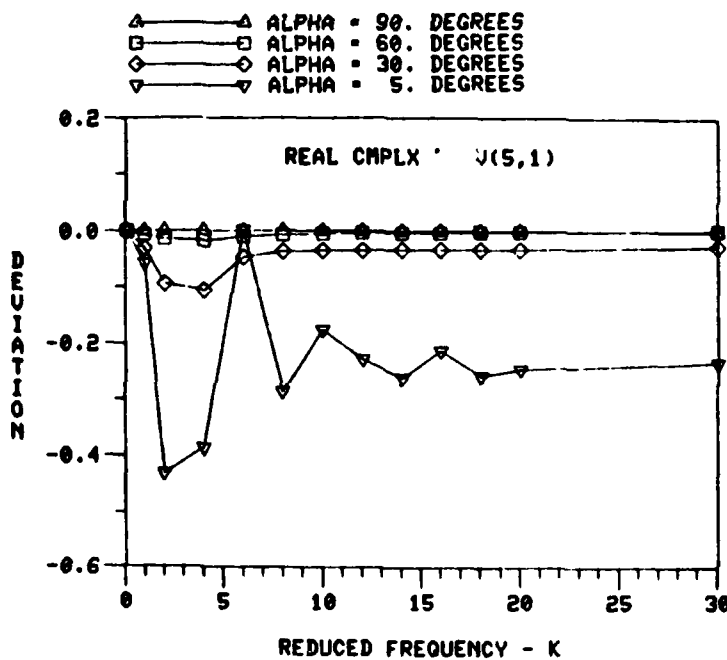
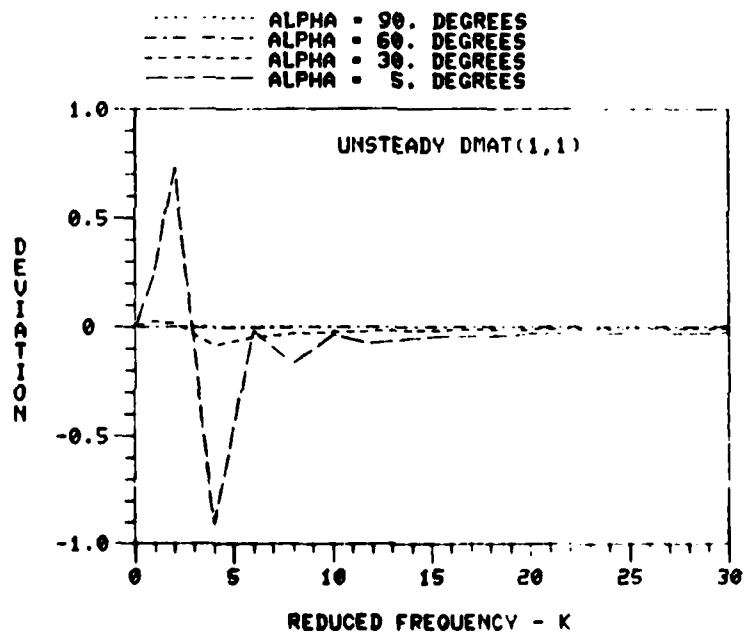


Figure 51.
Deviation of the
Real Part of the
(5,1) Element of
the Inverted
Complex $L(K)$
Matrix as
Calculated by
S.P. and S.V.
for α Sweep
(Corrected
Pressure)

Figure 52.
Deviation of the
Imaginary Part
of Element (1,1)
for the S.V. 5X5
and 3X3 Complex
Inverted $L(K)$
Matrix for α
Sweep (Corrected
Pressure
Distribution)



is small and almost independent of reduced frequency. The largest deviation for the (5,1) term is for $\alpha = 5$ and the deviation appears to be constant for $K > 18$.

For the case of axial flight, $\alpha = 90^\circ$, the inverted complex L-matrix obtained by either the S.P. or the S.V. method is diagonal. Consequently, there was no difference between the inverted 5 X 5 and 3 X 3 matrices. Figures 52 and 53 compare the imaginary parts of the (1,1) and (3,1) elements of the 5 X 5 and 3 X 3 S.V. inverted complex L-matrix. The figures show that there is little difference between imaginary parts for the 3 X 3 or 5 X 5 matrices. The imaginary part of the complex L-matrix is large at $K = 30$, yet the difference is less than 0.1. For $K < 10$, there are some more spurious peaks with the largest being for $\alpha = 5^\circ$. Even with these peaks, the deviations are relatively small.

In reference 71, an analytic 3 X 3 L-matrix and apparent mass matrix was suggested, based on preliminary results of this research. These matrices are presented in Table 5. The rationale for the development of these elements will be addressed in Section 6. However, it is important to note that the first column of the M-matrix is for a corrected pressure distribution, while the second and third columns are for uncorrected pressure distributions. We will now discuss the results of using the analytical 3 X 3 M-matrix and L-matrix in the S.P. formulation and the subsequent comparison to the 3 X 3 S.V. matrices. Figure 54 compares the relative magnitudes of the S.V. (3,1) and (1,3) ratios

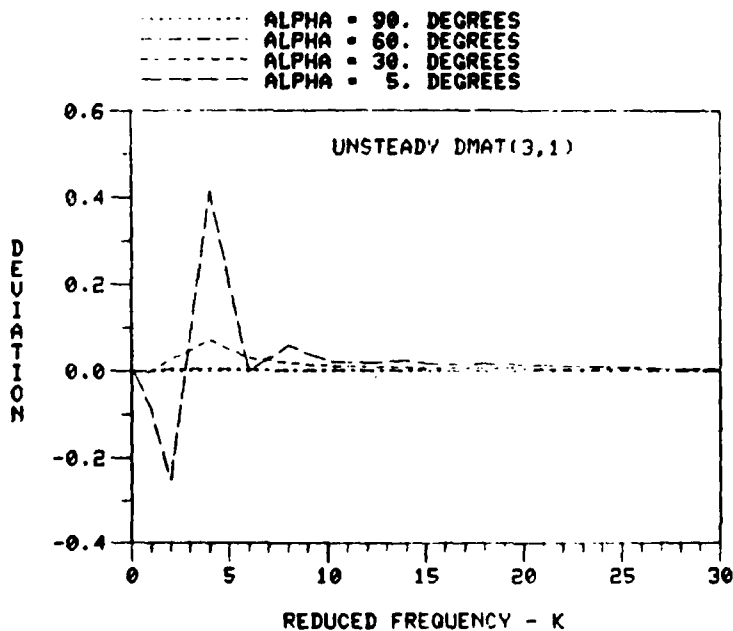


Figure 53.
Deviation of the
Imaginary Part
of Element (3,1)
for the S.V. 5X5
and 3X3 Complex
Inverted L(K)
Matrix for α
Sweep (Corrected
Pressure
Distribution)

Figure 54. Relative
Magnitude of the
Off-Diagonal Terms
of the 3X3 Inverted
Complex L(K) Matrix
at $\alpha = 30^\circ$

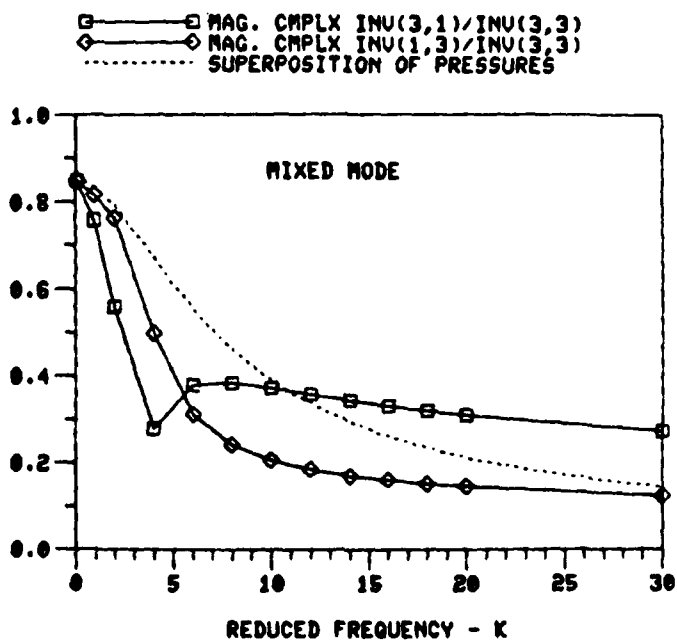


TABLE 5

Analytic Forms of L-Matrix
and M - Matrix

$$[L] = \frac{1}{V} \begin{bmatrix} \frac{1}{2} & 0 & \frac{15}{64} \sqrt{\frac{1-\sin\alpha}{1+\sin\alpha}} \\ 0 & \frac{-4}{1+\sin\alpha} & 0 \\ \frac{15}{64} \sqrt{\frac{1-\sin\alpha}{1+\sin\alpha}} & 0 & \frac{-4\sin\alpha}{1+\sin\alpha} \end{bmatrix}$$

$$[M] = \begin{bmatrix} \frac{128}{75} & 0 & 0 \\ 0 & \frac{-16}{45} & 0 \\ 0 & 0 & \frac{-16}{45} \end{bmatrix}$$

to the (3,3) element for $\alpha = 30^\circ$. The ratio of magnitudes is also presented for the S.P. theory in figure 54. This ratio gives an absolute measure of the magnitude of the off-diagonal terms in comparison with the diagonal elements. The relative magnitude of the off-diagonal terms is shown to decrease for increasing K. This not only tells us of the importance of the off-diagonal terms but is also a direct comparison of the S.P. method, for which off-diagonals are assumed to be real and have no imaginary part; with the S.V. method, the elements which have both real and imaginary terms. Figure 54 shows qualitative agreement between the two theories. It is interesting to note that the S.V. calculations are not symmetric as are those of S.P. Figures 55 and 56 show the phase angles of the ratio of the off-diagonal to the (3,3) element as calculated by S.P. and S.V. For $\alpha = 90^\circ$, both figures show good correlation of the phase angles. However, for $\alpha = 30^\circ$, the correlation is poor with the general shape of the curves being similar but with a discrepancy in the actual values. Lastly, it is interesting to note the phase angles predicted by the S.V. method are not symmetric. In fact, the phase angle in figure 56 changes shape radically in the range $2 < K < 6$.

5.2 PRESCRIBED-WAKE RESULTS

The results of the 3 X 3 Prescribed-Wake (PW) L-matrix are presented in figures 57 - 59. The rotor characteristics are the same as those tested in references (54 - 57). The rotor moves with respect to still air at 20 ft/sec and the

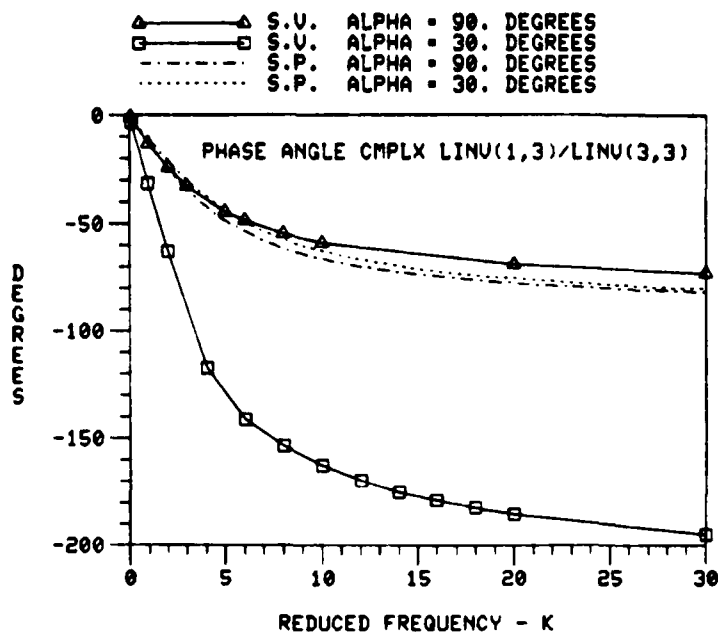
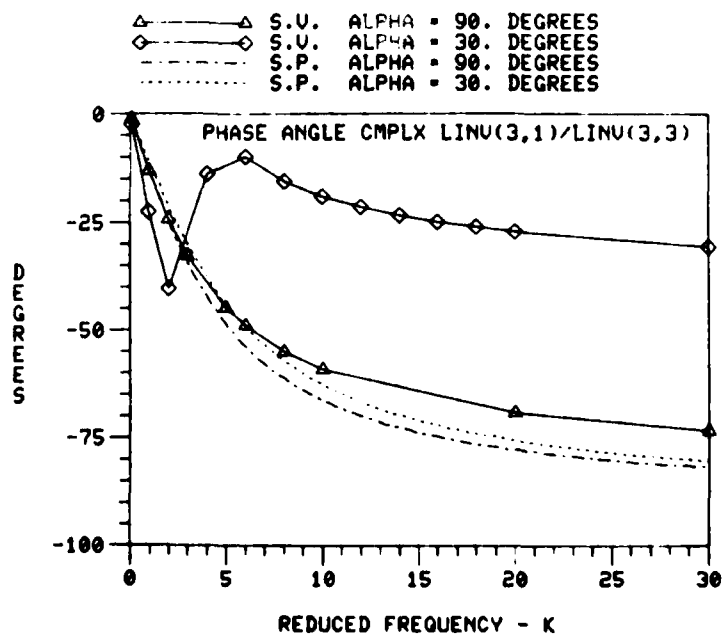


Figure 56. Phase Angle of Complex (3,1)/(3,3) for Analytical L and M Matrices



tip speed is 216 ft/sec. The L-matrix is calculated at the following angles-of-attack: 90° , 60° , and 30° . However, the effective angle of attack is a function of the steady rotor thrust and inflow conditions. The effective angle-of-attack is given in reference (71) as

$$\alpha^* = \tan^{-1} \frac{\bar{\lambda} + \bar{v}}{\mu} \quad (119)$$

For a helicopter in forward flight, α^* is generally larger than 6 degrees. The effective angle of attack was used in plotting the PW L-matrix of figures 57 - 59. In these figures, the 30° and 60° cases are shifted to the right because the

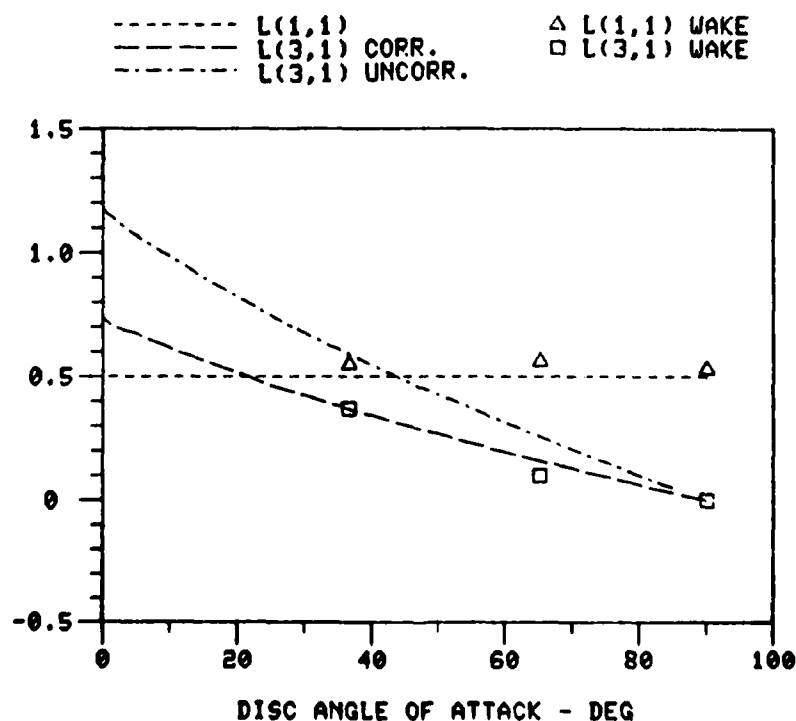


Figure 57. First Column of the Prescribed-Wake L-Matrix

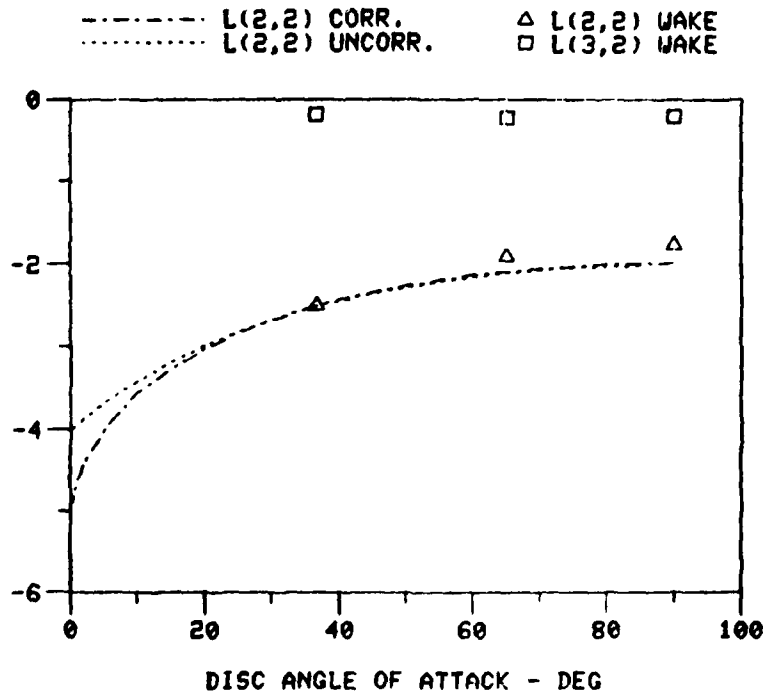


Figure 58. Second Column of the Prescribed-Wake L-Matrix

effective angle-of-attack of thrusting rotor is larger than the geometric angle-of-attack.

The L-matrices generated in this section require 4 prescribed wake calculations for each α . First, a baseline case is run for a typical control setting. Second, the controls (θ_o , θ_s , θ_c) are varied sequentially. For each variation, the change in v_o , v_s , v_c , C_T , C_L , and C_M is noted. A linear inversion then gives L, as described earlier.

The first column of the PW L-matrix is presented in figure 57. In this figure the steady Actuator Disc (AD) L-matrix is presented as dotted/dashed lines. The (AD) L-matrix is presented for both the corrected and uncorrected

thrust distributions. The PW (1,1) term is shown to be relatively constant for all α , and shows excellent agreement with the AD (1,1) term (6% error). It should be remembered that the AD (1,1) term is independent of either thrust distribution or rotor angle-of-attack. This excellent degree of correlation is amazing, when it is remembered that the PW integration of induced velocities and air loads is crude with respect to: assumed constants, assumed lift, and constant induced velocity for the rectangular integration scheme in the radial direction. The PW L(3,1) term also shows good correlation with the corrected AD values. The shift in angle-of-attack, α^* , is seen to play an important role in aiding the correlation.

Figure 58 is the second column of the prescribed-wake L-matrix, which is the induced flow due to a rolling moment. (The Actuator-Disc Theory predicts that the corrected and uncorrected (2,2) terms should be equal for $\alpha > 25^\circ$). The PW L(2,2) term shows excellent agreement in this range. The third column of the PW L-matrix, induced flow due to a pitching moment C_M , is presented in figure 59. The (1,3) and (3,3) terms also show excellent agreement with both the magnitudes and slopes of their respective actuator disc values. In the range of the prescribed-wake data, the corrected and uncorrected moment distributions have little effect on the AD L(1,3) and L(3,3) terms. It appears that the PW L(3,3) is approaching zero for the case of edgewise

flight. The PW $L(2,1)$ and $L(1,2)$ terms are less than 0.05 for all cases, and are essentially zero as predicted by the AD theory.

Most of the dynamic-inflow theories to date, including the Actuator-Disc Theory developed during this research, predict that the $(3,2)$ and $(2,3)$ terms of the L-matrix are zero for all α . The $(3,2)$ term is v_c , cosine or fore-to-aft induced velocity, due to C_L (rolling moment); and the $(2,3)$ term is v_s , sine component of induced velocity, due to C_M (a pitching moment). Nonzero values or cross-coupling terms

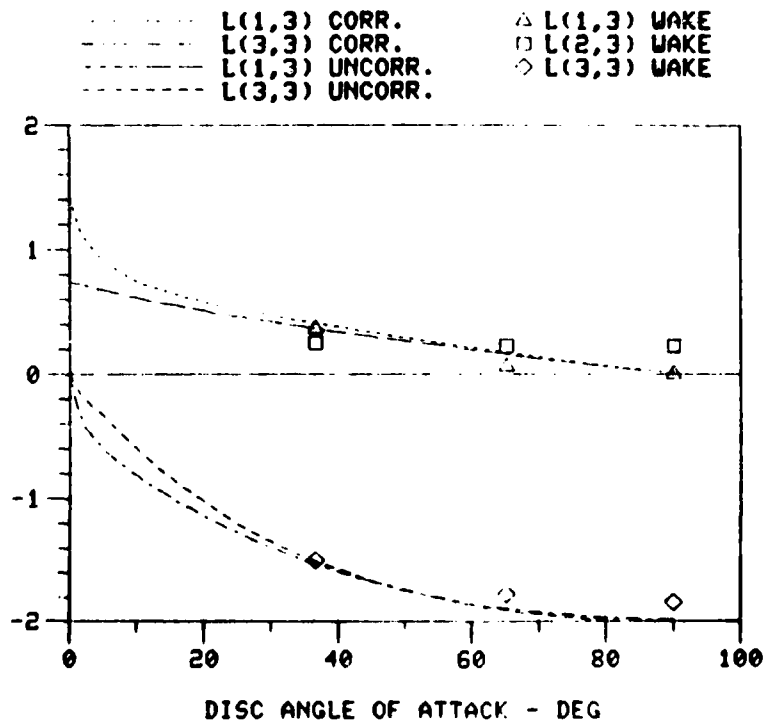


Figure 59. Third Column of the Prescribed-Wake L-Matrix

are predicted by the prescribed-wake theory, and are shown in figures 58 and 59. Both terms appear to be constant with respect to α . It is interesting to note that $L(3,2)$ is approximately -0.2 and that $L(2,3)$ is 0.2. Thus, $L(2,3) = -L(3,2)$ for the prescribed-wake L-matrix. This is qualitatively similar to the empirical model, reference (60), in which $L_{23} = -L_{32}$ is found at low α .

The natural explanation of these coupling terms is that they represent the induced velocity caused by the rotor - wake rotation. Bramwell (72) states that the rotation or swirl velocity is due to the bound circulation about the blades and the circulation due to the spiral vortex lines forming the slipstream. Bramwell relates the swirl velocity to disc loading and shows that the velocity caused by the wake rotation is small when compared to the other induced velocity terms. The PW $L(3,2)$ and $L(2,3)$ terms are small with respect to the other numbers in the column as seen in figures 58 and 59. Because the swirl velocity is a function of the rotor disc loading, it is felt that the PW $L(3,2)$ and $L(2,3)$ terms will vary slightly with thrust. The value of swirl angle required to produce these terms is about 6° , which is the same order-of-magnitude as the swirl angle for this case.

6. CONCLUSIONS AND RECOMMENDATIONS

The inflow models used in this research consist of:

- (1) Steady Actuator Disc-Corrected and Uncorrected radial load distribution.
- (2) Unsteady Actuator Disc-Superposition of Pressure (S.P.) for both the corrected and uncorrected radial load distributions.
- (3) Unsteady Actuator Disc-Superposition of Velocities (S.V.) for both the corrected and uncorrected radial load distributions.
- (4) Unsteady Actuator Disc-Analytical 3X3 L and M Matrices.
- (5) Prescribed-Wake Model

The induced-velocity distribution for each inflow model is numerically integrated over the rotor disc for three independent pressure distributions to obtain the L-matrix. Models 1 - 3 provide both a standard 3X3 nonuniform inflow L-matrix, and an extended 5X5 L-matrix that includes second-harmonic velocities and loadings. The fourth model represents an analytical formulation of induced flow based on the results of models 1 - 3. The fifth model includes wake contraction, wake rotation, and finite number of blades. Thus, it serves as a measure of accuracy for the simpler, actuator-disc models.

6.1 CONCLUSIONS CONCERNING THE STEADY, ACTUATOR-DISC MODEL

Some of the more important conclusions of the steady actuator-disc research are:

(1) The steady, actuator-disc theory for dynamic inflow is based on the Mangler-Squire Theory. The induced velocities calculated by the Mangler-Squire Theory are shown to agree with measured results of reference (12).

(2) In axial flow (e.g. hover), the gains (elements of the 3X3 L-matrix) are identical to those obtained from simple momentum theory, and are independent of the radial lift distribution.

(3) The fore-to-aft induced velocity gradient ($L(3,1)$) in dynamic inflow (or K in Glauert Theory) varies with α in the same manner predicted by the wake skew angle formula of simple vortex theory.

(4) Closed form results are obtained for all elements of the L-matrix at $\alpha = 90^\circ$ (axial flow), for all elements of the L-matrix at $\alpha = 0^\circ$ (edgewise flow), and for the first column of the L-matrix at all angles-of-incidence, α .

(5) For a thrust loading and edgewise flow, the cosine harmonics of induced velocity, $L(3,1)$ and $L(5,1)$, are large with respect to the average value $L(1,1)$. For the other loading conditions, at $\alpha = 0^\circ$, all the higher harmonic elements of the L-matrix are small save for $L(5,5)$.

(6) Numerical results for the elements of L at angles-of-incidence from 0° to 90° show that they are not strongly dependent upon lift distribution for $10^\circ < \alpha < 90^\circ$, although significant dependence does occur for $\alpha < 10^\circ$.

(7) A 3-degree-of-freedom dynamic-inflow model is probably adequate for rotary wing dynamics.

(8) Both the 5X5 and 3X3 steady L-matrices are well behaved and invertible as α varies from 90° to 0° .

(9) The upper 3X3 portions of the inverted, steady 5X5 and 3X3 L-matrices are in agreement for typical values of α .

6.2 CONCLUSIONS CONCERNING THE UNSTEADY, ACTUATOR-DISC MODEL

In the unsteady, actuator-disc research, the inverted complex L-matrices of the S.P. and S.V. methods are compared. The following are the conclusions from this phase of the research:

(1) The apparent mass terms (the M-matrix) for the uncorrected pressure distributions are identical to the apparent mass terms of an impermeable disc, but these values vary significantly with lift distribution. The uncorrected terms are always larger than the corrected values.

(2) The apparent mass terms are more sensitive to the lift distribution than are the corresponding terms in the L-matrix.

(3) The apparent mass terms (for either corrected or uncorrected distributions) decrease with increasing harmonics of induced velocity.

(4) The apparent mass terms of the S.V. method approach those of the S.P. method at high reduced frequencies (K). However, for small K, the S.V. and S.P. apparent mass terms are considerably different.

(5) For $\alpha \neq 90^\circ$ and $K > 0$, the S.V. method predicts imaginary terms for some of the off-diagonal elements while

the S.P. method does not. However, these are small with respect to the diagonal terms.

(6) The real part of the complex, inverted L matrix is constant with K for the S.P. method, but varies with both α and K for the S.V. method. This difference between the methods is largest at high values of K, where the imaginary part is dominant and the real terms are negligible.

6.3 CONCLUSIONS CONCERNING THE PRESCRIBED-WAKE MODEL

The conclusions of the prescribed-wake program are:

(1) Generally, a given rotor control perturbation, (θ) will result in a larger perturbation in C_T than in C_L or C_M .

(2) The prescribed-wake L-matrix agrees favorably with the L-matrix from the actuator-disc model, provided that the V and α^* parameters are chosen based on momentum considerations.

(3) The prescribed-wake L-matrix has antisymmetric or cross coupling terms, $L(3,2)$ and $L(2,3)$, which are constant with α . These are not predicted by the Actuator-Disc Theory. These are due to the wake rotation associated with lifting rotor. For realistic values of rotor power, however, these are only about 10 percent as large as the diagonal terms.

6.4 COMMENTS CONCERNING THE ANALYTICAL MODEL

The analytical model is given in tables 3 and 4. The first column represents the closed form results of equation for a corrected thrust distribution. The uncorrected thrust distribution is unrealistic of a lifting rotor. The second and third columns are for uncorrected roll and pitching

moment distributions. There are several reasons for this choice in the second and third columns:

(1) Either the corrected or uncorrected moment-distribution of figure 7.2.2 would be reasonable for the first-harmonic variation of lift.

(2) Figures 11 - 12 show that the two distributions give nearly identical results (for $L(1,3)$, $L(2,2)$ and $L(3,3)$ when $\alpha > 10^\circ$).

(3) The analytic L-matrix (for α^* and v defined by equations (119) and (31)) show excellent agreement with prescribed-wake results. (For a loaded helicopter rotor $\alpha^* > 6^\circ$ generally).

(4) The uncorrected distributions follow smooth curves that appear to be identical to the α -functions in equation (117a-c).

The M-matrix is chosen for this same mixture of corrected and uncorrected load distributions. The choice of uncorrected apparent mass for $M(2,2)$ and $M(3,3)$ is also consistent with experimental results in reference (63) that show that these give realistic time constants. An eigenvalue analysis of $[L] [M]$ (the eigenvalues are the time constants) shows that there are no anomalies in the system. The induced flow has three real, stable roots for all values of α between 0° and 90° ; and L is always invertible.

6.5 RECOMMENDATIONS FOR FURTHER RESEARCH

The recommendations for future research are in two areas: 1) Unsteady, Actuator-Disc Theory and 2) Prescribed -

Wake Theory. The following work is recommended to further substantiate the present dynamic inflow model.

(1) The unsteady program should be exercised to use more than 10 radial blade stations and to decrease azimuthal increments $\alpha < 5^\circ$ to increase accuracy of L-matrix calculations for $\alpha < 10^\circ$.

(2) Windtunnel testing should be conducted to verify both the unsteady aerodynamic load distributions (C_T , C_L , C_M) and the unsteady induced velocities. This would help to physically explain the transition of the L-matrix from $\alpha = 90^\circ$ to $\alpha = 0^\circ$.

(3) Stability and dynamic response of a helicopter rotor should be calculated for 3X3 and 5X5 L-matrices as well as for both the S.P. and S.V. inverted complex L-matrices. This would provide added insight into the differences of the two methods.

The prescribed-wake computer research provided knowledge of the effects of finite blades and wake contraction on the L-matrix. This was the first successful attempt at using a Prescribed-Wake Theory to develop a dynamic inflow model. Therefore, the following ideas are offered for future study:

(1) One should develop an empirical model to estimate the wake rotation or swirl effects. The prescribed-wake program could be used to correlate the empirical model at high and low thrust levels.

(2) Thought should be given to modifying the PW program to interpolate the blade circulation at Gauss points and change the azimuthwise integration from rectangular to trapizoidal; thus, increasing the accuracy of the blade-load calculations.

(3) It would be interesting to use the PW program to develop an L-matrix for autorotational flight. It would be very useful in vortex-ring state, where momentum theory is not valid.

(4) Someone should use an unsteady, prescribed-wake model to discover the effects of wake contraction and finite number of blades on the apparent mass terms.

7. APPENDICES

APPENDIX 7.1

Actuator Disc Coordinate System

We define a Wind-Axis, Cartesian Coordinate System (x', y', z') by a rotation of the (x, y, z) Disc Coordinates through an angle α about the y/y' axis. The angle α is the disc incidence angle. We further nondimensionalize the Cartesian coordinate systems on the disc radius R . The new Disc and Wind Coordinate Systems are called X', Y', Z' and X, Y, Z respectively and are given in equation 7.1.1

$$(X, Y, Z) = \frac{1}{R} (x, y, z) \quad (7.1.1)$$

$$(X', Y', Z') = \frac{1}{R} (x', y', z')$$

Both the Wind and Disc Coordinate Systems are depicted in figure 7.1.1.

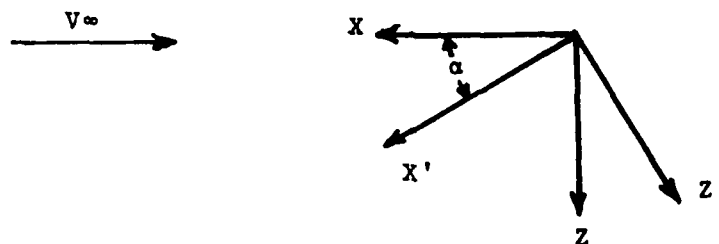


Figure 7.1.1. Wind and Disc Cartesian Coordinate Systems

The transformation between the two coordinate systems is given by

$$\begin{bmatrix} X \\ Y \\ Z \end{bmatrix} = \begin{bmatrix} \cos\alpha & 0 & -\sin\alpha \\ 0 & 1 & 0 \\ \sin\alpha & 0 & \cos\alpha \end{bmatrix} \begin{bmatrix} X' \\ Y' \\ Z' \end{bmatrix} \quad (7.1.2)$$

$$\begin{bmatrix} X' \\ Y' \\ Z' \end{bmatrix} = \begin{bmatrix} \cos\alpha & 0 & \sin\alpha \\ 0 & 1 & 0 \\ -\sin\alpha & 0 & \cos\alpha \end{bmatrix} \begin{bmatrix} X \\ Y \\ Z \end{bmatrix}$$

The Curvilinear Coordinate System (Ellipsoidal Coordinate System) v, η, ψ is defined in equation 7.1.3

$$\begin{aligned} X' &= -\sqrt{1-v^2} \sqrt{1+\eta^2} \cos\psi \\ Y' &= \sqrt{1-v^2} \sqrt{1+\eta^2} \sin\psi \\ Z' &= -v\eta \end{aligned} \quad (7.1.3)$$

The Curvilinear Coordinate System (Ellipsoidal Coordinate System) as shown in figure 7.1.2 will cover the entire three dimensional space once and only once if the restrictions given below are enforced.

$$\begin{aligned} -1 &\leq v \leq +1 \\ 0 &\leq \eta \leq \infty \\ 0 &\leq \psi \leq 2\pi \end{aligned} \quad (7.1.4)$$

In the Ellipsoidal Coordinate System, $\eta = 0$ is on the rotor disc and the coordinate v changes signs as it crosses the disc surface. The inverse transformation from the Disc Coordinate System, X', Y', Z' to the Ellipsoidal Coordinate System is given by

(7.1.5)

$$v = \frac{-1}{\sqrt{2}} (\text{sgn } Z') \sqrt{1 - \bar{K} + \sqrt{(\bar{K} - 1)^2 + 4Z'^2}}$$

$$\eta = \frac{-1}{\sqrt{2}} \sqrt{\bar{K} - 1 + \sqrt{(\bar{K} - 1)^2 + 4Z'^2}}$$

$$\text{Where } \bar{K} = X'^2 + Y'^2 + Z'^2$$

$$\psi = \tan^{-1} \left(\frac{-Y'}{X'} \right)$$

On the disc, equations 7.1.3 are used to relate the non-dimensional blade radius to the ellipsoidal coordinates.

This yields

$$r^2 = R^2 (1 - v^2) \quad (7.1.6)$$

$$\eta = 0$$

The following identity is required to perform thrust, pitch, and roll force integrations

(7.1.7)

$$\int_0^R f_L(\bar{r}) - f_U(\bar{r}) r^{-n} dr =$$

$$- \int_{-1}^0 R^{n+1} f(v) v (1-v^2)^{\frac{n-1}{2}} dv + \int_1^0 R^{n+1} f(v) v (1-v^2)^{\frac{n-1}{2}} dv =$$

$$-R^{n+1} \int_{-1}^{+1} f(v) v (1-v^2)^{\frac{n-1}{2}} dv =$$

$$\left\{ \begin{array}{l} -2Rf(v)v (1-v^2)^{\frac{n-1}{2}} dv, f(v) \text{ odd} \\ 0, f(v) \text{ even} \end{array} \right.$$

Figure 7.1.3 depicts the relationship between the rotor disc and the streamline along which we integrate to determine the induced velocity at a point on the disc.

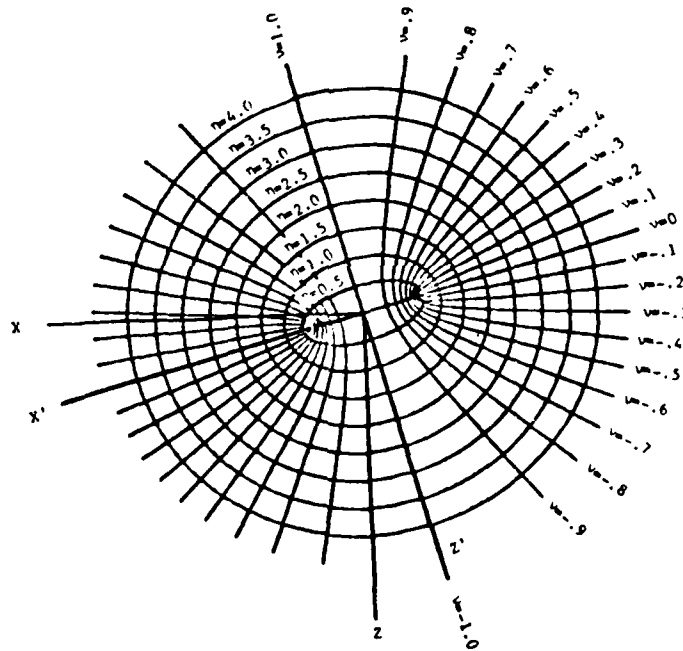
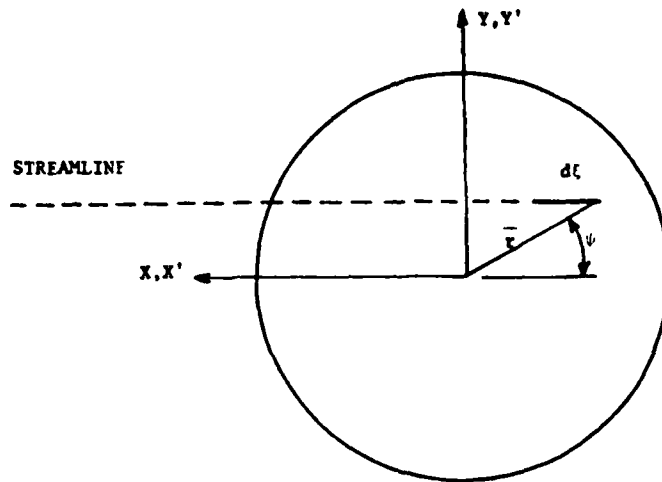
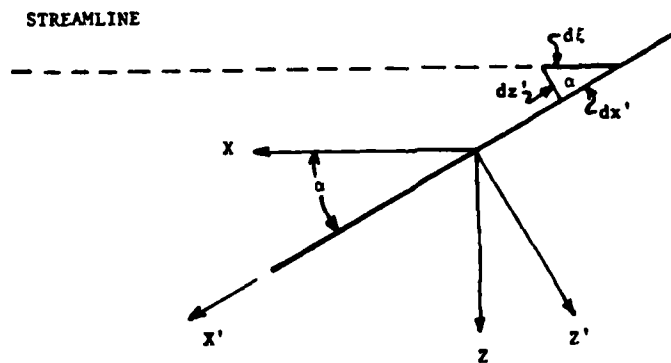


Figure 7.1.2. Curvilinear Coordinate System (Ellipsoidal Coordinate System)



a) Top View



b) Side View

Figure 7.1.3. Integration of Induced Velocity Along a Streamline in the x Direction

APPENDIX 7.2

Legendre Polynomials and Their Associated Properties

The following Legendre Polynomials of the first kind are required to evaluate the Mangler-Squire pressure distribution. The following formulas are applicable when $-1 < v < 1$

$$P_1^0(v) = v \quad (7.2.1)$$

$$P_3^0(v) = \frac{v}{2}(5v^2 - 3)$$

$$P_2^1(v) = -3v\sqrt{1-v^2}$$

$$P_4^1(v) = -\frac{5}{2}v(7v^2 - 3)\sqrt{1-v^2}$$

$$P_3^2(v) = 15v(1-v^2)$$

For the induced velocity calculations, we need to determine $\frac{d}{dv} P_n^m(v)$. The following recursive formula can be used to find the derivative of the Legendre functions of the first kind.

$$\frac{d}{dv} P_n^m(v) = \frac{nv}{v^2-1} P_n^m(v) - \frac{n+m}{v^2-1} P_{n-1}^m(v) \quad (7.2.2)$$

To determine the derivative of the polynomials given in equation (7.2.1) using equation (7.2.2), we require the use of the following polynomials.

$$P_0^0(v) = 1 \quad (7.2.3)$$

$$P_2^0(v) = \frac{1}{2}(3v^2 - 1)$$

$$P_1^1(v) = -\sqrt{1-v^2}$$

$$P_3^1(v) = -\frac{3}{2}(5v^2-1)\sqrt{1-v^2}$$

$$P_2^2(v) = 3(1-v^2)$$

The Legendre Polynomials of the first kind have the following properties of orthogonality and normalization.

$$\text{Orthogonality } \int_0^1 P_n^m(v) P_{n'}^m(v) dv = 0 \text{ for } n \neq n' \quad (7.2.4)$$

$$\text{Normalization } \int_{-1}^1 [P_n^m(v)]^2 dv = \frac{2}{2n+1} \cdot \frac{(n+m)!}{(n-m)!} \quad (7.2.5)$$

Legendre function of the second kind for Z outside the segment $(-1, +1)$ can be expressed in general form

$$Q_0(Z) = \frac{1}{2} \log \frac{Z+1}{Z-1} \quad (7.2.6)$$

The Mangler-Squire pressure distribution requires that the Legendre Polynomials of the second kind be complex (i.e. $Q_n^m(in)$). The general form of the polynomials will involve the natural logarithm of the complex number $(in+1)/(in-1)$. This problem is circumvented by the use of the following identity obtained from reference 73.

$$\tan^{-1} Z = \frac{i}{2} \log \frac{i+Z}{i-Z} \quad (7.2.7)$$

A representative example of obtaining complex Legendre functions will be performed by transforming equation (7.2.6) for our variable $Z = in$

$$Q_0(in) = \frac{1}{2} \log \frac{in+1}{in-1} \quad (7.2.8)$$

$$Q_0(in) = \frac{1}{2} \log \frac{i+1/n}{i-1/n}$$

use of equation (7.2.7) and the fact $(-i) \cdot (-i) = 1$ yields

$$Q_0(in) = -i \tan^{-1} \frac{1}{n} \quad (7.2.9)$$

Making use of the above procedure, results in the following Legendre functions of the second kind which are required for the pressure distribution equation

$$Q_1^0(in) = n \tan^{-1} \frac{1}{n} - 1 \quad (7.2.10)$$

$$Q_3^0(in) = -\frac{n}{2}(5n^2+3) \tan^{-1} \frac{1}{n} + \frac{5n^2}{2} + \frac{2}{3}$$

$$Q_2^1(in) = 3in\sqrt{1+n^2} \tan^{-1} \frac{1}{n} - 3i\sqrt{1+n^2} + \frac{i}{\sqrt{1+n^2}}$$

$$Q_4^1(in) = -\frac{5}{2}in(7n^2+3)\sqrt{1+n^2} \tan^{-1} \frac{1}{n} + \frac{5}{6}i(21n^2+2)\sqrt{1+n^2} + \frac{i}{\sqrt{1+n^2}}$$

$$Q_3^2(in) = -15n(1+n^2) \tan^{-1} \frac{1}{n} + 15n^2 + 10 - \frac{2}{1+n^2}$$

As previously stated in section 3, the functions $Q_n^m(in)$ are evaluated on the rotor disc which requires $n = 0$. Thus, to determine $Q_n^m(i0)$ one must find $\tan^{-1} 1/0$ which could be troublesome to the computer. Noting that for our Ellipsoidal Coordinate System that $n \geq 0$ we can use the following relationship which is obtained from reference 74 to evaluate the functions on the disc

(7.2.11)

$$\begin{aligned} \tan^{-1} \frac{1}{\eta} &= \frac{\pi}{2} - \tan^{-1} \eta \\ \text{when } \eta &= 0 \quad \tan^{-1} 0 = 0 \\ \tan^{-1} \frac{1}{\eta} &= \frac{\pi}{2} \\ \eta &\rightarrow 0 \end{aligned}$$

(7.2.12)

For the induced velocity calculations, we need to determine $\frac{d Q_n^m(i\eta)}{d \eta}$.
The following recursive formula can be used to find the derivative of the Legendre function of the second kind.

$$\frac{d Q_n^m(i\eta)}{d \eta} = \frac{n\eta}{1+\eta^2} Q_n^m(i\eta) + \frac{(n+m)i}{1+\eta^2} Q_{n-1}^m(i\eta) \quad (7.2.13)$$

Therefore, to determine the derivative of the polynomials given in equation (7.2.10) using equation (7.2.13), the following additional polynomials are required.

$$\begin{aligned} Q_0^0(i\eta) &= -i \tan^{-1} \frac{1}{\eta} \\ Q_2^0(i\eta) &= \frac{i}{2} (3\eta^2 + 1) \tan^{-1} \frac{1}{\eta} - \frac{3}{2} i\eta \\ Q_1^1(i\eta) &= \sqrt{1+\eta^2} \tan^{-1} \frac{1}{\eta} - \frac{\eta}{\sqrt{1+\eta^2}} \\ Q_3^1(i\eta) &= -\frac{3}{2} (5\eta^2 + 1) \sqrt{1+\eta^2} \tan^{-1} \frac{1}{\eta} + \frac{15\eta}{2} \sqrt{1+\eta^2} - \frac{\eta}{\sqrt{1+\eta^2}} \\ Q_2^2(i\eta) &= 3i(1+\eta^2) \tan^{-1} \frac{1}{\eta} - 3i\eta - \frac{2i\eta}{1+\eta^2} \end{aligned} \quad (7.2.14)$$

Using equation (7.2.12), the Legendre functions of the second kind on the rotor disc can be explicitly determined and are given below

$$\begin{array}{ll}
 Q_0^0(i\omega) = -\frac{\pi}{2}i & Q_2^1(i\omega) = -2i \\
 Q_1^0(i\omega) = -1 & Q_3^1(i\omega) = -\frac{3}{4}\pi \\
 Q_2^0(i\omega) = \frac{\pi}{4}i & Q_4^1(i\omega) = \frac{8}{3}i \\
 Q_3^0(i\omega) = \frac{2}{3} & Q_2^2(i\omega) = \frac{3\pi}{2}i \\
 Q_1^1(i\omega) = \frac{\pi}{2} & Q_3^2(i\omega) = 8
 \end{array} \tag{7.2.15}$$

In the pressure distribution equation, the Legendre functions of the second kind $Q_2^1(in)$ and $Q_4^1(in)$ are complex and the constants that premultiply them, C_2^1 & D_2^1 and C_4^1 & D_4^1 respectively, are also complex. Consequently, the pressure distribution will consist of real values. The recursive formula for the derivative (7.2.13) includes the complex i in the second term, this insures that derivatives of the complex Q functions will be complex and derivatives of real Q functions will be real. For example, finding the derivative of $Q_4^1(in)$ which is complex, requires the usage of $Q_3^1(in)$ which is real

$$\frac{d Q_4^1(in)}{d n} = \frac{4n}{1+n^2} Q_4^1(in) + \frac{5i}{1+n^2} Q_3^1(in) \tag{7.2.16}$$

Because the Q functions alternate between real and complex numbers, the recursive derivative formula is useful. The complex algebra will be circumvented in the computer program by noting that all terms in the pressure distribution, are real. Thus, the multiplication of the complex Q functions by their respective complex constants is handled by the

negative of the product, because $i \cdot i = -1$. For example, $Q_4^1(i\eta) \cdot C_4^1$ is handled as $-Q_4^1(i\eta) \cdot C_4^1$ where the complex i has been disregarded.

Figures 7.2.1 through 7.2.3 are plots of the Legendre Polynomials of the first kind evaluated on the rotor disc. Also depicted in these figures are the corrected load distributions that result from combinations of the polynomials. The Legendre Polynomials of the second kind, $Q_n^m(i\eta)$, are shown in figures 7.2.4 through 7.2.6. It is noted that all the $Q_n^m(i\eta)$ polynomials become zero as the ellipsoidal coordinate η approaches infinity. However, the rate of decays are different, with $Q_1^0(i\eta)$ decaying at the slowest rate. At an η of 4.0 it is the only polynomial that is nonzero.

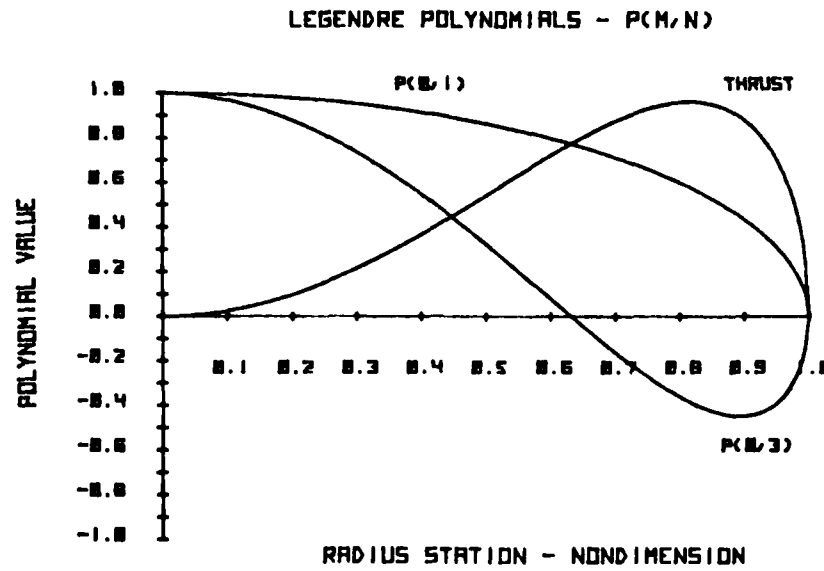


Figure 7.2.1. P_1^0 , P_3^0 and Corrected Thrust for C_T

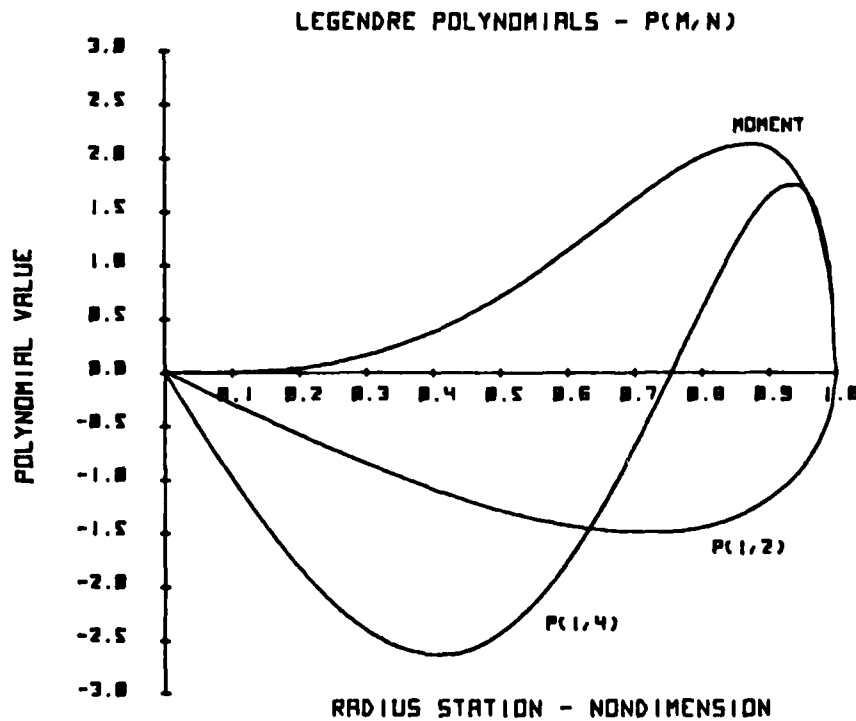


Figure 7.2.2. P_2^1 , P_4^1 and Corrected Moment for C_L and C_M

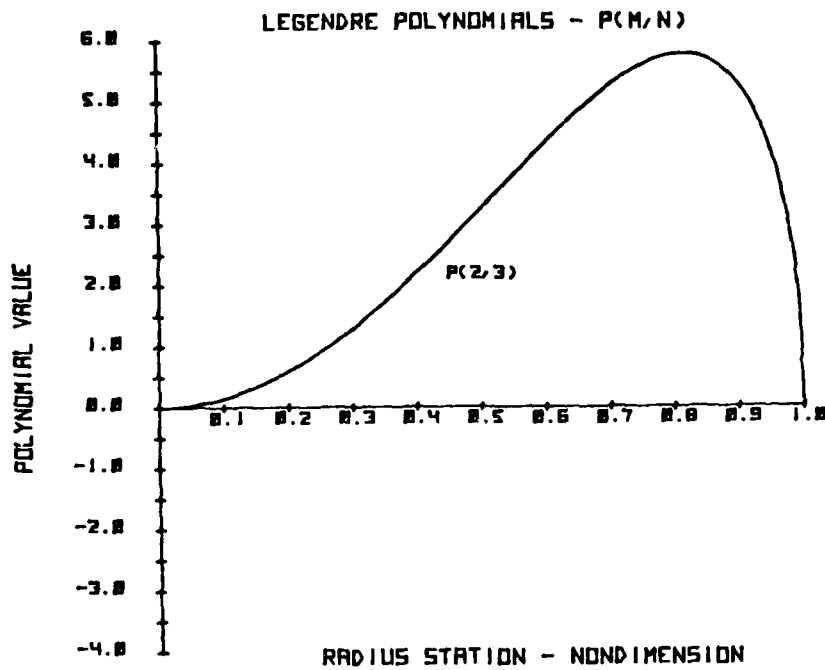


Figure 7.2.3. P_3^2 for C_{2L} and C_{2M}

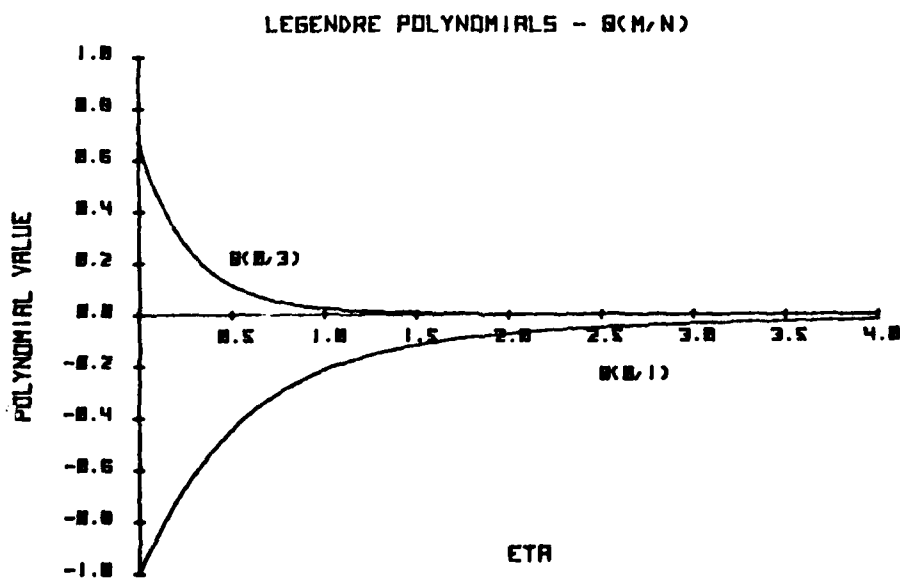


Figure 7.2.4. Q_1^0 and Q_3^0 Variation with n

AD-A099 532

ARMY TROOP SUPPORT AND AVIATION MATERIEL READINESS CO--ETC F/S 20/4
ROTOR DYNAMIC INFLOW DERIVATIVES AND TIME CONSTANTS FROM VARIOU--ETC(U)
DEC 80 D M PITT
TSARCON-TR-81-2

UNCLASSIFIED

NL

3 of 3

ALL INFORMATION CONTAINED
HEREIN IS UNCLASSIFIED

DATE

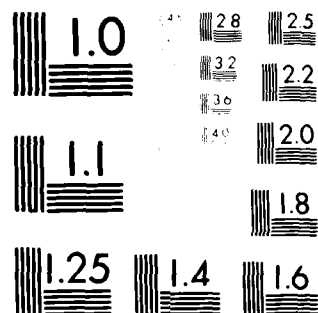
END

DATE

FILED

6-81

DTIC



MICROCOPY RESOLUTION TEST CHART
NATIONAL BUREAU OF STANDARDS-1963-A

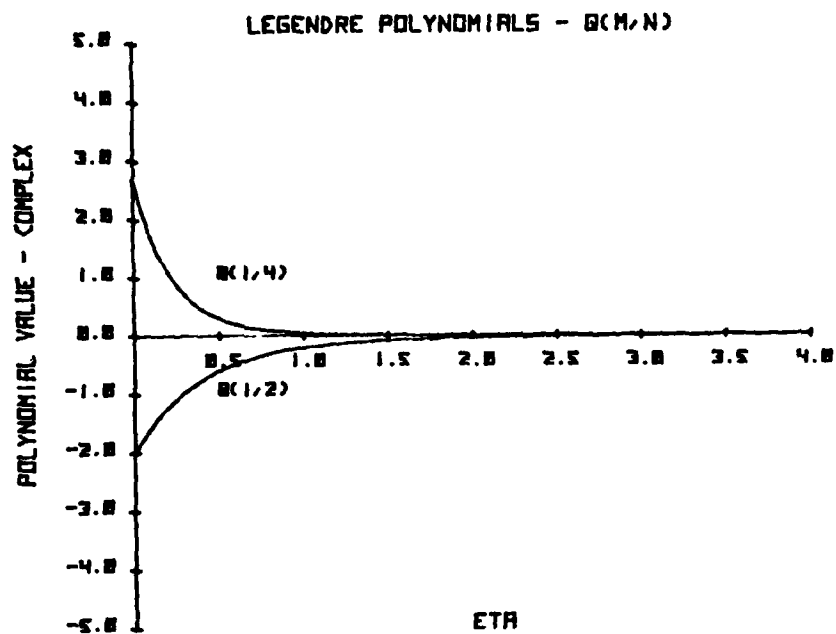


Figure 7.2.5. Q_2^1 and Q_4^1 Variation with η

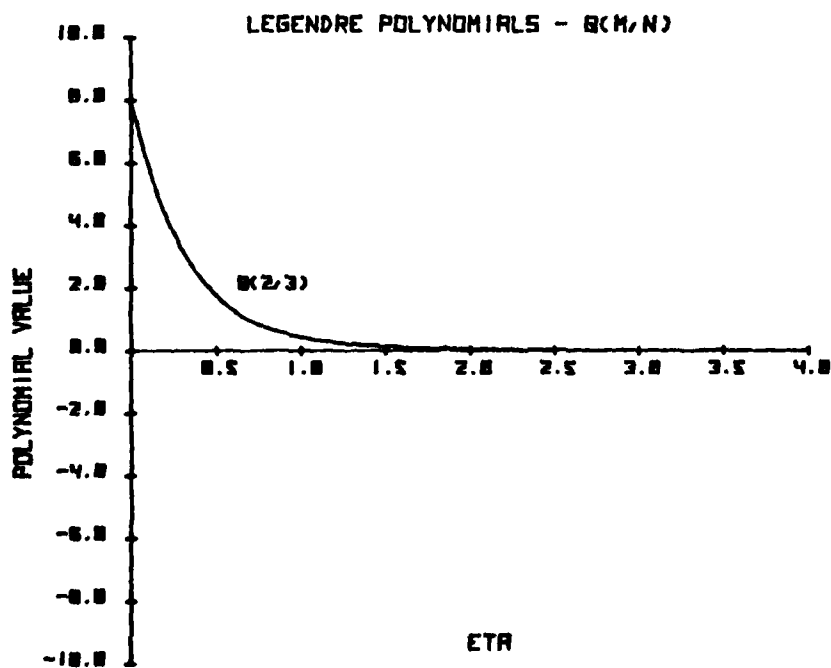


Figure 7.2.6. Q_3^2 Variation with η

APPENDIX 7.3

Actuator Disc Aerodynamic Loading

The purpose of this appendix is to describe the various aerodynamic loadings associated with the Legendre Polynomials. Due to the orthogonality of the Legendre Polynomials the property of superposition holds. Consequently, each loading will be described separately. The actual trim flight loading condition will be represented by a combination of all the loading conditions.

Figure 7.3.1 depicts a loading condition that only has a radial variation. This loading is called the uncorrected thrust distribution, and is given by equation 7.3.1 on the rotor disc.

$$p = \frac{-3C_T p_1^0}{4V^2}(\nu) \quad (7.3.1)$$

The thrust loading is corrected with the use of $P_3^0(\nu)$ term. This will yield zero lift both at the hub and edge of the disc. This loading is shown in figure 7.3.2. It should be noted that the thrust loading only varies in the radial direction and has no azimuth variation.

A negative pitching moment is shown in figure 7.3.3. The loading varies in the azimuth direction as $\cos\psi$. The loading will be zero at $\psi=90^\circ$ and $\psi=270^\circ$. It should be noted that the harmonic airloads (pitch moment, roll moment,

etc.) do not change the total thrust on the disc, but only changes its distribution.

Figure 7.3.4 is a negative rolling moment and is seen to have maximum value at $\psi=90^\circ$ and $\psi=270^\circ$. At an azimuth position of $\psi=0^\circ$ and 180° the loading is zero. The rolling moment varies as $\sin\psi$.

The second harmonic aerodynamic loadings vary as $\cos 2\psi$ and $\sin 2\psi$ and are shown in figures 7.3.5 and 7.3.6 respectively. These loadings will be zero at four azimuth positions.

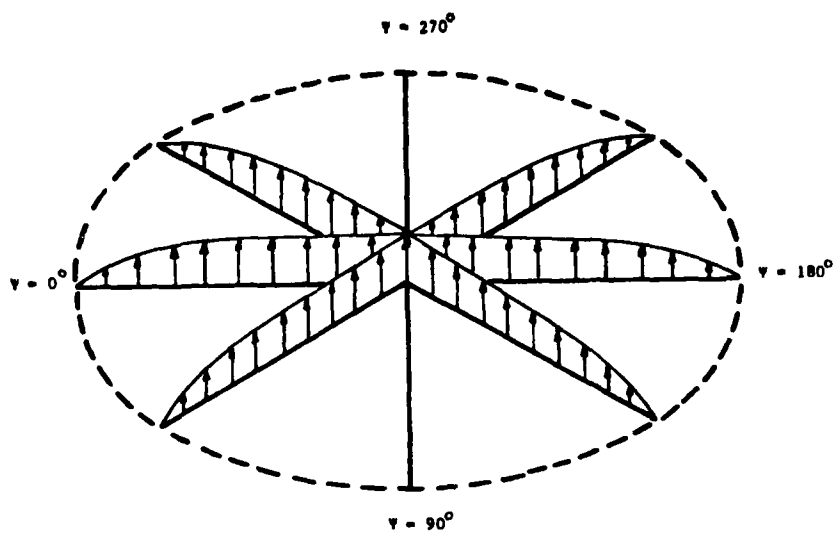


Figure 7.3.1. Uncorrected Thrust Distribution

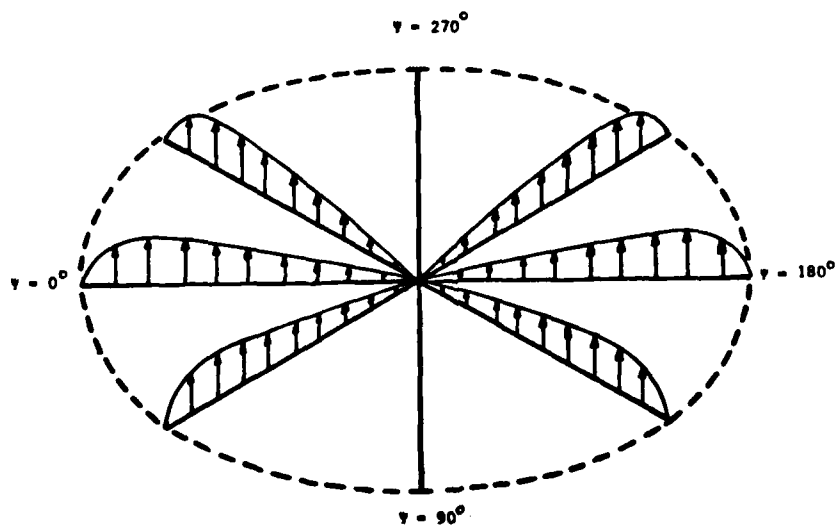


Figure 7.3.2. Corrected Thrust Distribution

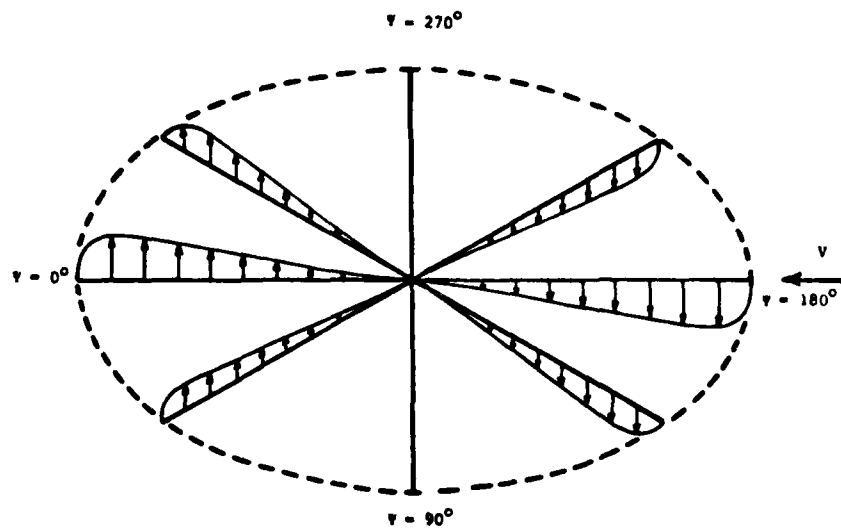


Figure 7.3.3. Negative Pitching Moment Distribution

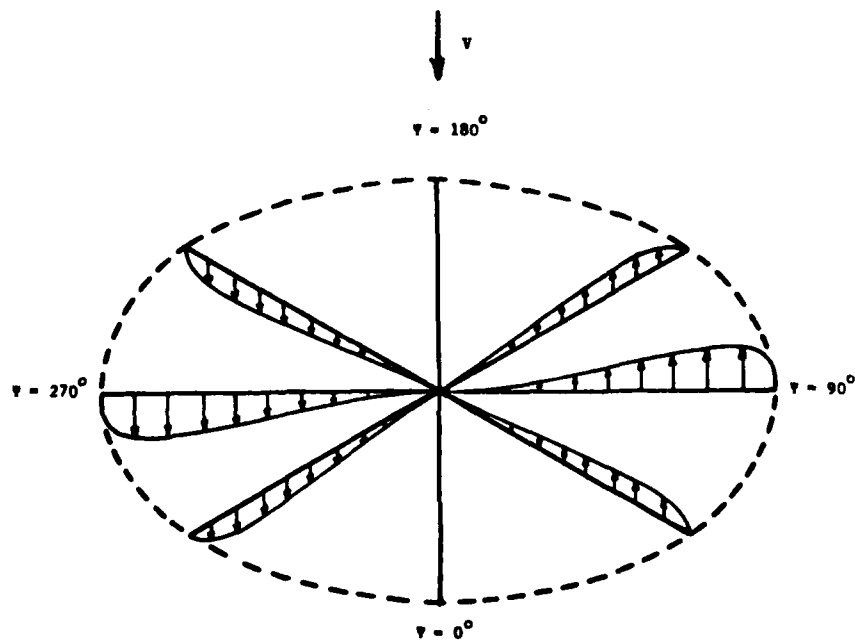


Figure 7.3.4. Negative Rolling Moment Distribution

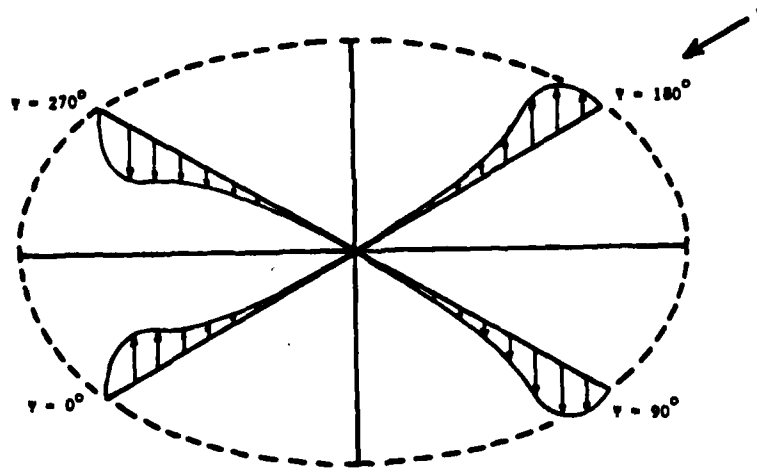


Figure 7.3.5. Negative Second Harmonic Loading
Distribution of $\cos 2\psi$

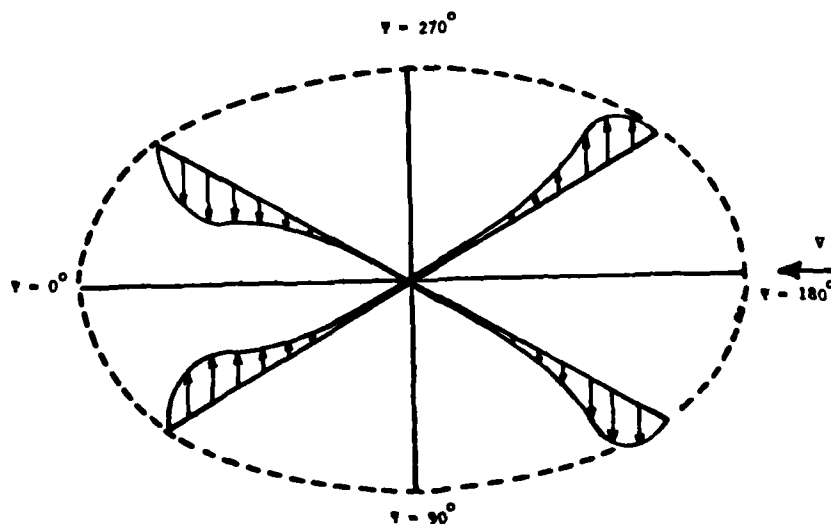


Figure 7.3.6. Negative Second Harmonic Loading
Distribution of $\sin 2\psi$

APPENDIX 7.4

Unsteady Actuator Disc-Supplemental Data

The remaining unsteady actuator disc results are presented in the appendix. Figures 7.4.1 - 7.4.10 are the magnitudes of the second through third column of the complex inverted 5x5 L-matrix. The phase angles are presented in figures 7.4.11 - 7.4.20. Figures 7.4.21 - 7.4.30 are the imaginary terms of the complex inverted L-matrix. The deviations between the S.P. real part and S.V. real part are presented in figures 7.4.31 - 7.4.40. Finally, the differences between the upper 3x3 of the S.V. 5x5 inverted complex L-matrix and the S.V. 3x3 inverted complex L-matrix are shown in figures 7.4.41 - 7.4.43.

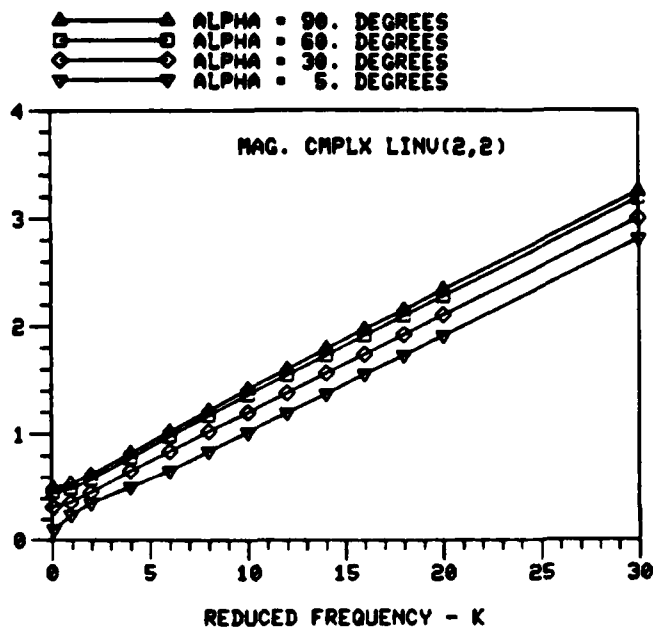
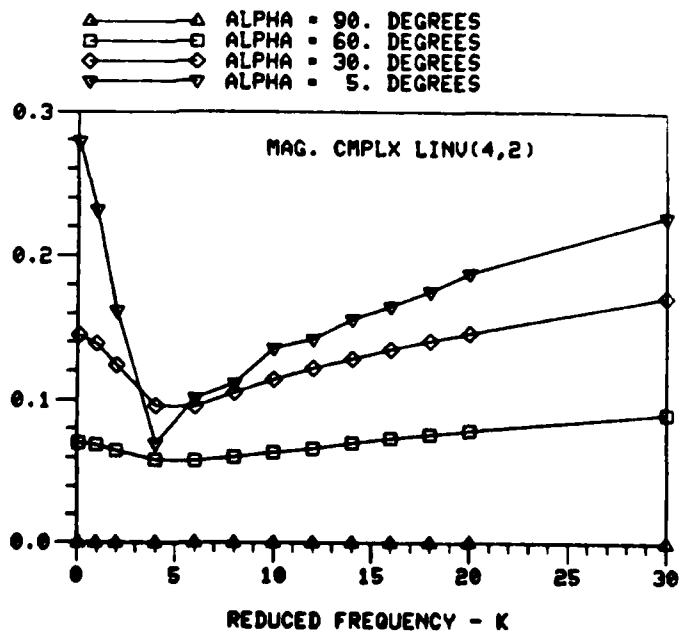


Figure 7.4.1
Magnitude of the
(2,2) Element of
Inverted Complex
L(K) Matrix for
a Sweep (Corrected
Pressure)

Figure 7.4.2
Magnitude of the
(4,2) Element of
Inverted Complex
L(K) Matrix for
a Sweep (Corrected
Pressure)



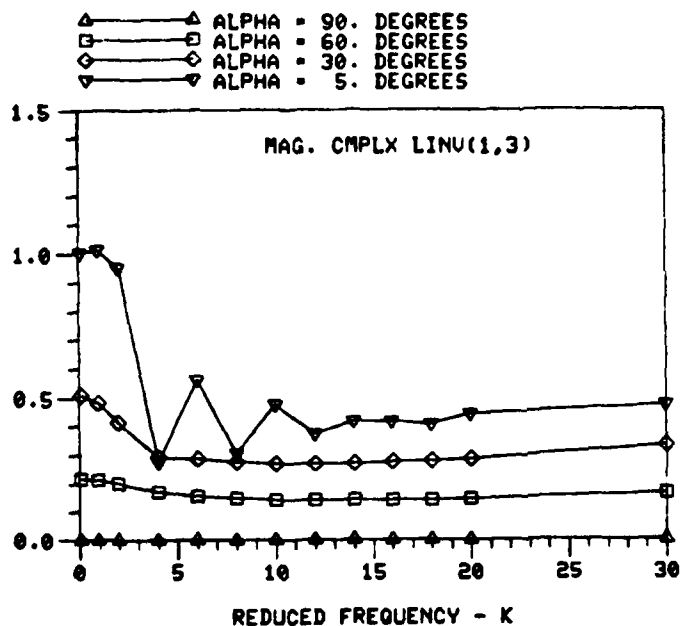
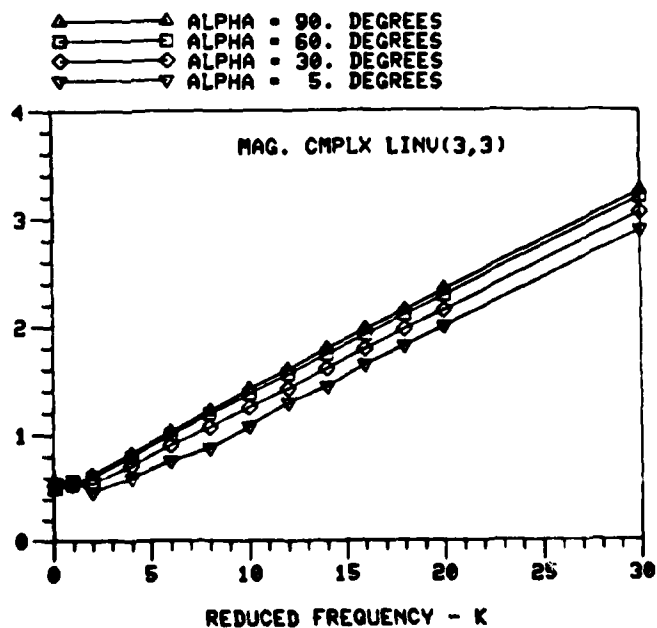


Figure 7.4.3
Magnitude of the
(1,3) Element of
Inverted Complex
L(K) Matrix for
 α Sweep (Corrected
Pressure)

Figure 7.4.4
Magnitude of the
(3,3) Element of
Inverted Complex
L(K) Matrix for
 α Sweep (Corrected
Pressure)



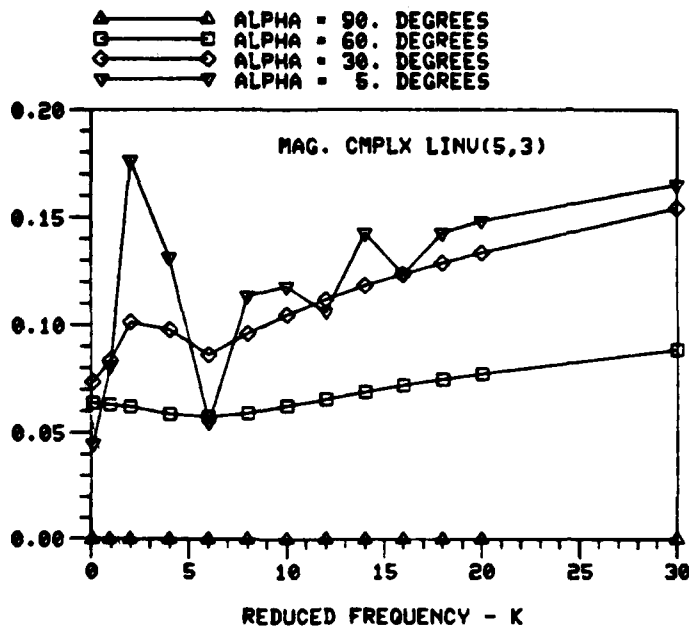
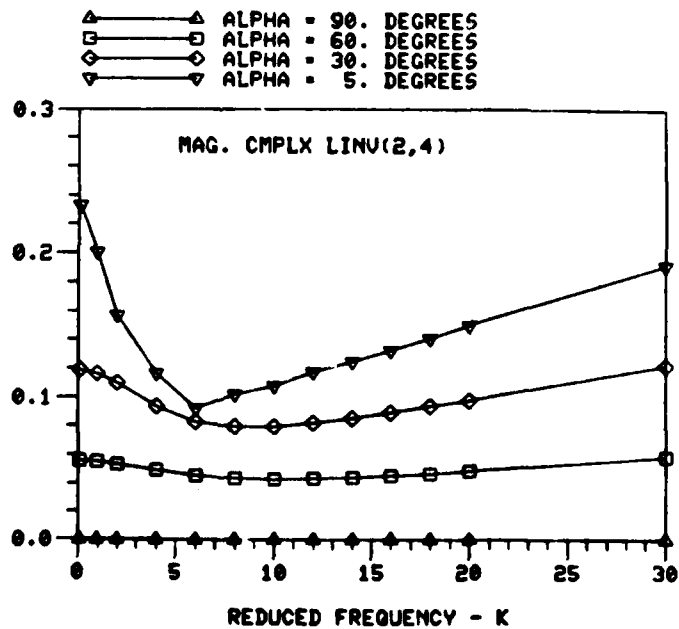


Figure 7.4.5
Magnitude of the
(5,3) Element of
Inverted Complex
L(K) Matrix for
 α Sweep (Corrected
Pressure)

Figure 7.4.6
Magnitude of the
(2,4) Element of
Inverted Complex
L(K) Matrix for
 α Sweep (Corrected
Pressure)



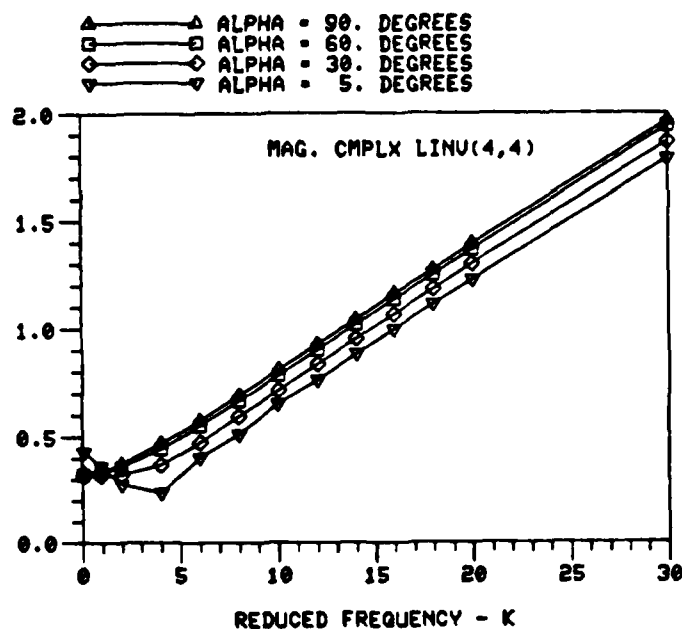
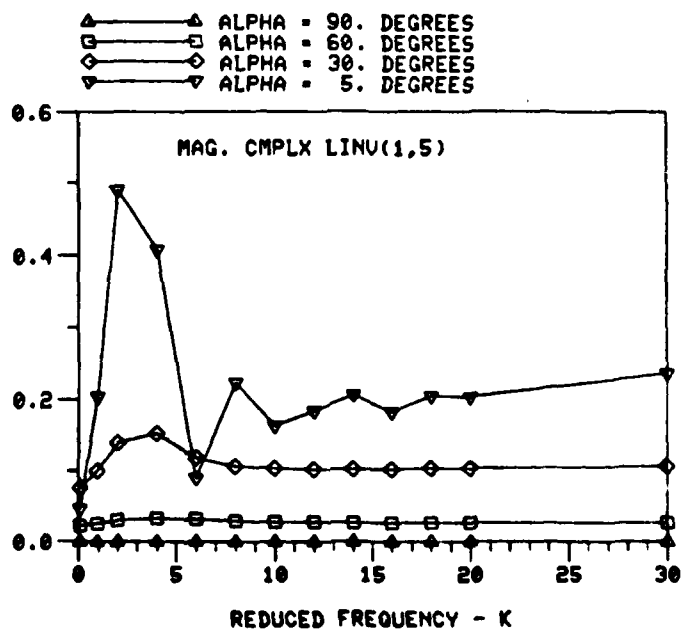


Figure 7.4.7
Magnitude of the
(4,4) Element of
Inverted Complex
L(K) Matrix for
 α Sweep (Corrected
Pressure)

Figure 7.4.8
Magnitude of the
(1,5) Element of
Inverted Complex
L(K) Matrix for
 α Sweep (Corrected
Pressure)



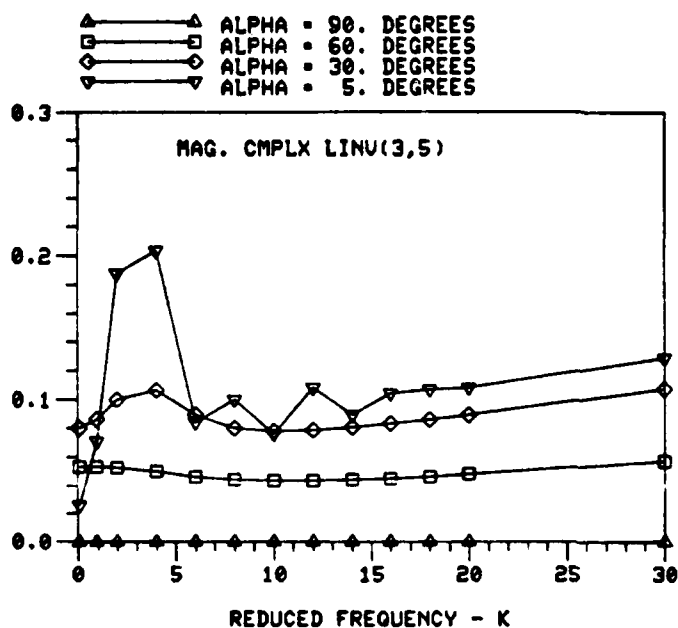
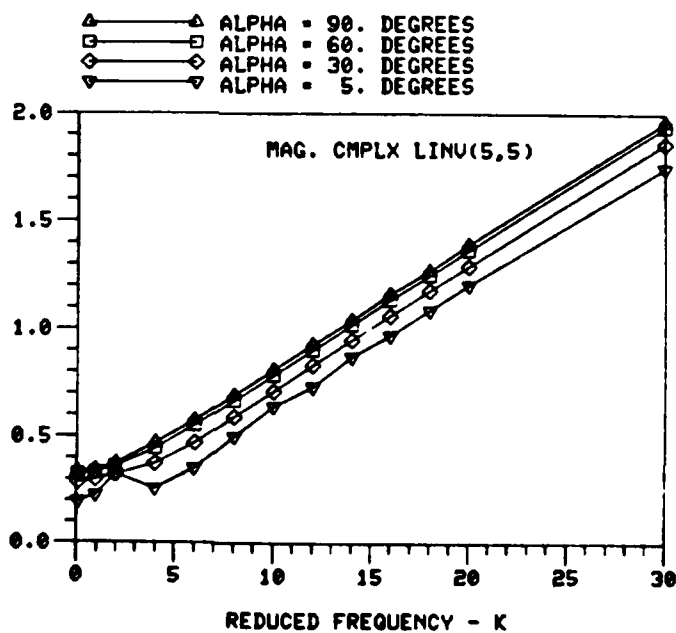


Figure 7.4.9
Magnitude of the
(3,5) Element of
Inverted Complex
L(K) Matrix for
 α Sweep (Corrected
Pressure)

Figure 7.4.10
Magnitude of the
(5,5) Element of
Inverted Complex
L(K) Matrix for
 α Sweep (Corrected
Pressure)



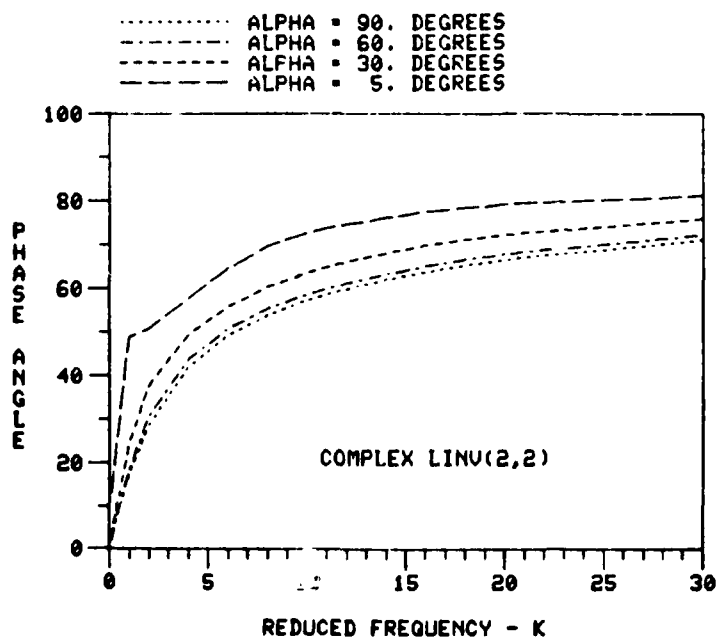
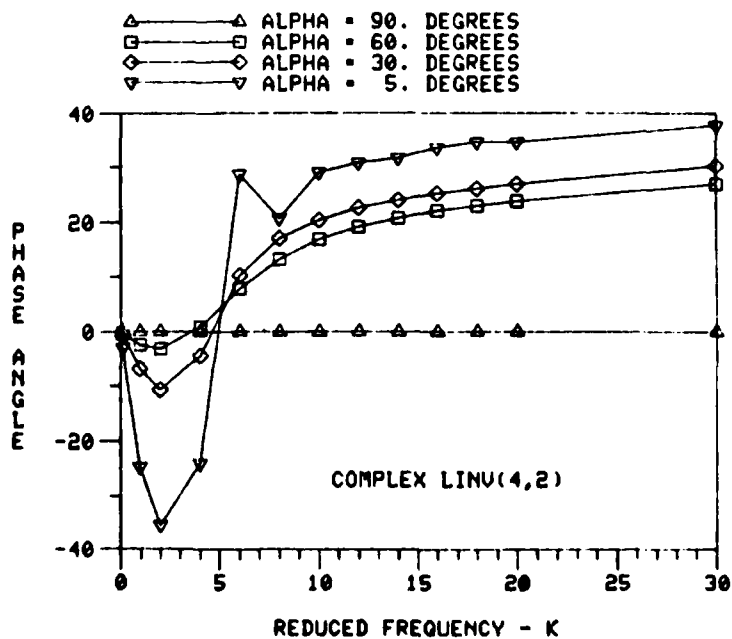


Figure 7.4.11
Phase Angle of the
(2,2) Element of
Inverted Complex
 $L(K)$ Matrix for α
Sweep (Corrected
Pressure)

Figure 7.4.12
Phase Angle of the
(4,2) Element of
Inverted Complex
 $L(K)$ Matrix for α
Sweep (Corrected
Pressure)



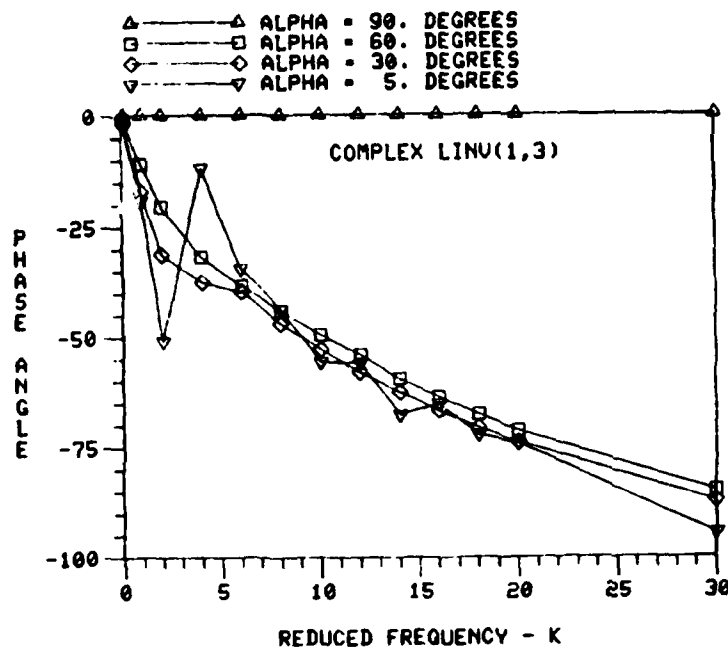
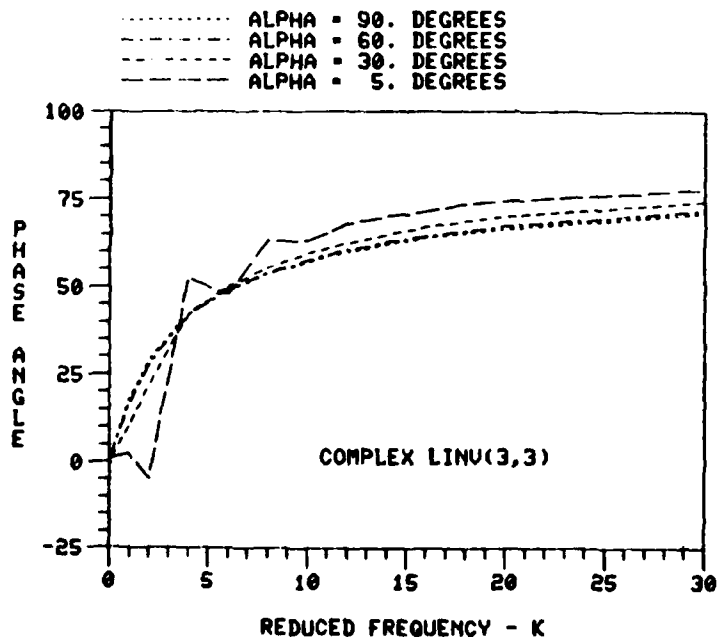


Figure 7.4.13
Phase Angle of the
(1,3) Element of
Inverted Complex
 $L(K)$ Matrix for α
Sweep (Corrected
Pressure)

Figure 7.4.14
Phase Angle of the
(3,3) Element of
Inverted Complex
 $L(K)$ Matrix for α
Sweep (Corrected
Pressure)



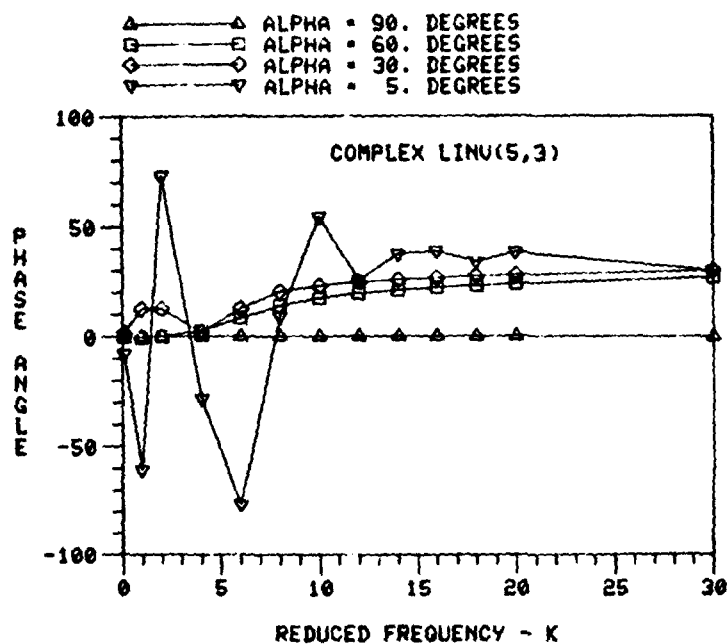
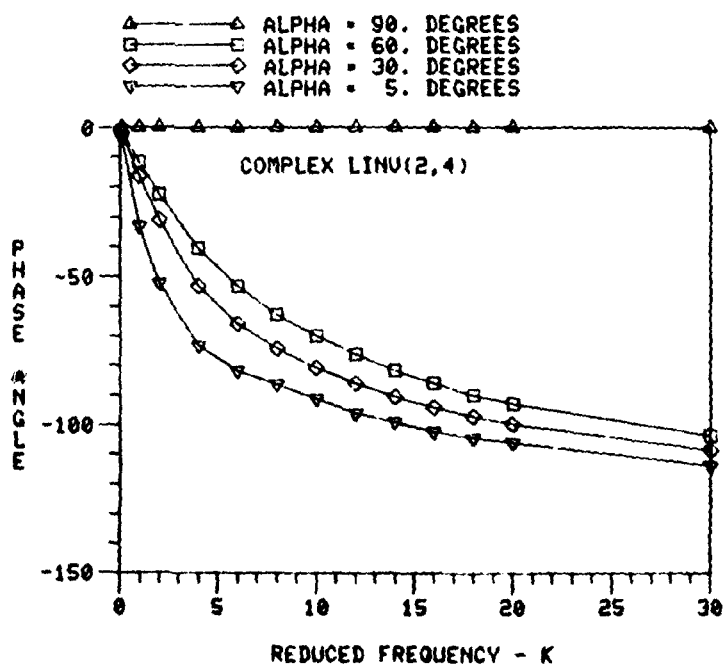


Figure 7.4.15
Phase Angle of the
(5,3) Element of
Inverted Complex
L(K) Matrix for α
Sweep (Corrected
Pressure)

Figure 7.4.16
Phase Angle of the
(2,4) Element of
Inverted Complex
L(K) Matrix for α
Sweep (Corrected
Pressure)



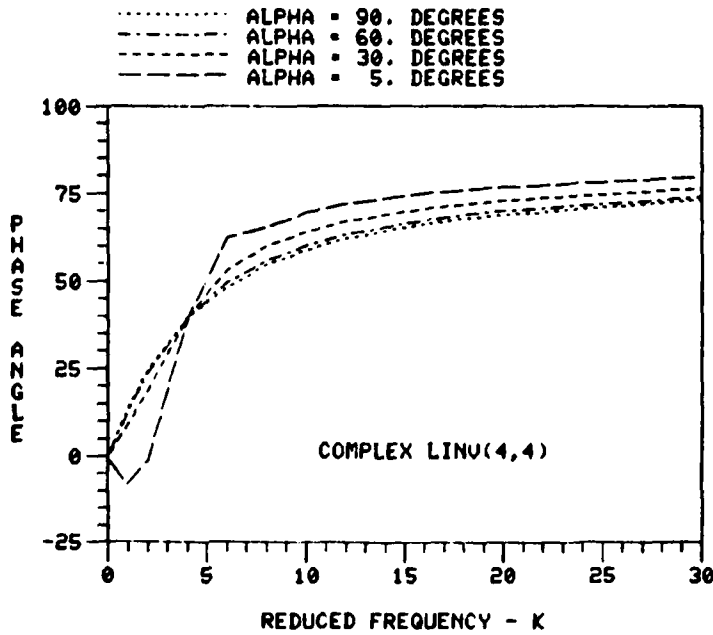
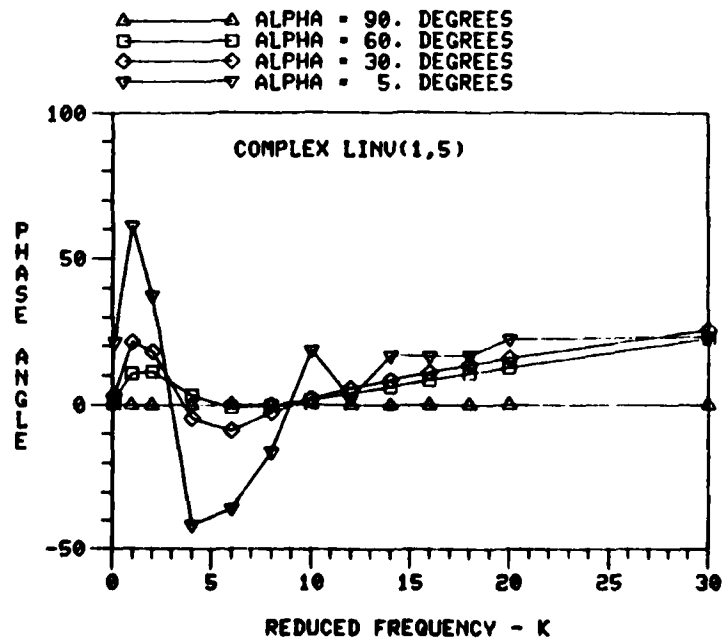


Figure 7.4.17
Phase Angle of the
(4,4) Element of
Inverted Complex
L(K) Matrix for a
Sweep (Corrected
Pressure)

Figure 7.4.18
Phase Angle of the
(1,5) Element of
Inverted Complex
L(K) Matrix for a
Sweep (Corrected
Pressure)



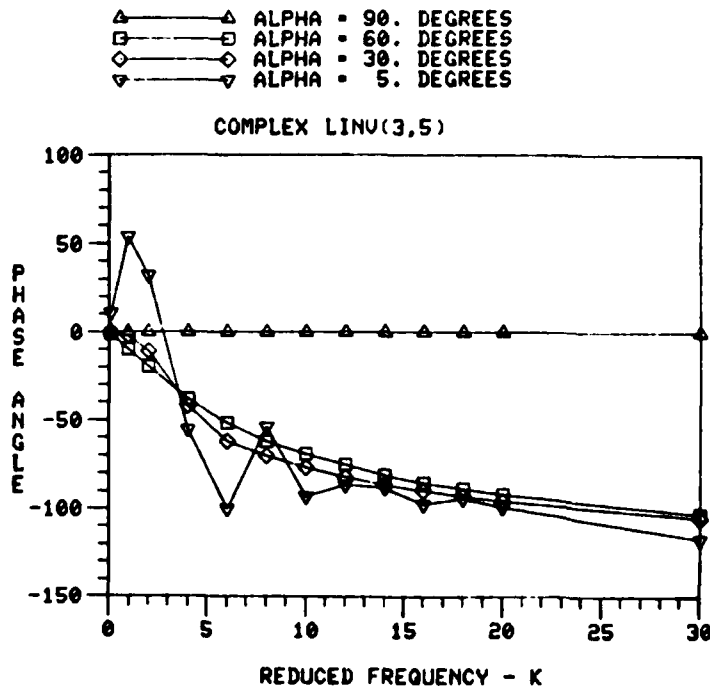
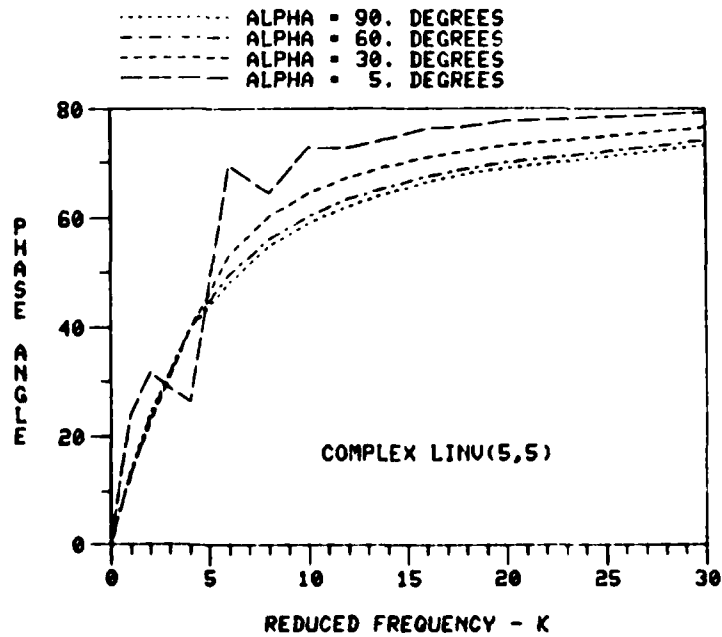


Figure 7.4.19
 Phase Angle of the
 (3,5) Element of
 Inverted Complex
 L(K) Matrix for α
 Sweep (Corrected
 Pressure)

Figure 7.4.20
 Phase Angle of the
 (5,5) Element of
 Inverted Complex
 L(K) Matrix for α
 Sweep (Corrected
 Pressure)



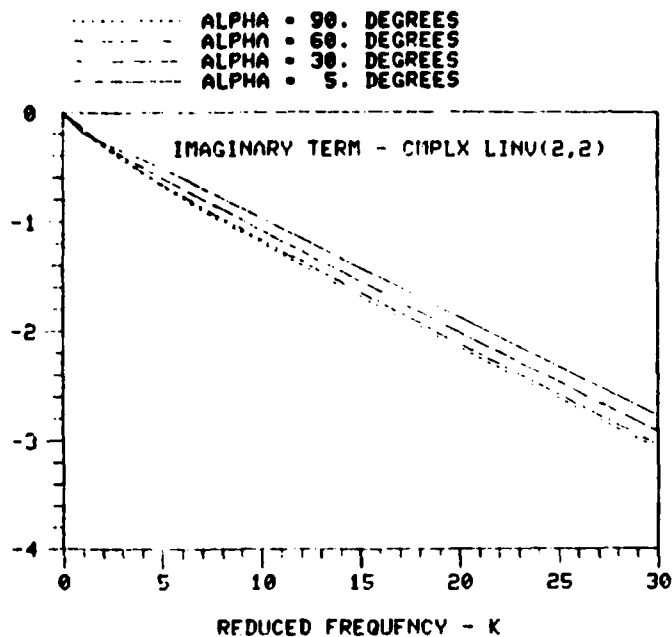
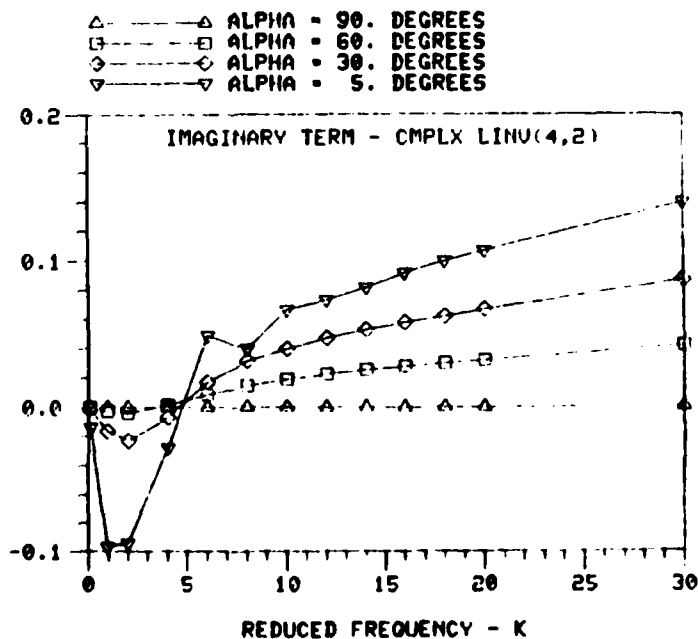


Figure 7.4.21
Imaginary Term of
the (2,2) Element
Inverted Complex
L(K) Matrix for α
Sweep (Corrected
Pressure)

Figure 7.4.22
Imaginary Term of
the (4,2) Element
Inverted Complex
L(K) Matrix for α
Sweep (Corrected
Pressure)



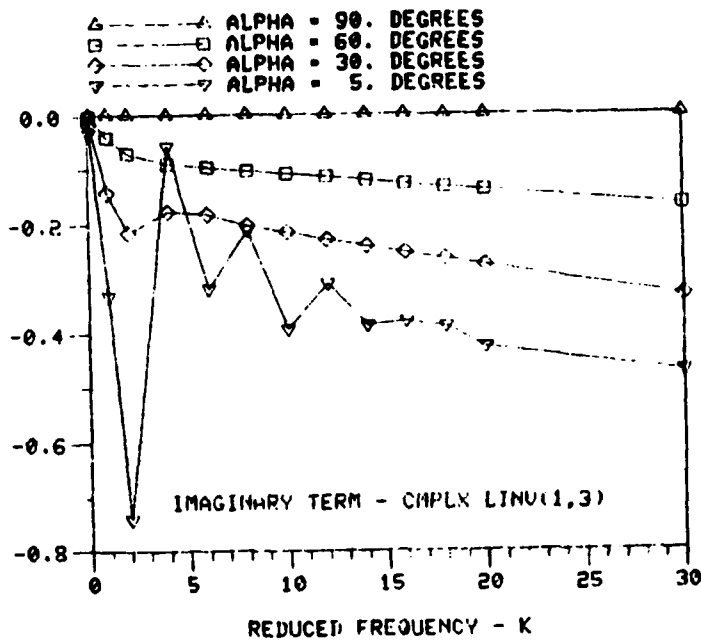
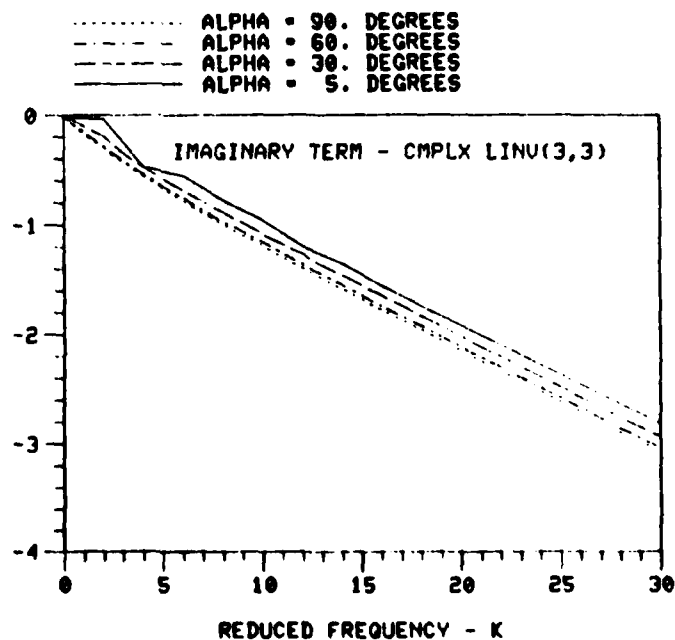


Figure 7.4.23
Imaginary Term of
the (1,3) Element
Inverted Complex
 $L(K)$ Matrix for α
Sweep (Corrected
Pressure)

Figure 7.4.24
Imaginary Term of
the (3,3) Element
Inverted Complex
 $L(K)$ Matrix for α
Sweep (Corrected
Pressure)



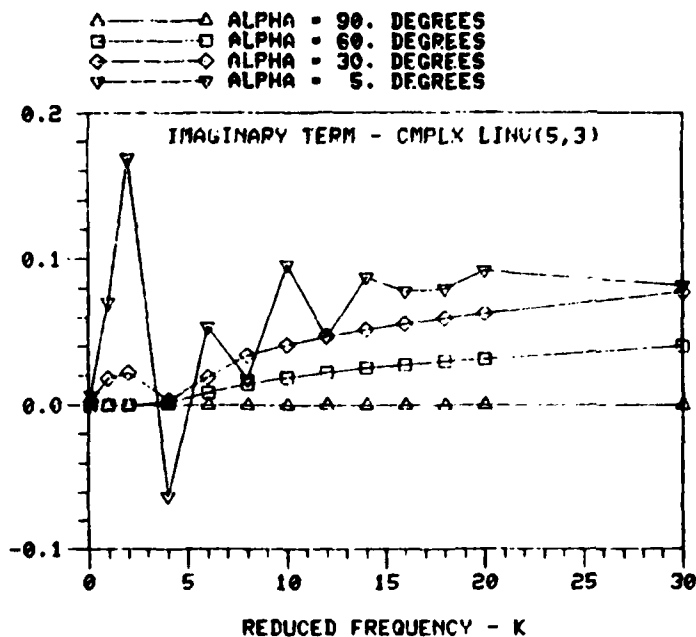
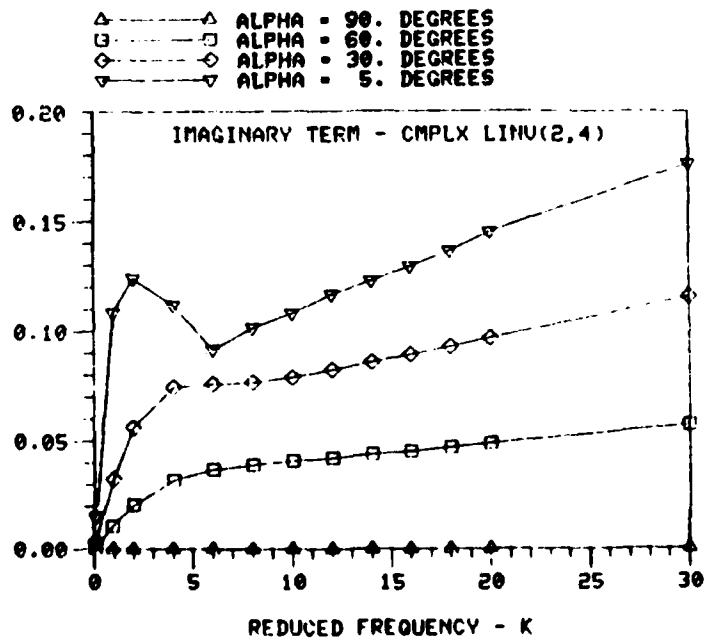


Figure 7.4.25
Imaginary Term of
the (5,3) Element
Inverted Complex
L(K) Matrix for α
Sweep (Corrected
Pressure)

Figure 7.4.26
Imaginary Term of
the (2,4) Element
Inverted Complex
L(K) Matrix for α
Sweep (Corrected
Pressure)



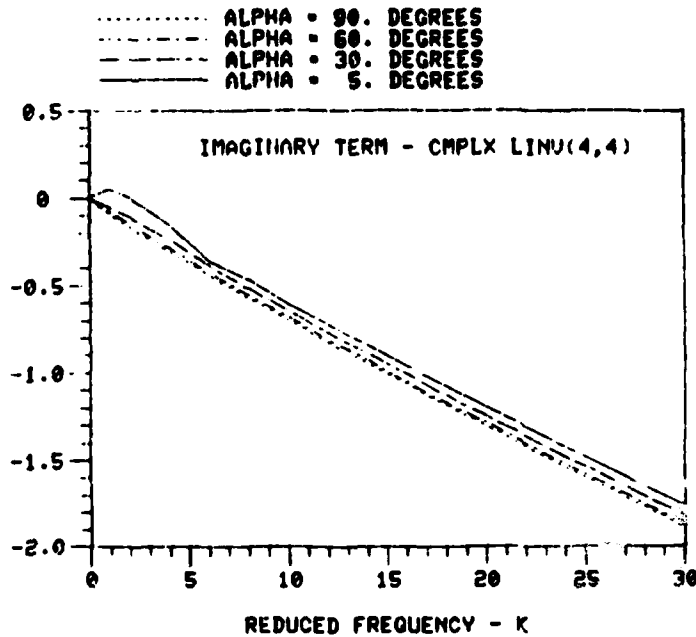
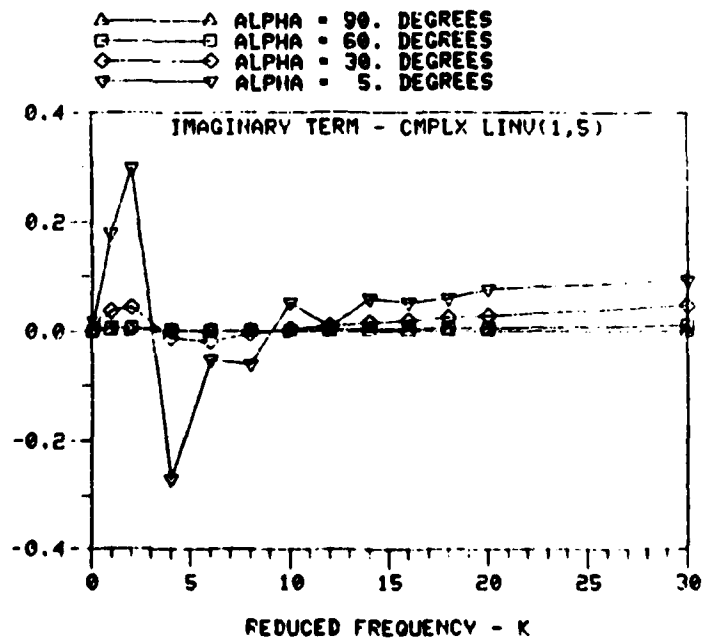


Figure 7.4.27
Imaginary Term of
the (4,4) Element
Inverted Complex
L(K) Matrix for a
Sweep (Corrected
Pressure)

Figure 7.4.28
Imaginary Term of
the (1,5) Element
Inverted Complex
L(K) Matrix for a
Sweep (Corrected
Pressure)



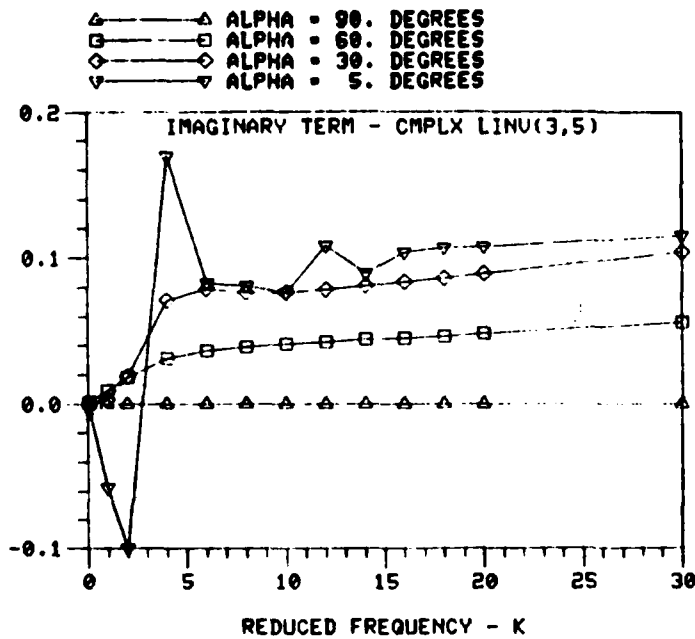
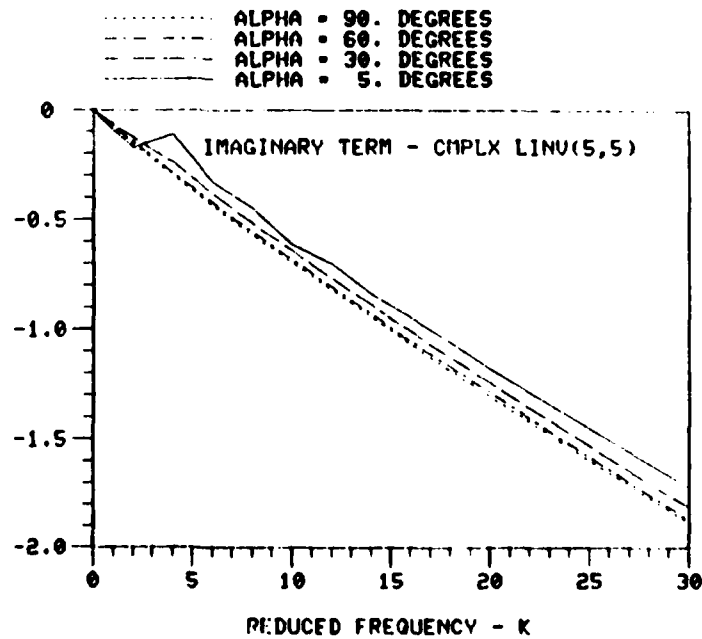


Figure 7.4.29
Imaginary Term of
the (3,5) Element
Inverted Complex
L(K) Matrix for α
Sweep (Corrected
Pressure)

Figure 7.4.30
Imaginary Term of
the (5,5) Element
Inverted Complex
L(K) Matrix for α
Sweep (Corrected
Pressure)



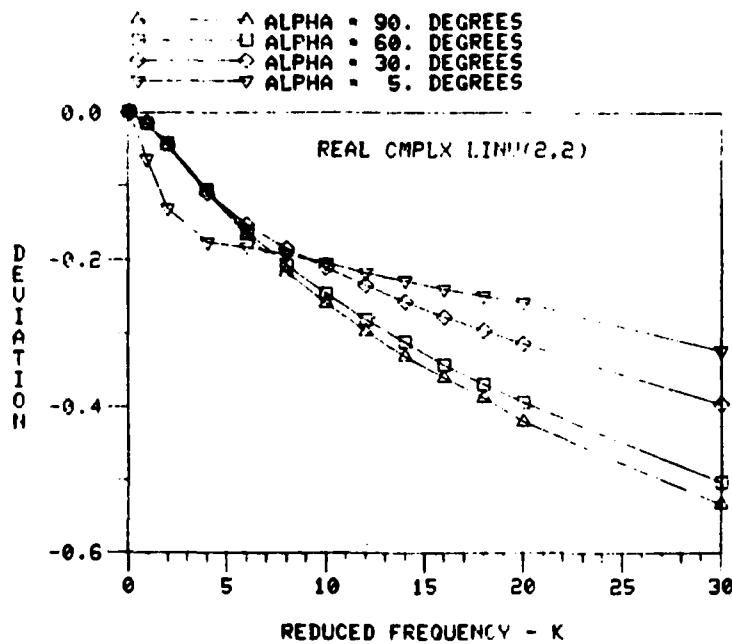
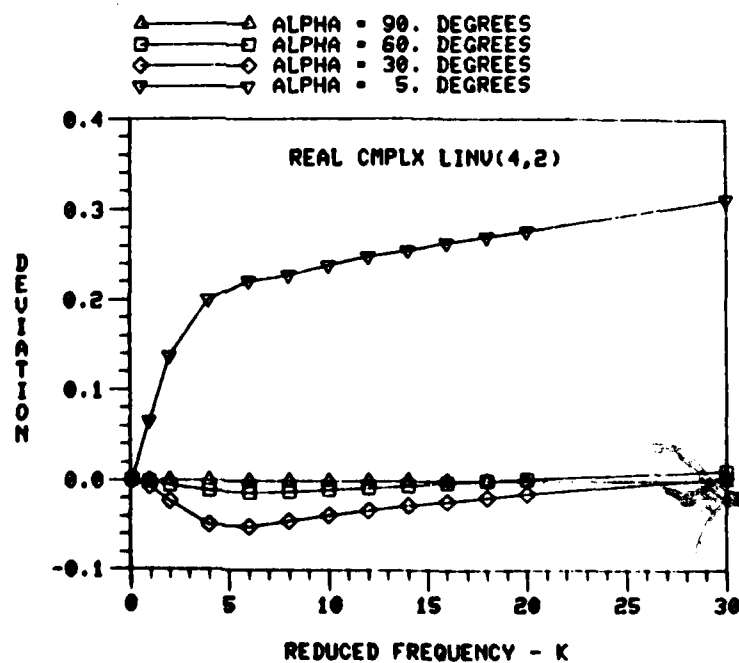


Figure 7.4.31
Deviation of
Real Terms of
the (2,2) Element
Inverted Complex
L(K) Matrix for a
Sweep (Corrected
Pressure)

Figure 7.4.32
Deviation of
Real Terms of
the (4,2) Element
Inverted Complex
L(K) Matrix for a
Sweep (Corrected
Pressure)



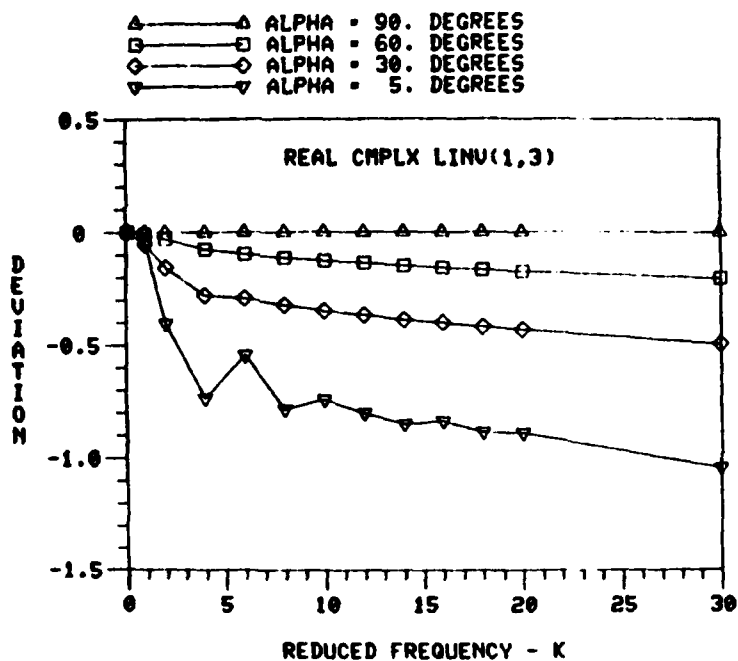
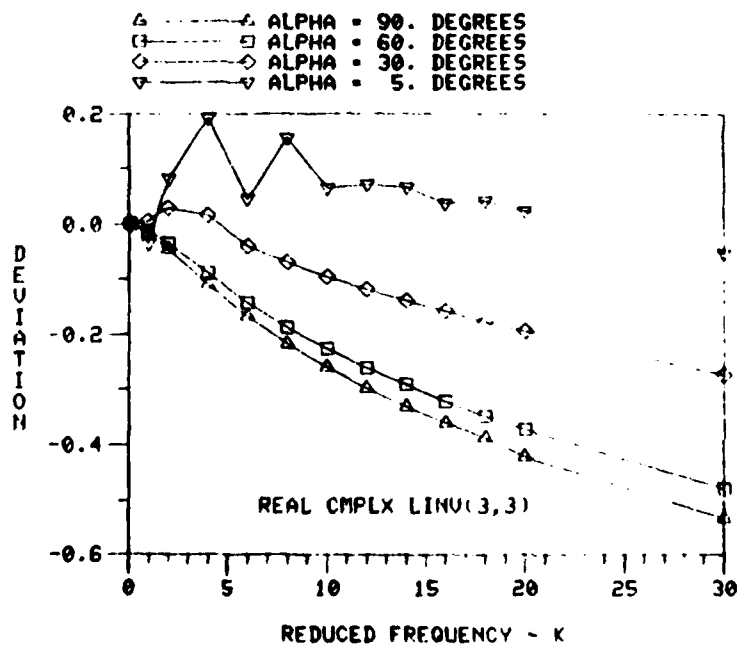


Figure 7.4.33
Deviation of
Real Terms of
the (1,3) Element
Inverted Complex
L(K) Matrix for α
Sweep (Corrected
Pressure)

Figure 7.4.34
Deviation of
Real Terms of
the (3,3) Element
Inverted Complex
L(K) Matrix for α
Sweep (Corrected
Pressure)



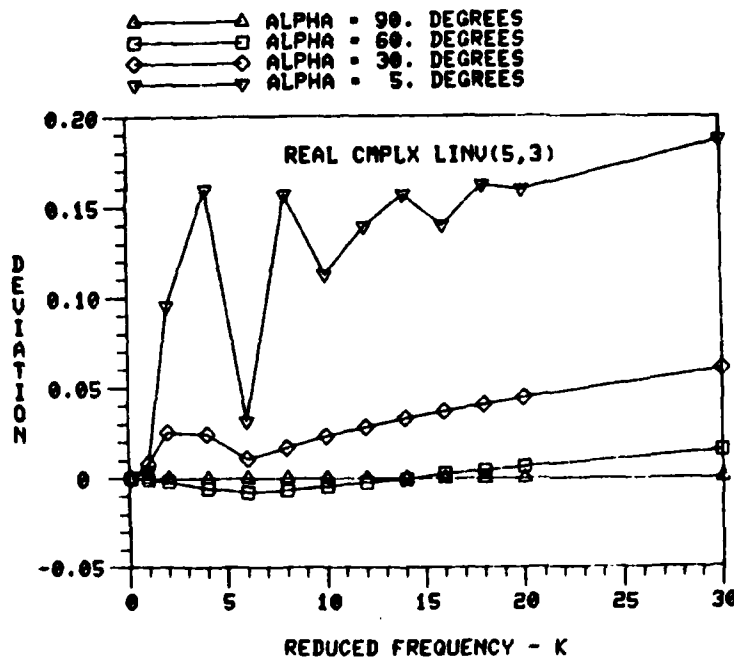
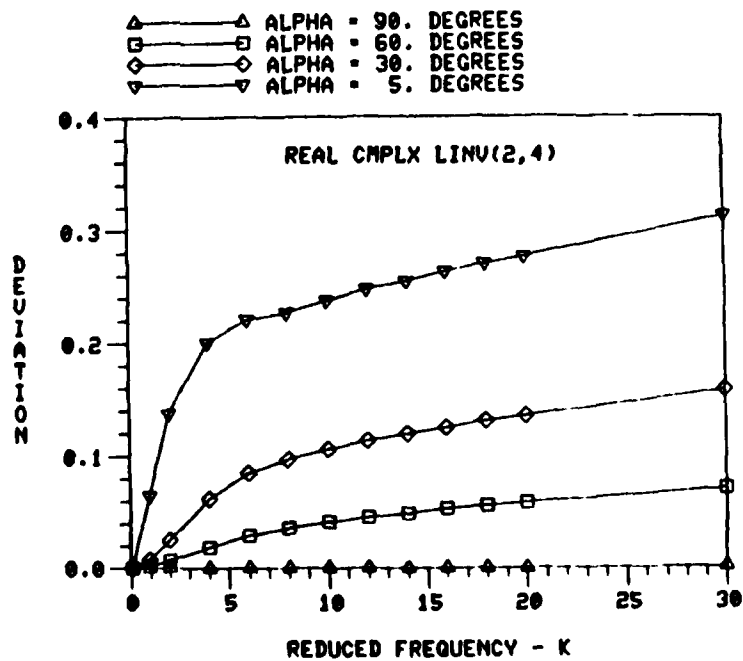


Figure 7.4.35
Deviation of
Real Terms of
the (5,3) Element
Inverted Complex
L(K) Matrix for α
Sweep (Corrected
Pressure)

Figure 7.4.36
Deviation of
Real Terms of
the (2,4) Element
Inverted Complex
L(K) Matrix for α
Sweep (Corrected
Pressure)



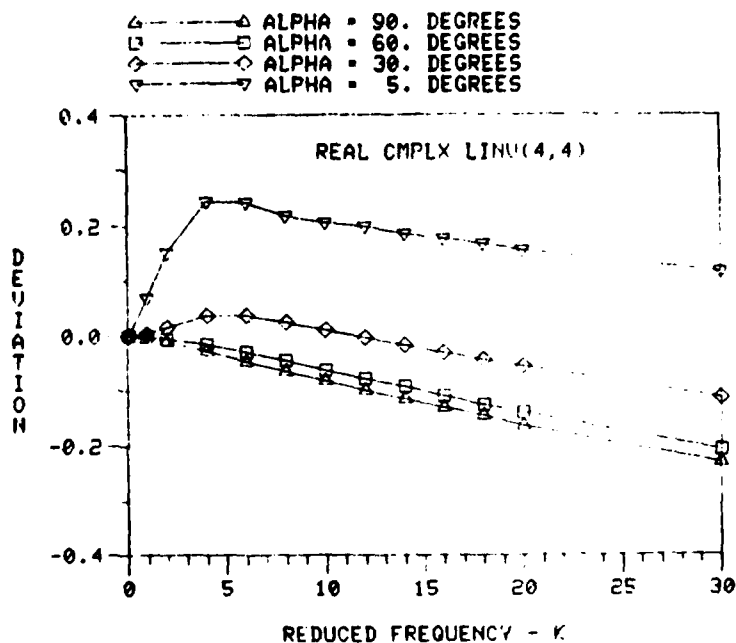
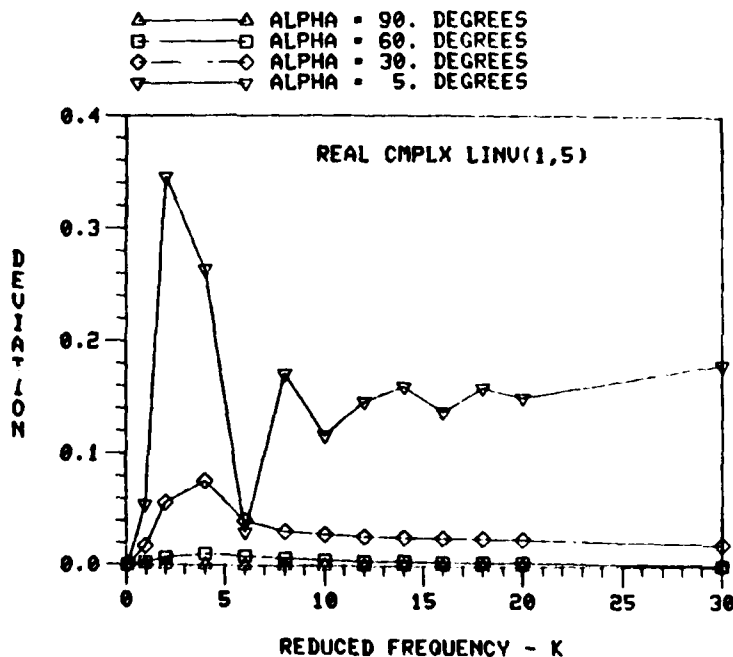


Figure 7.4.37
Deviation of
Real Terms of
the (4,4) Element
Inverted Complex
L(K) Matrix for a
Sweep (Corrected
Pressure)

Figure 7.4.38
Deviation of
Real Terms of
the (1,5) Element
Inverted Complex
L(K) Matrix for a
Sweep (Corrected
Pressure)



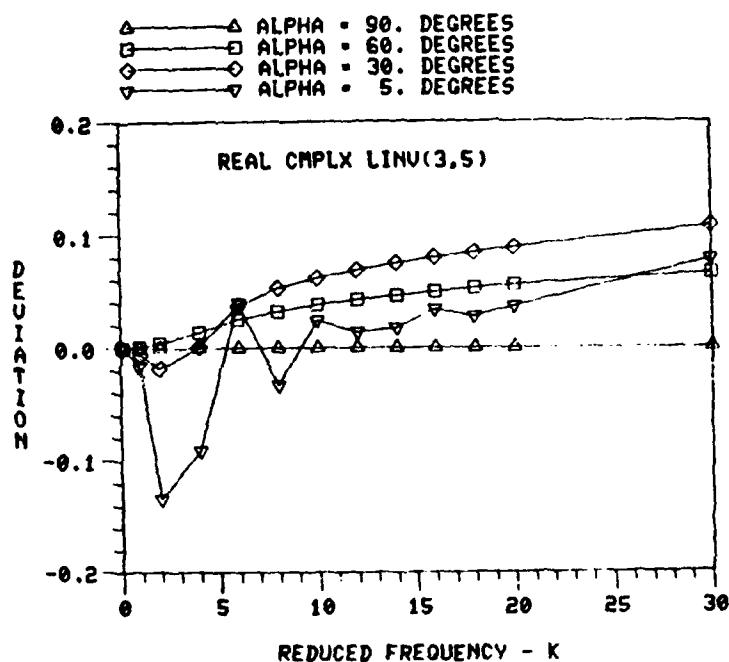
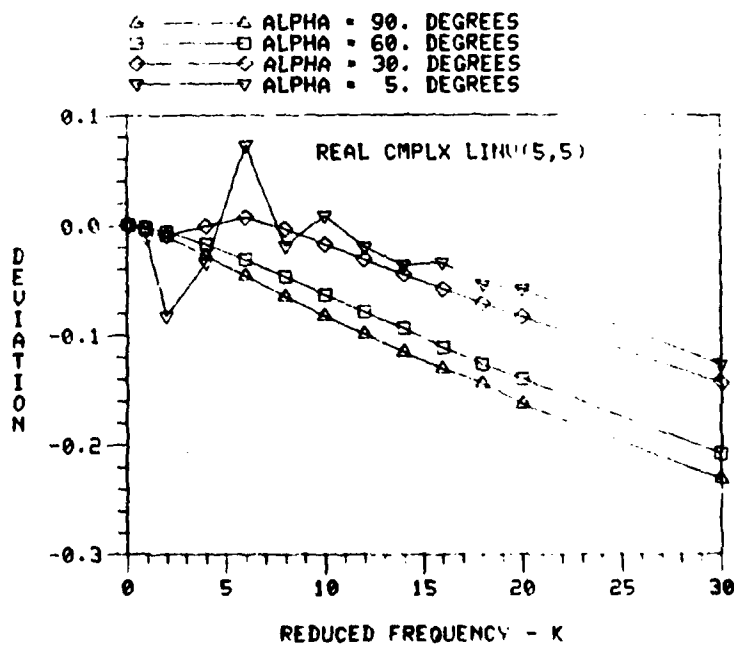


Figure 7.4.39
Deviation of
Real Terms of
the (3,5) Element
Inverted Complex
L(K) Matrix for α
Sweep (Corrected
Pressure)

Figure 7.4.40
Deviation of
Real Terms of
the (5,5) Element
Inverted Complex
L(K) Matrix for α
Sweep (Corrected
Pressure)



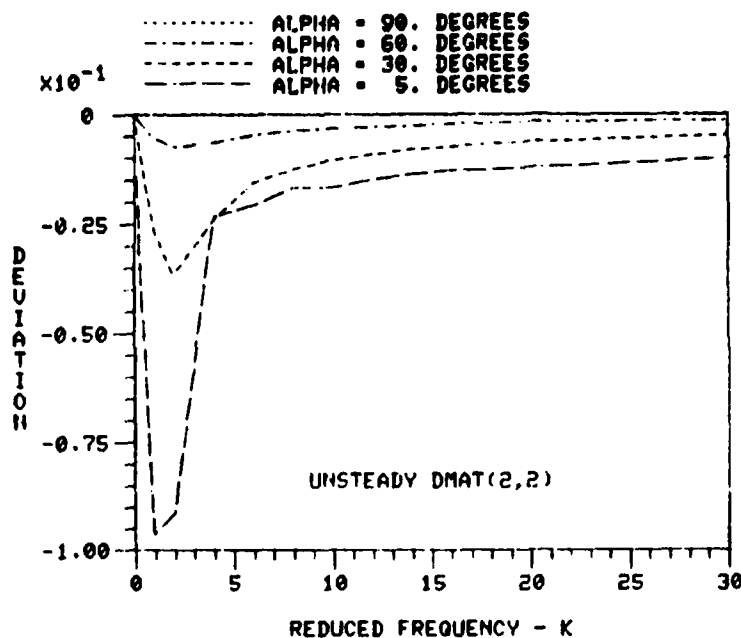
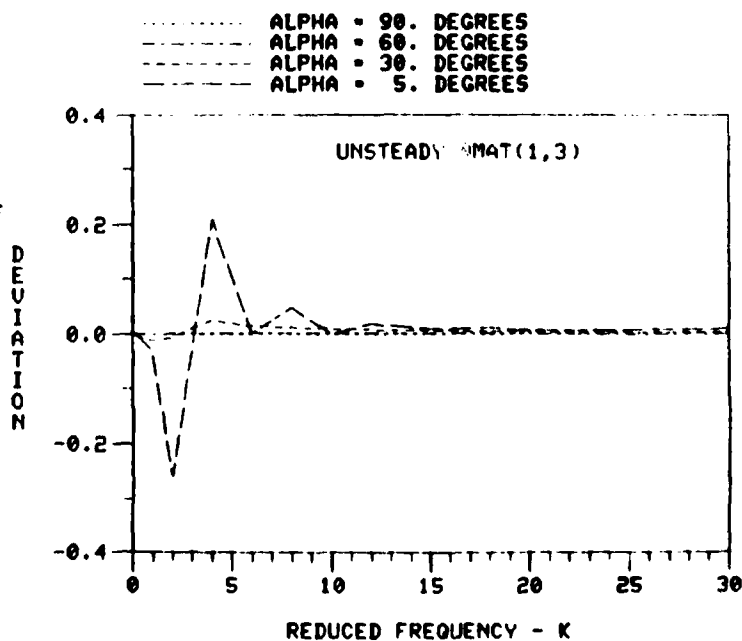


Figure 7.4.41
Deviation of
Imaginary Terms of
the (2,2) Element
Inverted Complex
L(K) Matrix for α
Sweep (Corrected
Pressure)

Figure 7.4.42
Deviation of
Imaginary Terms of
the (1,3) Element
Inverted Complex
L(K) Matrix for α
Sweep (Corrected
Pressure)



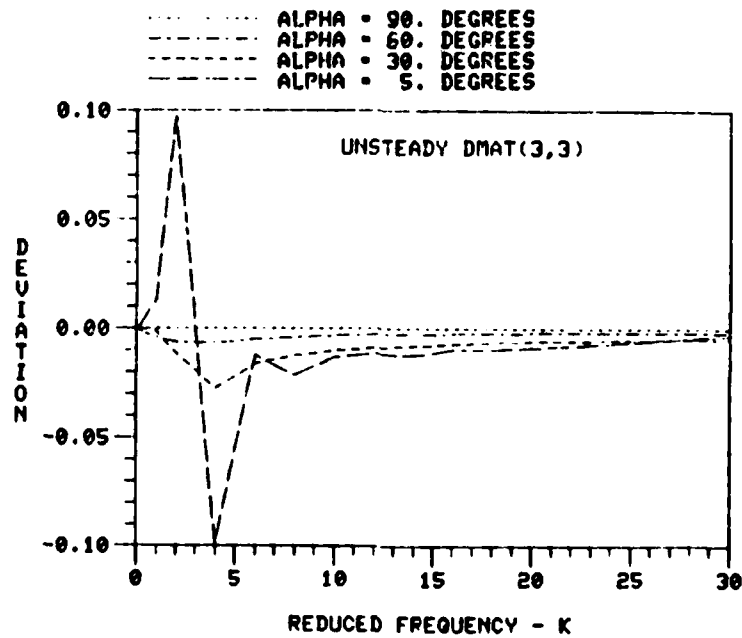


Figure 7.4.43. Deviation of Imaginary Terms of the (3,3) Element Inverted Complex L(K) Matrix for a Sweep (Corrected Pressure)

APPENDIX 7.5

Nomenclature

- a = two-dimensional lift curve slope, $dC_l/d\alpha \text{ rad}^{-1}$
- AD = abbreviation for Actuator Disc
- A_o = real component of out-of-phase pressure
- b = number of rotor blades
- B = tip loss factor
- B_o = imaginary component of out-of-phase pressure distribution
- c = blade cord length, ft.
- {CD} = column matrix of constants C_n^m and D_n^m of Mangler-Squire pressure distribution
- C_{do}^* = equivalent drag coefficient
- C_L = harmonic perturbation of roll-moment coefficient
= roll moment/ $\rho\pi\Omega^2 R^5$, positive advancing blade down
- C_{2L} = second-harmonic-pressure perturbation coefficient
= $L_2/\rho\pi\Omega^2 R^6$
- C_M = harmonic perturbation of pitch-moment coefficient
= pitch moment/ $\rho\pi\Omega^2 R^5$, positive nose up
- C_{2M} = second-harmonic-pressure perturbation coefficient
= $M_2/\rho\pi\Omega^2 R^6$
- C_T = harmonic perturbation of thrust coefficient
- \bar{C}_T = steady value of thrust coefficient = $T/\rho\pi\Omega^2 R^4$
- C_n^m = constant in the pressure distribution multiplying the cosine term
- D.L. = abbreviation for disc loading, lb/ft^2
- D_n^m = constant in the pressure distribution multiplying the sine term
- {F} = column matrix of thrust, rolling and pitching moment coefficients
- {dF} = generalized rotor thrust and moments
- i = $\sqrt{-1}$

[I] = identity matrix

I_A = apparent inertia of air, slug-ft²

$j = \sqrt{-1}$

K = slope of Glauert's linear representation of momentum induced-velocity distribution also used as the reduced frequency, ω/v , in unsteady actuator disc theory

[K] = nondimensional apparent mass diagonal matrix

[K_E] = inverse of empirical [L] matrix

K_M, K_I = nondimensional apparent mass and inertia of impermeable disc

(i)' = lift per radial blade station, i

L = rotor roll moment

[L] = nonuniform induced inflow matrix

[\bar{L}] = matrix that relates the constants C_n^m and D_n^m of the pressure distribution to the induced flow perturbations

[L_E] = empirical value for quasi-steady portion of L-matrix

[L(K)] = complex or unsteady nonuniform induced inflow matrix

[L(K)]_E = empirical complex L-matrix

\mathcal{L} = Laplace Operator

M = rotor pitch moment

[M], [M'] = rotor response partial derivative matrix for control inputs without inflow, open-loop and closed-loop respectively

[M] = apparent mass matrix

m_A = apparent mass of air, slugs

N = total number of rotor azimuth positions

[N] = rotor response partial derivative matrix for induced inflow components

p = Mangler-Squire pressure distribution

- P_n^m = Legendre functions of the first kind
- P_o = complex pressure distribution utilized in superposition of pressure method
- PW = abbreviation for Prescribed Wake
- \bar{q} = nondimensional fluid velocity, $q/\Omega R$
- \bar{q}_i = in-phase induced velocity components in the i axis direction
- q_i = component of fluid velocity in the i axis
- [Q] = nonuniform induced inflow matrix, imaginary parts only
- $\bar{Q}_i(X,Y,Z)$ = induced velocity at point (X, Y, Z) in the i direction
- Q_n^m = Legendre functions of the second kind
- r = distance of blade element from axis of rotation
- \bar{r} = nondimensional rotor distance, r/R
- R = rotor radius, ft.
- s = Laplace domain variable
- S.P. = abbreviation for Superposition of Pressures
- S.V. = abbreviation for Superposition of Velocities
- T = rotor thrust, lb.
- [T] = matrix that relates the lift distribution {F} to coefficient matrix {CD}
- u = imaginary component or out-of-phase induced velocity
- v_o = momentum theory induced velocity, ft/sec
- $v(r)$ = induced velocity at nondimensional blade radius station
- v = induced flow parameter
- $V_{FS} = V_\infty$ = free stream velocity, ft/sec
- V = forward velocity of the rotor

- V_R = resultant airflow through the rotor
- $\bar{W}(X,Y,Z)$ = nondimensional induced velocity normal to the rotor disc
- w = real component or in-phase induced velocity
- X, Y, Z = Wind Cartesian Coordinate System
- X', Y', Z' = Disc Cartesian Coordinate System
- $\bar{X}', \bar{Y}', \bar{Z}'$ = location of the induced velocity segment as it is being integrated along the streamline, i.e. functions of ξ
- $(*) = \delta/\delta\psi$
- $()' = \delta/\delta x$
- $(),_i = \delta/\delta i$
- α = hub pitch angle, positive nose up; also angle-of-attack of tip path plane
- α^* = effective angle-of-attack for a thrusting rotor
- γ = lock number, $\rho a c R^4 \int_0^R r^2 dm$
- γ^* = equivalent lock number
- Γ_b = circulation about the rotor blade
- θ = blade pitch angle
- $\bar{\theta}$ = steady collective pitch angle
- $\theta_o, \theta_s, \theta_c$ = rotor pitch angles
- $\{d\theta\}$ = generalized control inputs
- λ = classical inflow ratio = $(V \sin(\alpha) - v)/\Omega R$; also for dynamic inflow theory it is the total inflow through the rotor including induced flow
- $\bar{\lambda}$ = steady inflow ratio = $V/\Omega R + \bar{v}$
- $\{d\lambda\}$ = generalized inflow components
- $\lambda_o, \lambda_s, \lambda_c$ = inflow perturbations including induced flow
- μ = classical advance ratio = $V \cos \alpha / \Omega R$
- v = total induced flow

\bar{v} = induced flow due to steady rotor thrust

$v_o, v_s, v_c,$
 v_{2s}, v_{2c} = induced flow perturbations

$\{v\}$ = induced flow perturbation matrix

ξ = "dummy" variable of integration along streamline
or in X axis direction

ρ = mass density of air slugs/ft³

σ = rotor solidity = $bc/\pi R$

τ = inflow time constant

τ_M, τ_I = induced flow time constants; thrust, pitch and
roll respectively, rad⁻¹

ϕ = nondimensional Mangler-Squire pressure
distribution = $p/\rho V^2$

$\bar{\phi}$ = in-phase pressure distribution for Superposition
of Velocities Method

$\hat{\phi}$ = nondimensional Mangler-Squire pressure
distribution (rotor tip speed) = $P/\rho (\Omega R)^2$

ψ = rotor blade azimuth position, rad

ω = excitation frequency divided by Ω

ω_f = nondimensional frequency in fixed frame

Ω = rotor blade angular velocity, rad/sec

χ = wake skew angle, $\chi = \tan^{-1} \mu/\lambda_o$

v, η, ψ = Ellipsoidal Coordinate System

∇ = vector operator $\frac{\partial}{\partial x} \hat{x} + \frac{\partial}{\partial y} \hat{y} + \frac{\partial}{\partial z} \hat{z}$

div = divergence

8. BIBLIOGRAPHY

1. Glauert, H., "A General Theory of the Autogyro", Aeronautical Research Council (Great Britain), R&M No. 1111, 1926.
2. Sissingh, G. J., "The Effect of Induced Velocity Variation on Helicopter Rotor Damping in Pitch or Roll", Aeronautical Research Council (Great Britain), A.R.C. Technical Report C.P. No. 101 (14, 757), 1952.
3. Gessow, A., and Myers, C. G., Jr., Aerodynamics of the Helicopter, The Frederick Unger Publishing Company, New York, 1952.
4. Knight, Montgomery and Hefner, Ralph A., "Static Thrust Analysis of Lifting Airscrew", NACA TN 626, 1937.
5. Gessow, A., "Review of Information on Induced Flow of a Lifting Rotor", NACA TN 3238, August 1954.
6. Stepniewski, W. Z., "Rotary Wing Aerodynamics", NASA CR-3082, 1979.
7. Harris, F. D. and McVeigh, M. A., "Uniform Downwash with Rotors Having a Finite Number of Blades", Journal of The American Helicopter Society, Vol. 21, No. 1, January 1976.
8. Harris, F. D., "Articulated Rotor Blade Flapping Motion at Low Advance Ratio", Journal of The American Helicopter Society, Vol. 17, No. 1, January 1972.
9. Coleman, R. P., Feingold, A. M., and Stempin, C. W., "Evaluation of the Induced-Velocity Field of an Idealized Helicopter Rotor", NACA WR L-126, June 1945.
10. Castles, W. and DeLeeuw, J. H., "The Normal Component of the Induced Velocity in the Vicinity of a Lifting Rotor and Some Examples of Its Application", NACA TR 1184, 1954.
11. Castles, W. and Durham, H. L., "Distribution of Normal Component of Induced Velocity in Lateral Plane of a Lifting Rotor", NACA TN 3841, December 1956.
12. Heyson, H. H. and Kotzoff, S., "Induced Velocities Near a Lifting Rotor with Nonuniform Disc Loading", NACA TR 1319, 1957.
13. Heyson, H. H., "A Note on the Mean Value of Induced Velocity for a Helicopter Rotor", NASA TN D-240, 1960.

14. Heyson, H. H., "Equations for the Induced Velocities Near a Lifting Rotor With Nonuniform Azimuthwise Vorticity Distribution", NASA TN D-394, 1960.
15. Heyson, H. H., "Tables and Charts of the Normal Component of Induced Velocity in the Lateral Plane of a Rotor with Harmonic Azimuthwise Vorticity Distribution", NASA TN D-809, 1961.
16. Heyson, H. H., "A Brief Survey of Rotary Wing Induced Velocity Theory", NASA TM 78741, June 1978.
17. Baskin, V. Ye, Vil'dqrube, L. S; Vozhdayey, Ye. S, and Maykapar, G. I., "Theory of Lifting Airscrews", NASA TTF-823, 1975.
18. Ormiston, R. A., "An Actuator Disc Theory for Rotor Wake Induced Velocities", AGARD CP-111, February 1973.
19. Goldstein, S., "On the Vortex Theory of Screw Propellers", Royal Society Proceedings, Vol. 123, 1929.
20. Lock, C. N., "Application of Goldstein's Airscrew Theory to Design", Aeronautical Research Committee (Great Britain), R&M No. 1377, Nov 1930.
21. Jenney, D. S., Olson, J. R., and Landgrebe, A. J., "A Reassessment of Rotor Hovering Performance Prediction Methods", Journal of The American Helicopter Society, Vol. 13, No. 2, April 1968.
22. Landgrebe, A. J. and Cheney, M. C., "Rotor Wakes - Key to Performance Prediction", Presented at the Symposium on Status of Testing and Modeling Techniques for V/STOL Aircraft, Mideast Region of The American Helicopter Society, Oct 26, 1972.
23. Piziali, R. A., and DuWaldt, F. A., "A Method for Computing Rotary Wing Airload Distribution in Forward Flight", TCREC Technical Report 62-44, 1962.
24. Piziali, R. A., "A Method for Predicting the Aerodynamic Loads and Dynamic Response of Rotor Blades", USAAVLABS Technical Report 65-74, 1966.
25. Clark, D. R. and Leiper, A. C., "The Free Wake Analysis - A Method for the Prediction of Helicopter Rotor Hovering Performance", 25th Annual Forum of The American Helicopter Society, May 1969.
26. Sadler, S. G., "Development and Application of a Method for Predicting Rotor Free Wake Positions and Resulting Rotor Blade Airloads", NASA CR-1911 Vol. I - Model and Results, NASA CR-1912 Program Listings 1971.

27. Sadler, S. G., "Main Rotor Free Wake Geometry Effects on Blade Air Loads and Response for Helicopters in Steady Maneuvers", NASA CR-2110 Vol. II - Theoretical Formulation and Analysis of Results, NASA CR-2111.
28. Landgrebe, A. J., "An Analytical Method for Predicting Rotor Wake Geometry", Journal of The American Helicopter Association, Vol. 14, No. 4, Oct 1969.
29. Landgrebe, A. J., "An Analytical and Experimental Investigation of Helicopter Rotor Hover Performance and Wake Geometry Characteristics", USAAMRDL Technical Report 71-24, U.S. Army Air Mobility Research and Development Laboratory, Fort Eustis, VA, June 1971.
30. Landgrebe, A. J. and Bellinger, E. D., "An Investigation of the Quantitative Applicability of Model Helicopter Rotor Wake Patterns Obtained From a Water Tunnel", USAAMRDL Technical Report 71-69, U.S. Army Mobility Research and Development Laboratory, Fort Eustis, VA, December 1971.
31. Landgrebe, A. J., "The Wake Geometry of a Hovering Helicopter Rotor and Its Influence on Rotor Performance", Journal of The American Helicopter Society, Vol. 17, No. 4, October 1972.
32. Johnson, W. and Scully, M., "Aerodynamic Problems in the Calculation of Helicopter Air Loads", Presented at the Symposium on Status of Testing and Model Techniques for V/STOL Aircraft Mideast Region, American Helicopter Society", October 26 - 27, 1972, Philadelphia, PA.
33. Johnson, W., "A Comparison Between Experimental Data and Helicopter Air Loads Calculated Using a Lifting Surface Theory", MIT Aeroelastic and Structures Research Laboratory, TR 157-1, July 1970.
34. Scully, M. P., "A Method of Computing Helicopter Vortex Wake Distortions", MIT Aeroelastic and Structures Research Laboratory, TR 138-1, June 1967.
35. Scully, M. P., "Computation of Helicopter Rotor Wake Geometry and Its Influence on Rotor Harmonic Airloads", MIT Aeroelastic and Structures Research Laboratory, TR 178-1, March 1975.
36. Kocurek, J. D. and Tangler, J. L., "A Prescribed Wake Lifting Surface Hover Performance Analysis", Journal of The American Helicopter Society, Vol. 22, No. 1, January 1977.

37. Kocurek, J. D., "A Lifting Surface Performance Analysis with Circulation Coupled Wake for Advanced Configuration Hovering Rotors", P.H.D. Thesis, Texas A&M University, May 1978.
38. Wood, E. R. and Hermes, M. E., "Rotor Induced Velocities in Forward Flight By Momentum Theory", AIAA Paper No. 69-224, 1969.
39. Carpenter, P. J. and Fridovich, B., "Effect of a Rapid Blade Pitch Increase on the Thrust and Induced Velocity Response of a Full Scale Helicopter Rotor", NACA TN 3044, November 1953.
40. Azuma, A. and Kawchi, K., "Local Momentum Theory and Its Application to the Rotary Wing", AIAA Paper No. 75-865, 1975.
41. Stricker, R. and Gradl, W., "Rotor Prediction with Different Downwash Models", Presented at the Fourth European Rotorcraft and Powered Lift Aircraft Forum, Paper No. 6, September 1978.
42. Mangler, K. W. and Squire, H. B., "The Induced Velocity Field of a Rotor", R&M, No. 2642, 1950.
43. Joglekar, M. and Loewy, R., "An Actuator - Disc Analysis of Helicopter Wake Geometry and the Corresponding Blade Response", USAAVLABS Technical Report 69-66, 1970.
44. Amer, K. B., "Theory of Helicopter Damping in Pitch or Roll and Comparison with Flight Measurements", NACA TN - 2136, October 1948.
45. Rebont, Jean, Valensi, Jacques and Soulez-Lariviere, Jean, "Windtunnel Study of the Response in Lift of a Rotor to an Increase in Collective Pitch in the Case of Vertical Flight Near the Autorotative Regime", NASA TTF-17, 1960.
46. Rebont, Jean, Valensi, Jacques and Soulez-Lariviere, Jean, "Response of Rotor Lift to an Increase in Collective Pitch in the Case of Descending Flight, the Regime of the Rotor Being Near Autorotation", NASA TTF-18, 1960.
47. Rebont, Jean, Valensi, Jacques and Soulez-Lariviere, Jean, "Response of a Helicopter Rotor to an Increase in Collective Pitch for the Case of Vertical Flight", NASA TTF-55, 1961.
48. Loewy, R. G., "A Two Dimensional Approach to the Unsteady Aerodynamics of Rotary Wings", Journal Aerospace Science 24, 82-98, 1957.

49. Miller, R. H., "Rotor Blade Harmonic Air Loading", IAS Preprint No. 62-82, January 1962.
50. Jones, J. P., "An Actuator Disc Theory for the Shed Wake at Low Tip Speed Ratios", MIT Aeroelastic and Structures Laboratory", Technical Report 133-1, 1965.
51. Tararine, S. and Delest, M., "Experimental and Theoretical Study of Local Induced Velocities Over a Rotor Disc for Analytical Evaluation of the Primary Loads Acting on Helicopter Rotor Blades", European Research Office U.S. Department of the Army Contract, No. DA-91-591-EUC-1165, Report No. DE 2012, 15 October 1960.
52. Segel, L., "Air Loading on a Rotor Blade as Caused by Transient Inputs of Collective Pitch", USAAVLABS Technical Report 65-65, 1965.
53. Shupe, N. K., "A Study of the Dynamic Motions of Hingeless Rotored Helicopters", P.H.D. Thesis, Princeton University, 1970.
54. Kuczynski, W. A., and Sissingh, G. J., "Research Program to Determine Rotor Response Characteristics at High Advance Ratios", NASA CR 114290, LR 24122, February 1971.
55. Kuczynski, W. A., and Sissingh, G. J., "Characteristics of Hingeless Rotors with Hub Moment Feedback Controls Including Experimental Rotor Frequency Response", NASA CR 114427 (Vol. I) and NASA CR 114428 (Vol. II) LR 25048, January 1972.
56. Kuczynski, W. A., "Experimental Hingeless Rotor Characteristics at Full Scale First Flap Mode Frequencies", NASA CR 114519, LR 25491, October 1972.
57. London, R.J., Watts, G. A., and Sissingh, G. J., "Experimental Hingeless Rotor Characteristics at Low Advance Ratio with Thrust", NASA CR 114684, December 1973.
58. Azuma, Akira and Nakomura, Yoshiya, "Pitch Damping of Helicopter Rotor with Nonuniform Inflow", Journal of Aircraft, Vol. 11, No. 10, October 1974.
59. Shipman, K., "Effect of Wake on the Performance and Stability Characteristics of Advanced Rotor Systems", USAAMRDL Technical Report 74-45, September 1974.
60. Ormiston, R. A. and Peters, D. A., "Hingeless Helicopter Rotor Response with Nonuniform Inflow and Elastic Blade Bending", Journal of Aircraft, Vol. 9, No. 10, Oct 1972.

61. Gaonkar, G. H. and Peters, D. A., "Flap-Lag Stability with Dynamic Inflow by the Method of Multiblade Coordinates", AIAA Paper No. 79-0729, April 1979.
62. Crews, S. T., Hohenemser, K. H., and Ormiston, R. A., "An Unsteady Wake Model for a Hingeless Rotor", Journal of Aircraft, Vol. 10, No. 12, December 1973.
63. Peters, D. A., "Hingeless Rotor Frequency Response with Unsteady, Inflow", Presented at the AHS/NASA - Ames Specialists Meeting on Rotorcraft Dynamics, NASA SP-362, February 1974.
64. Ormiston, R. A., "Application of Simplified Inflow Models to Rotorcraft Dynamic Analysis", Journal of The American Helicopter Society, Vol. 21, No. 3, July 1976.
65. Peters, D. A. and Gaonkar, G. H., "Theoretical Flap-Lag Damping with Various Dynamic Inflow Models", Presented at The 35th Annual National Forum of The American Helicopter Society, Washington, D.C., May 1979.
66. Banerjee, D., Crews, S. T., Hohenemser, K. H., and Yin, S. K., "State and Parameter Identification Applied to Rotor Model Dynamic Test Results", Journal of the American Helicopter Society, April 1977.
67. Banerjee, D., Crews, S. T., and Hohenemser, K. H., "Parameter Identification Applied to Analytic Hingeless Rotor Modeling", Journal of The American Helicopter Society, January 1979.
68. Landgrebe, A. J., Egolf, T. A., "Rotorcraft Wake Analysis for the Prediction of Induced Velocities", USAAMRDL Technical Report 75-45, U.S. Army Mobility Research and Development Laboratory, Fort Eustis, VA, January 1976.
69. Wei, F. S., and Peters, D. A., "Lag Damping In Autorotation by a Perturbation Method", Presented at the 34th Annual National Forum of The American Helicopter Society, Washington, D.C., May 1978.
70. Mangler, K. W., "Fourier Coefficients for Downwash of a Helicopter Rotor", Royal Aircraft Establishment Report No. Aero. 1958, May 1948.
71. Pitt, D. M., Peters, D. A., "Theoretical Prediction of Dynamic Inflow Deviations", Presented at the Sixth European Rotorcraft and Powered Lift Aircraft Forum, Bristol, England, September 1980.
72. Bramwell, A. R. S., Helicopter Dynamics, John Wiley & Sons, New York, 1976

73. Churchill, R., Brown, James and Verkey, R., Complex Variables and Applications, McGraw-Hill Book Company, Third Edition, 1976, Page 70.
74. Abramowitz, M. and Stegun, Irene, Handbook of Mathematical Functions with Formulas, Graphs, and Mathematical Tables, Dover Publications, Inc., New York, 1965, Page 79.

9. VITA

Biographical items on the author of the thesis, Mr. Dale M. Pitt

- 1) Born September 21, 1950
- 2) Attended the University of Missouri-Rolla from September, 1968 to May, 1972. Graduated Magna Cum Laude and received the degree of Bachelor of Science in Aerospace Engineering in May, 1972.
- 3) Aerospace Engineer, United States Army Aviation Research and Development Command, July, 1972 to present.
- 4) Attended the University of Missouri-Rolla Graduate Center from August, 1972 to August, 1975. Received the degree of Master of Science in Aerospace Engineering in August, 1975.
- 5) Attended Washington University from January, 1977 to the present date. Awarded the American Helicopter Society's Vertical Flight Scholarship in 1978 and 1979.
- 6) Membership in Professional and Honor Societies: American Institute of Aeronautics and Astronautics, American Helicopter Society, American Society of Mechanical Engineers, National Society of Professional Engineers, Missouri Society of Professional Engineers, Tau Beta Pi, Phi Kappa Phi and Intercollegiate Knights.

December, 1980

Short Title: Dynamic-Inflow Models Pitt, D.Sc. 1980

DATE
FILMED
- 8